Università degli Studi di Firenze
Dipartimento di Chimica
Scuola di Dottorato in Scienze

Dottorato di Ricerca in Scienze Chimiche
XXIII Ciclo
CHIM/03 - Chimica Generale ed Inorganica

Thermal deposition of Single Molecule Magnets on metallic and magnetic surfaces

PhD. Thesis by

Ludovica Margheriti

Tutor
Prof. Andrea Caneschi

Coordinator
Prof. Andrea Goti

Ad Alberto

Contents

Abstract

The aim of this thesis work is the preparation and investigation of the magnetic properties of two main classes of SMMs (Fe_4 and $TbPc_2$) deposited on metallic and magnetic surfaces by using thermal evaporation thechniques. The evaporated molecules have been characterized from the chemical and the magnetic points of view in order to verify if the thermal evaporation process in HV or UHV conditions induces a decomposition of the molecules and if the metallic or magnetic surfaces could influence the magnetic behavior of the deposited molecules.

In **Chapter 1** we have described the main concept that characterize the single molecule magnets focusing the attention on the two main classes of the compounds used in this thesis work: namely tetranuclear iron(IIII clusters, Fe_4, and terbium(III) bisphthalocyninato, $TbPc_2$. In particular for these two compounds we have described the magnetic characterization techinques that we have used along this thesis work.

Due to the possibility that SMMs could be used as components for developing innovative devices, the organization on surfaces is the first step in order to address the magnetic state of a single molecule or to connect the molecules to a conducting substrate. For this reason we have considered appropriate to briefly resume in **Chapter 2** the most common deposition techniques suitable to deposit Fe_4 and $TbPc_2$ molecules on surface.

C**hapter 3** describes our first experimental results on the thermal deposition of a thick film of a Fe_4 family containing different tripodal ligands. In fact the introduction in the precursor compound of this type of organic ligands enhances the magnetic properties by increasing the anisotropy barrier and makes the complexes much more stable thanks to the chelating effect of the triol groups. For each compounds we have described the thermal deposition parameters and the chemical, as well as the subsequent magnetic characterization, of the deposited thick films carried out by combining the use of time-of-flight secondary ion mass

spectrometry, ToF-SIMS, superconducting quantum interference device (SQUID) magnetometry, high frequency electron paramagnetic resonance (HF-EPR) and alternating current (ac) susceptibility measurements. We have demonstrated that for some molecules it is possible to evaporate films of different thickness keeping intact the Single Molecule Magnets behaviour.

In the second part of this thesis work we have described the characterisation of monolayer evaporated on metallic and magnetic surfaces, allowed thanks to the very high sensitivity and element selectivity of X-ray Absprption Spectroscopy and the possibility to measure the X-ray Magnetic Circular Dichroism, XMCD. In **Chapter 4** we have therefore breafly given the basis of XMCD and we have described some examples useful to introduce and better understand the experiments carried out on the evaporated monolayers samples of Fe_4 and $TbPc_2$.

Finally, in **Chapter 5** and **Chapter 6** we have described the most important experimental results of this thesis work that allowed us to increase the information relative to the magnetic beahaviour of SMM molecules on surface. In fact thanks to the sensitivity of XMCD and the experimental low temperature reached by using the ^{3}He-^{4}He dilution cryostat, we have been able to demonstrate that the evaporated Fe_4 monolayer on gold surface maintains intact the typical SMM behavior of the dynamics of the magnetization while, surprisingly, the same compound evaporated on a magnetic substrate, manganite, LSMO, shows a suppression of the tunneling around zero field, clearly indicating an influence of the substrates.

In **Chapter 6** we move to the another class of SMM characterized by the strong anisotropy of the rare-earth ions, $TbPc_2$. We have reported the XMCD analysis conducted on an evaporated thick film, and on a monolayer deposit on gold and manganite substrates. Once again we have demonstrated that the orientation of the molecules and the dynamics of the magnetization can be influenced by the surface. These findings contribute to understand the magnetic behavior of the SMM systems on magnetic and metallic surfaces and open interesting perspectives in the development of vertical devices formed by multilayer hetero-structures, that can reveal novel phenomena of great interest in the field of molecular spintronics.

Chapter 1.

Single Molecule Magnets

1.1. Introduction

Magnetism is certainly one of the fundamental properties of matter, inextricably associated with electrical properties, and molecular magnetic materials have recently become a hot topic, thanks to the efforts of many research groups. The nineties were characterized by an intense research on a new class of molecular materials, known as Single Molecule Magnets (SMMs).[1-3] These are in general polynuclear coordination compounds of paramagnetic metal ions held together by suitable ligands, which often provide an effective shielding between adjacent molecules in the solid. The magnetic centers can be transition-metal or rare-earth ions, or even organic radicals. The most interesting aspect is that a few of these molecular clusters, featuring a combination of a large spin and an easy axis magnetic anisotropy, are characterized by a dramatic slowing down of the fluctuations of the magnetization at low temperature, and in some cases a magnetic hysteresis is observed.[4] At variance with more conventional magnetic materials, this type of hysteresis has a pure molecular origin and does not imply long range order. It was soon recognized that Single Molecule Magnets hold great potential to store information at the molecular level, even if the temperatures at which the hysteresis is observed remains prohibitive for technological applications. In fact, it is still confined to liquid helium region despite the many synthetic efforts. This, however, has not diminished the interest in SMMs as model systems to investigate magnetism at the nanoscale and, in particular, the coexistence of quantum phenomena with the classical hysteretic behaviour.[5] A key issue that has emerged in the last years is the possibility to address the magnetism of a single molecule, indeed a mandatory step to fully exploit the potential of SMMs. In its circular pathway, molecular magnetism is therefore focussing again on isolated magnetic objects. However, the environment is no

longer a crystal lattice but a nanostructured surface or a miniaturized electronic device built using a single magnetic molecule. This gives the possibility to combine the rich quantum dynamics of SMMs with transport properties, in the emerging field known as *molecular spintronics*.[6] The first step in this direction has been the organization of isolated SMMs on conducting and semiconducting surfaces[7] as a means of imaging single molecules and of measuring their transport properties with scanning probes techniques. Synchrotron based techniques, in particular X-ray Absorption Spectroscopy with circularly polarized light,[8] have been used in molecular magnetism because of their unique capability to provide element specific magnetic information,[9] as well as to distinguish between orbital and spin contributions to the magnetism of the molecular material. More recently the great sensitivity of these techniques started to play a key role for the investigation of molecular adsorbates at surfaces.[10-12] Here, the challenge consists in clarifying the influence of the surface on the magnetic properties, and especially on the memory effect of a SMM, which is known to be dramatically environment dependent.

In this first chapter is reported a brief introduction about a few key concepts in molecular nanomagnetism, *i.e.* magnetic exchange, magnetic anisotropy and magnetization dynamics, and some examples of SMMs containing transition metal and lanthanide ions.

1.2. Single Molecule Magnet properties

1.2.1. Magnetic exchange interactions in polynuclear Single Molecule Magnets

SMM are magnetic molecules characterized by high spin ground state (*S*), high zero field splitting and an easy axis of the magnetization (which correspond to high and negative zero field splitting parameter D). If we exclude the case of mononuclear lanthanide complexes [13] of high symmetry, *e. g.* double decker compounds with phthalocyanine, that we have described in the last part of this chapter, all other molecules presenting slow relaxation of the magnetization are constituted by polynuclear complexes of paramagnetic metal ions. Usually in this case only interactions between nearest neighboring magnetic sites are considered and the effective Spin Hamiltonian (SH) can be write:

$$H_{ex} = \sum_{i>j}^{J_{ij}} S_i \cdot S_j \qquad (1.1)$$

where *i* and *j* run over all metal sites of the cluster. The energy of the different S_T states can be calculated analytically in some high symmetry cases, in particular when a central spin exhibits the same exchange interaction with the neighboring ones. This is also known as the Kambe approach[14] and spin systems comprising up to 13 coupled spins have been handled in this way.[15] A spin system that can be treated with this approach is the tetrameric unit schematized in **Figure 1.1** and can be applied to a large family of tetranuclear iron(III) clusters, Fe_4,[16-17] also known as *iron stars*:[18]

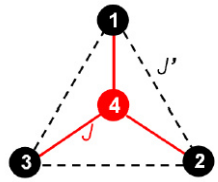

Figure 1.1: Coupling scheme in a star-like tetramer.

1.2.2. Magnetic anisotropy in Single Molecule Magnets

The spin structure of the SMM is strongly correlated to the dynamics of the magnetization and can be considered as a sort of fingerprint of the SMM. On the other hand the occurrence of a large spin ground state is a necessary, although not sufficient, condition to observe slow relaxation of the magnetization. The second key ingredient in SMM is magnetic anisotropy. In traditional magnets, three factors give equally important contributions to the anisotropy, namely surface, strain, and magnetocrystalline contributions. In SMM the only significant role is played by magnetocrystalline anisotropy and is brought in by a combination of spin-orbit coupling with the low-symmetry environment around the metal centers constituting the SMM. Dipolar contributions are in most cases negligible. A quantitative treatment of the magnetic anisotropy is based on the effective spin-hamiltonian approach where only the spin variables appear, while the orbital contributions are introduced through parameters. For a system with no symmetry at all, the SH can be written as:

$$H_{an} = \boldsymbol{S} \cdot \widehat{\boldsymbol{D}} \cdot \boldsymbol{S} = D\left[S_z^2 - \tfrac{1}{3}S(S+1)\right] + E(S_x^2 - S_y^2) \qquad (1.2)$$

where $D = D_{zz} - \frac{1}{2}D_{xx} - \frac{1}{2}D_{yy}$ represents the axial anisotropy, and $E = 1/2\,(D_{xx} - D_{yy})$the transverse (or rhombic) one. The value of E is intrinsically limited to $1/3\,D$ because going beyond this limit indeed corresponds to a change in the axis of the leading anisotropy. The effect of the magnetic anisotropy on the (2*S*+1) states of the spin multiplet is that of removing their degeneracy even in the absence of an external field, and thus is also named *Zero Field Splitting* (ZFS).

The effect of a negative *D* in Eq. 1.2 is that the system can be magnetized much more easily when the field is applied along the principal, *i.e. z*, axis. Moreover a system showing easy axis magnetic anisotropy, D<0, has the ground doublet characterized by $m = \pm S$, which corresponds to two potential wells separated by an energy barrier, U_{eff}, as reported in **Figure 1.2**. In the case of a spin system constituted by a single paramagnetic center carrying 2*S* unpaired electrons, the value of *D* can be experimentally determined through electron paramagnetic spectroscopy (EPR),[19-21] or alternatively through inelastic neutron scattering.[22] Also magnetometry, especially if performed on a single crystal sample, can provide accurate values. The magnetic anisotropy can also be estimated theoretically, with a great variety of approaches. These range from simple perturbation theory, starting from a spectroscopic estimation of the energy separation of the partially filled *d* orbitals,[23-24] to a ligand field treatment based on the Angular Overlap Model.[25] More recently *ab initio* calculations, either based on Density Functionals or on post Hartree-Foch approaches [26] have also shown a good predictive capability.

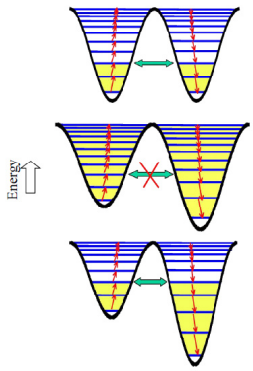

Figure 1.2: Anisotropy barrier and wells in case of a Mn_{12} SMM (S = 10) The upper part of the figure represents the two wells in case of zero field. In the middle when a magnetic field is applied, but the quantum tunneling is not permitted. The bottom part represents the two wells in case of applied magnetic field and permitted quantum tunneling.

The situation is more complicated in the case of a polynuclear metal system, such as most SMMs. In general, when working with first row transition metal ions it is found that the magnetic anisotropy is weaker than intramolecular exchange interactions. Hence, the resulting states are well described by the quantum number corresponding to the total spin state, as derived from Eq.1.1, and the magnetic anisotropy is introduced as a perturbation. The magnetic anisotropy of a given total spin S_T can be related to the single ion contributions, or to the anisotropic part of the interaction, either dipolar or exchange in nature, by using projection techniques:[27]

$$\boldsymbol{D_{S_T}} = \sum_i d_i \boldsymbol{D_i} + \sum_{i>j} d_{ij} \boldsymbol{D_{ij}} \qquad (1.3)$$

where i and j refer to the magnetic centers inside the SMM. The projection coefficients d_i and d_{ij} depend on how the individual spins project on the total spin state under consideration, D_i are the single ion contributions, and D_{ij} the anisotropy brought in by two-spins interactions. The calculation of d_i and d_{ij} is based on a relatively simple recursive algorithm, and very small value are typically found. This indicate that it is not straightforward to combine a large spin with a large magnetic anisotropy. Although apparently to couple more and more spins to increase S should lead to a quadratic effect on the height of the barrier, the projection of the anisotropies of the single ion makes the barrier to scale linearly with S.[28]

1.2.3. The dynamics of the magnetization

Slow relaxation of the magnetization was first observed in Mn_{12}ac thanks to alternating current (ac) susceptibility experiments. By operating at sufficiently low temperature the relaxation becomes so slow that an opening of the hysteresis is observable.[29] This dramatic slowing down of the fluctuations has its origin in the double well potential reported in **Figure 1.2**, characteristic of a large spin with a negative D parameter. The application of a magnetic field has the effect of stabilizing and populating preferentially one of the two wells. Once the field is removed, an equal population of the two wells, corresponding to zero magnetization, is only re-established by transferring part of the population on the other well. Transitions from one state to the other are promoted by deformations of the metal coordination environment. (rotations and geometrical strains) which can affect the spin degrees of freedom thanks to spin orbit coupling. However, at a first level of approximation these deformations are only able to induce transitions between states differing in m by ±1 and ±2. To overcome the energy barrier a multiphonon mechanism is therefore necessary. In analogy to a chemical

reaction involving many elementary processes, the overall rate is determined by the slowest step. In the case of a SMM, the slowest step is the one on top of the barrier, because at low temperature the highest states are less populated and also because of the quadratic energy spacing induced by Eq.1.2. The combination of these two factors yields an exponential temperature dependence of the relaxation time, which is typical of a thermally-activated mechanism:

$$\tau = \tau_0 \exp\left(U_{eff}/k_B T\right) \qquad (1.4)$$

where U_{eff} is the *effective* anisotropy barrier and τ_0 the pre-exponential factor.In Mn_{12}ac, and other SMMs like Fe_4 it is possible to observe also quantum effects, such as the tunneling of the magnetization. In fact, beside the thermally activated process, spin reversal in SMMs may also occur by quantum tunneling: whenever two states lying on opposite sides of the barrier have the same energy and the wavefunction of the left well extends to the right wall with a nonzero value, the probability of observing a through-barrier transition is different from zero.[30-31]

This phenomenon has been first observed in the ac magnetic susceptibility of Mn_{12}ac SMM [32] and then, more spectacularly, in the hysteresis curve, which is characterized by steps at the resonant fields (see **Figure 1.3**). In fact the vertical segments of the curve in **Figure 1.3** reflect accelerations of the relaxation rate and thus can be attributed to the quantum tunnelling process.[33-34]

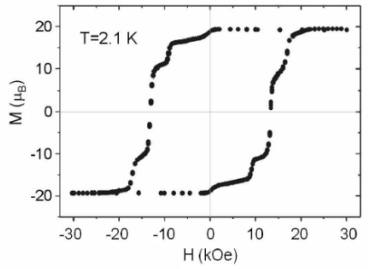

Figure 1.3: Hysteresis loop of a Mn_{12}ac single crystal with the applied field parallel to the tetragonal axis.

The fascinating interplay between quantum and classical effects in the dynamics of the magnetization of molecular nanomagnets has attracted great interest among physicists and chemists and many other spectacular phenomena have been observed in the last ten years, including topological interferences[35] and quantum coherence[36] to mention only two.

In the next two sections we shall describe the structures and the principal magnetic properties of the two main SMMs studied in this thesis work based on 3*d* transition metal and 4*f* lanthanide ions: Fe_4 and $TbPc_2$ SMMs.

1.3. Fe_4 SMM family

Fe_4 clusters are among the simplest inorganic systems showing SMM behaviour.[16, 37-38] The archetypal member of this class is the tetrairon(III) compound, Fe_4std, $[Fe_4(OMe)_6(dpm)_6]$ (Hdpm =dipivaloylmethane) (**Figure 1.4**). The six methoxide ligands bridge a central Fe(III) ion to three peripheral iron centers arranged at the vertices of an isosceles triangle with[16] a crystallographic C_2 symmetry, and some disorder which yields three different isomers in the lattice. At low temperature, the cluster has a high-spin state (S=5) and easy-axis magnetic anisotropy.

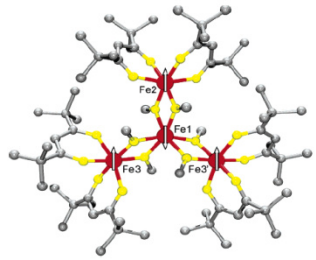

Figure 1.4: Molecular structure of Fe_4std. Color code: Fe = red, O = yellow, C = grey. The arrows give the spin configuration in the ground *S* = 5 state of the molecule.

This complex can be converted into a new class of SMMs by exchanging the bridging methoxides with tripodal ligands $R–C(CH_2OH)_3$.[17] This site-specific ligand replacement provides in some cases a means to raise the symmetry of Fe_4 clusters from C_2 to D_3. Moreover upon ligand replacement, the magnetic properties are in general enhanced and the anisotropy barrier is larger than that in the standard compound, reaching up to 17 K. In particular the complexes containing the tripodal ligand evidence a striking magnetostructural correlation between the height of the anisotropy barrier, its shape, and the helical pitch of the Fe-$(O_2Fe)_3$ core. Such energy barrier is still very low compared to those typical of Mn_{12} clusters, and to directly observe the blocking of the magnetization it is necessary to reach sub-Kelvin temperatures. The chelating effect of the triolate ligands also make the complex much more stable than its precursor, thus allowing a much easier manipulation. In the next section we will describe the most

representative Fe_4 derivative studied in this thesis work and the description of its magnetic properties will serve as the basis for the briefer introduction to the other Fe_4 complexes presented.

1.3.1. Fe_4Ph SMM compound

$Fe_4(Ph–C(CH_2O)_3)_2(dpm)_6$ compound, Fe_4Ph, was prepared by introducing the appropriate triol ligand around Fe_4 core.[17, 31] It crystallized in the monoclinic space group. The unit cell comprises four clusters and four diethyl ether molecules, which are easily lost from the crystalline lattice. The crystallographic symmetry is C_2, as the cluster develops around a two-fold axis parallel to the b-axis of the unit cell. Moreover this compound exhibit a good degree of order in the crystal structure, disorder effects being limited to the ^{t}Bu groups of the dpm ligands (**Figure 1.5**).

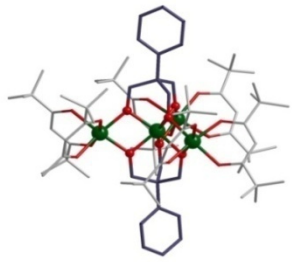

Figure 1.5: Molecular structure of $[Fe_4(Ph–C(CH_2O)_3)_2(dpm)_6]$. Color code: iron(III), green balls; oxygen, red balls and sticks; carbon, blue thin and thick sticks (indicating the dpm ligand and the aromatic tripodal ligand, respectively).

Magnetic properties. The molar magnetic susceptibility and the magnetization of Fe_4Ph are shown in **Figure 1.6** as a $\chi_m T/T$ and a M/H plots. In the $\chi_m T/T$ plot is recognizable the characteristic of "ferric stars" behaviour, where the dominant antiferromagnetic interaction between the central and peripheral high-spin iron(III) centers generate an S = 5 ground state. The $\chi_m T$ value first decreases upon cooling down from room temperature, going through a minimum at around 100 K, to reach then a maximum at 10–15 K. Further cooling results again in a decrease of the magnetic moment. The value at the maximum (16 emu K mol^{-1}) is close to the Curie constant for an S = 5 state (15.0 emu K mol^{-1} for g = 2.00).[39]

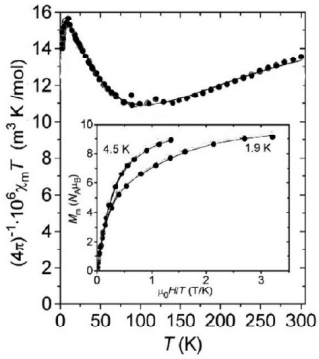

Figure 1.6: Temperature dependence of χT of Fe_4Ph in an applied field of 1 kOe. In the inset the magnetization curves at two different temperature.

Quantitative fitting of the data using a Heisenberg spin-Hamiltonian with nearest-neighbor (J) and next-nearest-neighbor (J') coupling constants gave the following parameters J = 16.37(12) cm^{-1} and J' = 0.29(11) cm^{-1}.(for the definition of nearest-neighbor J and next-nearest-neighbor J', see **Figue1.1**). The pattern of nearest-neighbour exchange-coupling constants observed in standard Fe_4 and in Fe_4Ph (Fe_4std > Fe_4Ph) is correlated with the Fe-O-Fe angles (average value: 104,3° and 103.2°). In fact studies performed on simple dimers ($Fe_2(dpm)_4(OMe)_2$) have shown that the strength of magnetic coupling within Fe-(OMe)-Fe units increases with the angle at the bridging oxygen atoms. Inspection of the data using the Heisemberg Hamiltonian, that can be written using the Kambe approach:

$$H_{ex} = J[S_1 \cdot S_4 + S_2 \cdot S_4 + S_3 \cdot S_4] + J'[S_1 \cdot S_2 + S_2 \cdot S_3 + S_1 \cdot S_3] \qquad (1.5)$$

proves the expected trend; i.e., a wider Fe-O-Fe angle results in a larger J constant.[31] Confirmation of the ground state spin could be found measuring the isothermal molar magnetization at 4.5 and 1.9 K as a function of applied field (**Figure 1.6 inset**). In fact it was possible to see how the magnetization approached the expect value $M_m = 10N_a\mu_B$ in the high field. The non-coincidence of the two isothermal curves at different temperatures is a signature of magnetic anisotropy effects in the ground state. Fitting the magnetization data using an axial Zero-Field Splitting plus Zeeman Hamiltonian (Eq. 1.6) resulted in D = – 0.421 cm^{-1} and – 0.415 cm^{-1} for the two isomers. An accurate fit being impossible with a positive D value confirming the Ising-type magnetic anisotropy:

$$H = D\left[S_z^2 - \frac{1}{3}S(S+1)\right] + g\boldsymbol{\mu_B}\boldsymbol{S}\cdot\boldsymbol{H} \qquad (1.6)$$

HF-EPR proved to be one of the most powerful methods in determining spin Hamiltonian parameters of molecular nanomagnets. One of the main advantages is the simplification of the spectra induced by the high fields, since Zero Field Splitting terms can be treated, in the first approximation, as a perturbation of the Zeeman effect. As a consequence, successive parallel and perpendicular transitions of a purely axial system are separated by $2|D|/g_{||}\mu_B$ and $|D|/g_{\perp}\mu_B$, respectively. Thus the $|D|$ value can be obtained by simple inspection of the spectrum. Furthermore, the large Zeeman splittings induced at large applied magnetic fields also allow the determination of the sign of D by monitoring depopulation effects within a spin manifold. Indeed, a complex with a negative D value will give an EPR spectrum with the intensity of parallel transitions increasing toward low fields upon cooling, while the trend will be reversed for a complex with a positive D value. Temperature-dependent HF-EPR spectra of Fe_4Ph recorded at 230 GHz is shown in **Figure 1.7**.[31]

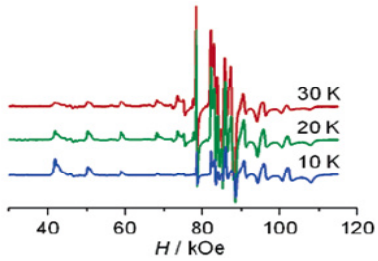

Figure 1.7: Temperature dependence for the 230-GHz HF-EPR spectra of $Fe_4Ph{\cdot}Et_2O$ compound.

On lowering temperature the intensity moves toward the extremes of the spectrum and the largest extension is observed in low fields, a characteristic behaviour for SMMs. Inspection of the spectra of Fe_4Ph in the parallel region evidences a clear splitting of the lines (**Figure 1.8**), suggesting the existence, in comparable amounts, of two not equivalent clusters with slightly different axial anisotropies D = – 0.420 cm^{-1} and – 0.414 cm^{-1} from the line-to-line separation. These values are in good agreement with the observation of a transition close to zero field at 115 GHz (**Figure 1.8**), which indicates that the energy difference between the M_S = ±4 and ± 5 doublets is ca. 3.8 cm^{-1}. Furthermore, the extension and partial splitting of the spectral lines in the perpendicular region are clear signatures of rhombic distortion, consistent with the crystallographic C_2 symmetry. The fact that the two axial ZFS parameters are so similar suggests that

the presence of non equivalent cluster might reflect the disordered ^{t}Bu groups or an unresolved disorder of the Et_2O molecules.

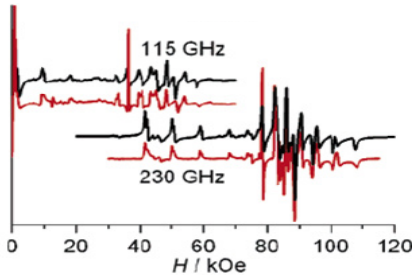

Figure 1.8: Experimental (red) and simulated (black) EPR powder spectra of $Fe_4Ph{\cdot}Et_2O$ at different frequencies and at 10K.

These results has been confirmed by measuring the frequency and temperature dependence of the ac magnetic susceptibility in zero static field (**Figure 1.9**).[31]

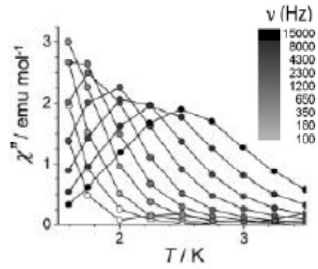

Figure 1**.9:** Temperature dependence of the imaginary components of the ac susceptibility measured for Fe_4Ph in the frequency range from 100 Hz to 15000 Hz (see color scale).

In fact, while simple paramagnets do not show any imaginary component, χ'', of the complex susceptibility, SMMs are characterized by a freezing of the magnetization and the appearance of a nonzero χ''. Within the Debye model commonly employed to analyse the ac susceptibility of SMMs, a maximum in χ'' is observed when the relaxation time equals $(2\pi\nu)^{-1}$, where ν is the frequency of the oscillating field. In a thermally activated relaxation process that follows the Arrhenius law (Eq.1.4), the relaxation time increases on decreasing temperature, eventually matching at T_{max} the condition that maximizes χ'', thus allowing us to evaluate $\tau(T_{max})=(2\pi\nu)^{-1}$. The typical frequency-dependent maxima in $\chi''(T)$ that characterized the SMM behaviour is observed also for Fe_4Ph compound showing

a barrier U_{eff}/k_B of 15.6 K, 15.0K (for the two isomers) larger than the standard compound (3.5 and 7.4 K for the two isomers) and $\tau_0 = 1.9x10^{-8}$ s.

Another common way to report dispersion data is the Cole-Cole plot used for dielectrics (Cole and Cole 1941),[40] known in magnetism as the Argand plot (Dekker et al. 1989),[3, 40-41] where χ'' vs. χ' is reported. When the relaxation process is not characterized by a single τ but rather by a distribution of relaxation times is necessary to introduce in the Debye model a parameter α, which takes into account deviations from the ideal semicircle centred on the χ' axis. The wider is the distribution in relaxation times the larger is α so that if different components of the magnetisation relax with different processes, more semicircles, sometimes partially merged, can be obtained.[42] In Fe_4Ph sample the Argand plot confirms the presence of two different isomers with slightly different relaxation times (**Figure 1.10**). The best fit of experimental data at different temperatures provided the values α=0.21 at T = 2.0 K, α=0.22 at T = 1.75 K, and α=0.25 at T = 1.5 K.

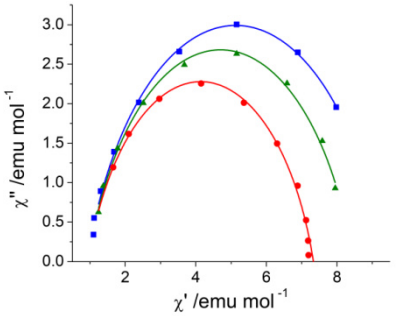

Figure 1.10: Argand plot of Fe_4Ph powder at three temperatures: T = 2 K (red circles), T = 1.75 K (green triangles) and T = 1.5 K (blue squares). The lines represent the best fit curves using a modified Debye model obtained with the values of α = 0.210 at 2.0 K, α = 0.211 at 1.75 K and α = 0.214 at 1.5 K.

1.4. SMM based on lanthanide ion, $TbPc_2$

In the last section of this first chapter we will focus our attention on another class of SMMs based on mononuclear lanthanide complexes describing the principal magnetic measures performed on the archetypal compound. One of the best advantages of using these "*mononuclear lanthanide magnets*" is that the slow magnetization relaxation is observed at significantly higher temperatures than that observed for the transition metal cluster SMMs.[43] On the other hand it is more complex to understand the dynamic magnetic properties of lanthanide complexes

compared to the transition metal ones because the determination of multiplet sub level structures is generally difficult. In fact lanthanide (III)-Pc showing SMMs behaviour have a significant large axial anisotropy which occurs with a different mechanism than those for known 3*d* metal SMMs. In the case of 3*d* cluster SMMs, spin orbit coupling is a perturbation of the ligand field, while the reverse is true for lanthanide ions, being the crystal field responsible of the splitting of the electronic multiplets..[44-45] For example the crystal field of a Tb^{3+} compound ($4f^8$) with a total angular moment *J* of 6 splits the ground multiplet so that the lowest sublevel has the largest J_z value ($|J_z| = 6$, corresponding to up/down spin states) and large energy gaps to the remaining sublevels (ca. 400 cm^{-1}).[43] Because of this unusual condition, there is a small probability for a transition between $J_z = 6$ (up-spin state) and –6 (down-spin state) sub-states and hence a slow magnetization response to an applied magnetic field.

In this paragraph we will focus our attention on the magnetic properties of $Tb(C_{32}H_{16}N_8)_2$, $TbPc_2$, SMM whose magnetic properties on surface will be describe in the **Chapter 5**. $TbPc_2$ complex has a metal ion sandwiched between two phthalocyanine, Pc, molecules with eight isoindole-nitrogen donor atoms. The twisted angle between the two rings was determined to be 41.4°, causing a pseudo 4-fold axis perpendicular to the Pc rings and a distorted antiprismatic coordination environment around the metal center. Both Pc rings are saucer-shaped and slightly distorted. However, one ring deviated more from the planarity than the other (**Figure 1.11**).[44, 46]

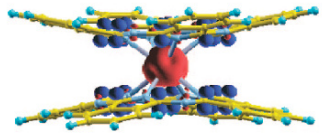

Figure 1.11: Calculated spin densities for the neutral $TbPc_2$ molecule.[46]

The neutral complex have a one-electron ligand oxidized “sandwich” structure, in which the unpaired electron was delocalized on both phthalocyanine ligands. In a recent work, Veciana and co-workers report the spectroscopic changes in the absorption spectra associated with the one-electron electrochemical inter conversions of $[TbPc_2]^{+/0/-}$. [47] These different species are stable and can be well distinguish by the UV/vis spectra (**Figure 1.12**) that show the characteristic absorption bands of double-decker phthalocyanine complexes, including Soret bands at 387, 371, and 358 nm and Q bands at 705, 663, 624 nm, respectively. In the case of $[TbPc_2]^{+/0}$, the characteristic π-radical band is observed at 495 and 475 nm, respectively.

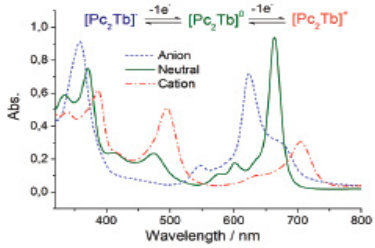

Figure 1.12: UV/vis absorption spectrum of solution of $[TbPc_2]^0$, in CH_2Cl_2 and of solutions of $[TbPc_2]^{+/-}$ generated electrochemically from neutral compound. [47]

Magnetic properties. In the 2003 Ishikawa reported for the first time the typical frequency dependence in the ac susceptibility signals of SMMs in the anionic bis(phtalocyaninato) terbium and dysprosium compounds, $[TbPc_2]^-$ and $[DyPc_2]^-$.[43, 48] These were the first lanthanide complexes functioning as a magnet at the single molecular level and the first mononuclear metal complexes showing such properties.

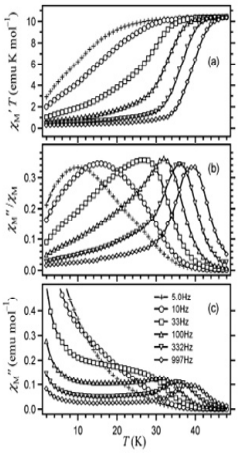

Figure 1.13: (a) $\chi_M'T$, (b) χ_M''/χ_M, and (c) χ_M'' against temperature T, where χ_M', χ_M'', and χ_M are in-phase ac, out-of-phase ac, and dc molar magnetic susceptibilities, respectively, for a powder sample of $[TbPc_2]^-$ measured in zero dc magnetic field with a 3.5 G ac field oscillating at the indicated frequencies.[49]

As observed in **Figure 1.13** relative to the ac and dc measurements, the magnetic relaxation behaviour is similar to that observed in the transition metal SMMs. In fact the $\chi_M'T$ vs T plot exhibits a sudden decrease with decreasing T in the temperature range depending on the ac frequency, indicating that the response of the magnetic moment to the alternating magnetic field is becoming slower. The out-of phase ac component of the magnetic susceptibility exhibits the

characteristic peaks in a χ_M''/χ_M vs T plot (the middle panel) at 40 K, and at each χ_M''/χ_M peak temperature, the magnetization relaxation time τ of the sample matches the inverse of the angular frequency ω of the applied ac magnetic field. To ensure that the slow magnetization relaxation is an intrinsic molecular properties, Ishikawa performed the same measurement diluting the samples into a diamagnetic matrix, like $[YPc_2]^-$. In this case comparing the χ_M''/χ_M plots with those reported for the undiluted sample Ishikawa observed the shift to higher temperature of some peaks (at 10, 100, and 997 Hz) (**Figure 1.14**). This indicates that the intermolecular interactions between adjacent $[TbPc_2]^-$ complexes shorten the relaxation time in the lower temperature range and that the slow magnetization relaxation is an intrinsic single-molecular property of $[TbPc_2]^-$, rather than resulting from intermolecular interactions and long-range order. Moreover in contrast with the undiluted sample (**Figure 1.13c**), all the χ_M'' T plots in **Figure 1.14c** show a clear peak even with an ac field frequency of 0.1 Hz. This is also ascribed to the magnetic interactions between adjacent Tb complexes.

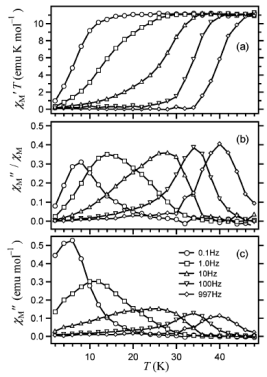

Figure 1.14: (a) $\chi_M'T$, (b) χ_M''/χ_M, and (c) χ_M'' against temperature T for a powder sample of **1** diluted in $[YPc_2]^-$ with the ratio [Tb]/[Y]) 1/50, measured in zero dc magnetic field with a 3.5 G ac field oscillating at the indicated frequencies.[49]

In the second section of this chapter we have described the magnetization relaxation phenomena of the transition metal-SMM observed in the ac susceptibility measurements and we have shown the thermally activated process described by the equation, $\tau = \tau_0 \exp(U_{eff}/k_B T)$, where U_{eff} is the height of the potential energy barrier between the two states with $S_z = \pm S$ and the resonant tunneling process when the energies of the sublevels with different $|Sz|$ values coincide by Zeeman interaction under an appropriate external magnetic field.

In **Figure 1.15** is reported the plot of $\ln(\tau^{-1})$ vs $1/T$ for undiluted and diluted samples of $[TbPc_2]^-$, where T is the χ_M''/χ_M peak temperature at which τ^{-1} matches the angular frequency ω of the applied ac field. As seen in the figure, the plot is divided into two parts. The data points in the higher temperature (higher frequency) part fit a single straight line with no dependence on magnetic dilution The linear relation of $\ln(\tau^{-1})$ to $1/T$ indicates that the Orbach process is dominant in the higher temperature range .On the contrary the data points in the lower-temperature parts are shifted to longer relaxation time by the dilution, meaning that a relaxation process enhanced by the spin-spin interaction between adjacent Tb complexes becomes dominant in the undiluted sample in this temperature range.[49]

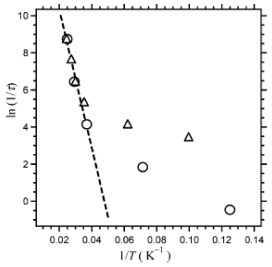

Figure 1.15: Natural logarithm of the magnetization relaxation rate against the inverse of the temperature of the peak of the $\chi_M''/\chi M$ value for the undiluted powder sample of $[TbPc_2]^-$ (triangles) and that diluted at 1:50 in $[YPc_2]^-$ (circles).[49]

This indicates that either the direct or Raman process is dominant in the temperature range below about 25 K. This conclusion is strongly supported by the study of the sublevel structures of the ground multiplets of lanthanide complexes (**Figure 1.16**).

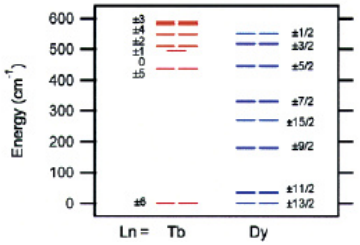

Figure 1.16: Energy diagram of the substates of the ground multiplets of $[LnPc_2]^-$ (Ln = Tb, Dy). The J_z value of each substate is indicated to the right of the corresponding energy level.[13]

In fact as we have described above, in the anionic Tb complex, if the relaxation occurs through a path consisting of stepwise transition from J_z to $J_z \pm 1$, states the "*rate-determining step*" is the first transition from the $J_z = 6$ to $J_z = 5$ (or from –6 to –5) because of the large energy gap (ca. 400 cm^{-1}). As an example we can observe that in the anionic Dy complex, the sublevels are distributed more evenly than the Tb one and this implies a more efficient relaxation pathway. The fit of data relative to the relaxation time of $TbPc_2$ anionic complex, give the barrier heights for the reversal magnetic moment of 260 cm^{-1} and with pre-exponential factor ($1/\tau_0$) of 5.0×10^7 s^{-1}. The barrier high is of the same order of magnitude as the separation between the first and the second lowest sublevels. This suggest the strong correlation between the relaxation rate and the sublevels distribution. It is known that one-electron oxidation of $[TbPc_2]^-$ occurs at the ligand, resulting in the neutral $[TbPc_2]^0$ with an open shell unpaired π electron system delocalized on the two Pc ligands (**Figure 1.17**).

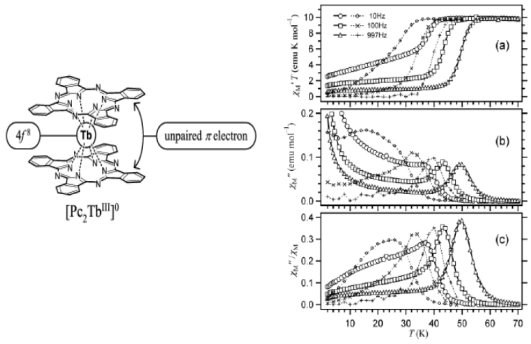

Figure 1.17 Plots of (a) $\chi_M'T$, (b) χ_M'', and (c) χ_M''/χ_M against temperature T, where χ_M', χ_M'', and χM are in-phase-ac, out-of-phase-ac, and dc molar magnetic susceptibilities, respectively, for a powder sample of $[TbPc_2]^0$ fixed in eicosane (open markers with solid lines). The corresponding data for the anionic complex $[TbPc_2]^-$ are shown with dotted lines.[48]

An alternating current magnetic susceptibility measurement of the neutral complex revealed a significant upward of the temperature range where the magnetization starts to freeze. In particular the peaks of the out of phase component of the ac susceptibility observed at 36, 43, and 50 K are shifted to significantly higher temperatures with respect to those of the anionic $[TbPc_2]^-$ complex. The phenomenological barrier height for reversal of the magnetic moment is estimated at 410 cm^{-1} with a pre exponential factor $1/\tau_0 = 6.8\times10^8$ s^{-1}. This is a significant increase from the 260 cm^{-1} ($1/\tau_0 = 5.0\times10^7$ s^{-1}) observed for the anionic compound $[TbPc_2]^-$. However due to the presence of a different

relaxation process that becomes dominant in the lower temperature region, the $\chi_M'T$ and χ_M'' values do not vanish in the low temperature region below 30 K: this means that the magnetic moment is not completely frozen. To clarify whether the upward temperature shift is attributed to an intrinsic molecular property or to long-range magnetic order by intermolecular interactions, Ishikawa and co-worker have carried out the ac susceptibility measurements of the π radical Tb complex under two different dilute conditions:

1) in a diamagnetic media using the same $TbPc_2$ structures functionalized with long-chain alkoxy substituents on the Pc ligand;

2) in $[YPc_2]^0$ having S = 1 /2 spin on the ligand but no *f* electron in the metal ion.

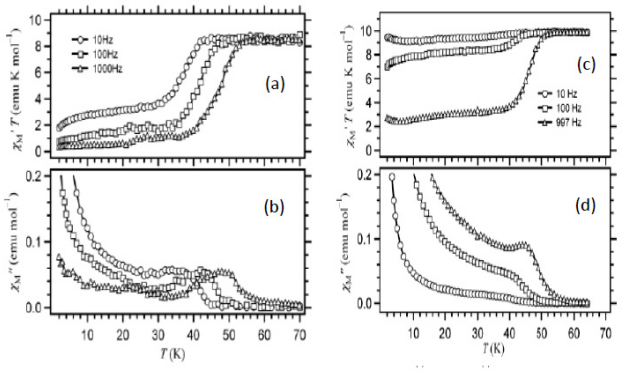

Figure 1.18: plots of (a) $\chi_M'T$ and (b) χ_M'' against temperature T for a frozen solution of $Tb[(C_{12}H_{25}O)_8Pc]_2$ in eicosane (on the left). Plots of (c) $\chi_M'T$ and (d) χ_M''against temperature T, of $[TbPc_2]^0$ diluted in $[YPc_2]^0$ (on the right).[48]

The first dilution clearly proves that the upward temperature shift of the magnetic relaxation phenomena is an intrinsic molecular property of $[TbPc_2]^0$, and it is not due to long range magnetic order or intermolecular interactions between adjacent unpaired π-electrons. In contrast, the dilution of $[TbPc_2]^0$ in $[YPc_2]^0$ having an S = 1/2 ligand system with no *f* electron led to a suppression of the magnetic relaxation phenomena. These observations show that the presence of unpaired π electronic systems in neighbor molecules does not cause upward temperature shift of $[TbPc_2]^0$, but rather reduces the relaxation time of the Tb complex.

Transition-metal SMMs can manifest a magnetization hysteresis in addition to the magnetization relaxation effect observed in an ac susceptibility measurement.

This concept can be applied also at a lanthanide SMMs. **Figure 1.19** shows a clear hysteresis behaviour of the anionic Tb complex diluted in the diamagnetic matrix. It is interesting to note that the value of the magnetization in the descending path from H = 1.6 T to H = 0 T is greater than the corresponding value in the ascending path from H =0 T to H =1.6 T. This indicates that the relaxation time for the lower |H| region is relatively shorter than that for the higher |H| region. Moreover in this case we cannot observed the characteristic step structures[49] caused by the "*resonant tunneling*" process typical of some transition-metal-cluster SMMs, like Mn_{12}. In fact because of the large energy difference between the lowest and second lowest substates, energy-level crossing does not occur under the magnetic field.

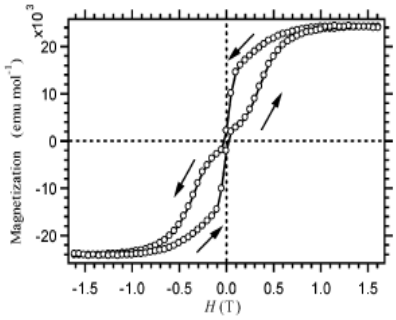

Figure 1.19: Magnetization vs field plot measured at 1.7 K for a powder sample of $[TbPc_2]^-$ [49]

Recently Veciana and co workers [47] put in evidence the difference in the dynamics of the magnetization relative to the coercive field of the anionic, neutral and cationic Tb-double decker (**Figure 1.20**). In fact the field dependent MCD of $[TbPc_2]^0$ recorded as a frozen solution exhibits a larger coercive field (1.6T) than $[TbPc_2]^{+/-}$. The derivatives of the hysteresis cycles of $[TbPc_2]^{+/0/-}$ show features (at ca. 0.4-0.5 T) that may arise from quantum tunneling effects, although the sharp decrease in the gradient at zero field strongly indicates that in all three systems there is relatively little tunneling at zero field. The relatively smooth profile of the hysteresis of $[TbPc_2]^0$ suggests that tunneling is not dominant in this complex when compared to $[TbPc_2]^{+/-}$.

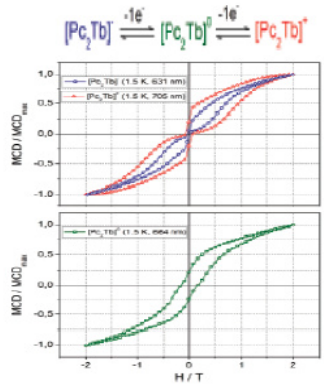

Figure 1.20: Hysteresis curves of the normalized MCD intensity vs B recorded at 1.5 K of $[TbPc_2]^{+/-}$ (top) and $[TbPc_2]^0$ (bottom).[47]

In the next chapter we shall describe the most common surface deposition techniques employed for SMMs.

Chapter 2.

Single Molecule Magnets on surfaces

2.1. Introduction

In order to take advantage from the Single Molecule Magnet behavior described in the first Chapter and to develop innovative devices, the fabrication of molecular nanostructures has been proposed and investigated by controlling at the nanoscale level the deposition of SMM on surface.[7, 50-52] For this reason many research groups have undertaken the investigation of the deposition methods whose choice depends on the chemical structures and stability of molecules and substrates.[12] Moreover, since the interactions between the molecules and the metallic or magnetic substrates could influence the molecular orientation or the magnetic behavior it has been essential to expand the study using surface sensitivity techniques thus allowing the investigation on the deposited molecules from the morphological, chemical and magnetic points of view. A morphologic analysis can be obtained by using the Scanning Tunneling Microscopy (STM) and Atomic Force Microscopy (AFM) techniques, while the chemical inspection of the deposited films can be carried out by exploiting X-ray Photoelectron Spectroscopy (XPS) or time-of-flight secondary ions mass spectrometry, ToF-SIMS. The crucial point is in fact to demonstrate that magnetic molecules remain intact on the surface. This is of paramount importance for SMMs, which are complex, often fragile structures based on coordination bonds. However the most critical point is the investigation of their magnetic properties at the nanoscale. In this sense many techniques have been developed. They can be grouped in two classes: the scanning probe techniques[53] able to provide spatially resolved information on the magnetic properties, namely MFM (Magnetic Force Microscopy) [54], SP-STM (Spin Polarized STM), SHPM (Scanning Hall Probe Mircroscopy) and ESN-STM (Electron Spin Noise STM techniques) and the spectroscopic ones based on the absorption of polarized light (Magnetic Circular

Dichroism, MCD and X-ray Magnetic Circular Dichroism, XMCD). Up to now, conclusive reports have been provided only using these non-local techniques, we also employed in this thesis.

In this chapter we shall briefly summarize the most important deposition methods reported in literature to deposit the two principal derivatives described in this thesis work: Fe_4 and $TbPc_2$ SMMs, while we postpone the description of the magnetic investigation of the molecule on surface to the three **Chapters 4, 5, 6**. Here we focus our attention on three different strategies based on a *wet approach*,[55-56] where the molecules are deposited on surface from a solution, a *physical approach* [57-58] like evaporation, Pulsed Laser Deposition (PLD) [59], Matrix Assisted Pulsed Laser Evaporation (MAPLE) [60] based on the Ultra High Vacuum apparatus, and a *mixed approach* like spray deposition[61] techniques that take advantage from the stability of the molecule in a solution and the use of a better control of surface cleanliness allowed by an UHV condition.

2.2. Self assembly of monolayer from solution

The easiest way to assemble molecules on a surface is through direct deposition of unmodified molecules physiosorbed on a native substrate *via* non-specific interactions (e.g. Van der Waals forces). Deposition is carried out either by simply *drop casting* a very dilute solution on the substrate (followed by solvent evaporation) or by dipping the substrate in a dilute solution (followed by careful cleaning with fresh solvent and drying) (**Figure 2.1 a**).

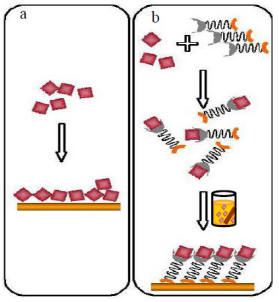

Figure 2.1: Approaches for deposition of magnetic molecules by **(a)** drop casting of non-functionalized molecules from diluted solutions; **(b)** self assembling of pre-functionalized molecules with suitable anchoring groups for specific surfaces.[62]

This method is most used when the molecules are not functionalized with organic group able to react with the surface forming for example a covalent bond. On the other hand sometimes the cleaning process could be not sufficient for the creation of a monolayer and the formation of aggregates results from the process. Moreover, since the molecules are not anchored to the surface by specific interactions but only physisorbed, sometimes the temperature could influence the mobility of the molecule on surface. In literature are principally presented examples applied on simple molecule like porphyrins[63] and phthalocyanines[64] metal complexes or system containing minor modification of their molecular structure allowing a better assembling on the surface, like in the case of the double-decker [Tb(phthalocyanine)$_2$] complexes substituted with alkyl chains that promote a bidimensional ordering and a greater thermal stabilities.[64] The STM investigation reveals the individual molecule on surface and the adsorption of the phthalocyanine molecules with their molecular plane parallel to the graphite surface resulting in the orientation of the preferential magnetization axis on the surface (**Figure 2.2**). Moreover the use of double-decker complexes with longer alkyl chains enhances both intermolecular interactions and the adsorbate-substrate interactions playing in this way a critical role in the organization and stabilization processes.

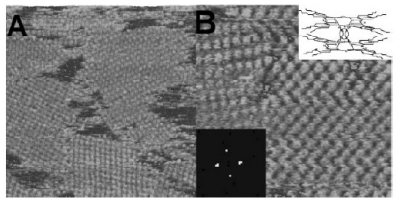

Figure 2.2: (a) STM image of various domains presenting a 2-fold symmetry package. **(b)** 20 × 20 nm magnification of one of the areas. The inset corresponds to the Fourier Transform from the larger scale fields. [64]

Covalent interactions between the molecules and the substrate in principle should guarantee a good stability of the deposit, from the morphological and chemical point of view. Nevertheless this requires the chemical effort to modify the molecules introducing an opportune ligand able to anchor the molecule on specific surfaces (**Figure 2.1 b**). For example in order to anchor Fe_4 and Mn_{12} SMMs on a gold surface a modification of the molecule has been necessary introducing in the molecules organic ligand functionalized with thio-group.[50, 65]In this case it has been important to study the deposition as function of different

parameters for example changing the ligand length that connected the surface to the SMM core.

Examples involve Fe_4 SMM containing ligand functionalized by the tio-group able to link the molecules on gold surface and trialchol used to stabilize the tetrairon core connected by aromatic or aliphatic chain. Thanks to a synthetic effort a new family of Fe_4 SMMs ($[Fe_4(SMe\text{-}PhPh\text{-}C(CH_2O)_3)_2(dpm)_6]$,[66] $[Fe_4(dpm)_6(AcS\text{-}(CH2)_9C(CH_2O)_3)_2]$,[67] $[Fe_4(dpm)_6(CH_3S\text{-}(CH_2)_5C(CH_2O)_3)_2]$,[68] ,$[Fe_4(dpm)_6(CH_3S\text{-}(CH_2)C(CH_2O)_3)_2]$) has been synthetized. All these compound have been deposited through the Self Assembly technique and a careful study on the experimental parameters like solvent and incubation time, has been described in another thesis work in the research group.[69] In **Chapter 4** we shall underline the importance of the choice of the ligand length that could influence the orientation of the molecules on surface while lateral ordering is not achieved, as suggested by STM images as those reported in **Figure 2.3** as example. The STM images refer to $Fe_4(dpm)_6(AcS\text{-}(CH_2)_9C(CH_2O)_3)_2$, Fe_4C_9Sac, self assembled on Au(111) surface.

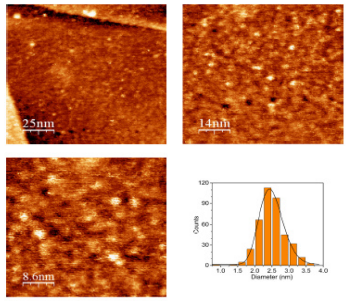

Figure 2.3: STM topography images of a typical Fe_4C_9SAc self assembled on gold substrate from a CH_2Cl_2 solution of the complex. Bottom right: statistic of the objects' diameter.

A variant of this method consists either in the surface pre-functionalization with chemical groups which provide specific docking site for the pristine molecules or in the functionalization of both molecule and surface with complementary groups that can interact one with the other.

However, the *wet deposition* techniques requires the stability of the surface in solution while most devices used in molecular spintronics are based on the use of reactive metallic surface such as metallic cobalt. For this reason it is important to develop ultra high-vacuum (UHV) deposition and *in situ* characterization techniques. Moreover UHV-compatible *physical deposition* would also be particularly useful for the creation of multi component nanostructures based on SMMs and realized with standard micro- and nanoelectronic technologies. For

example, at variance with solution-based techniques, thermal deposition (**Figure 2.4 a**) does not rely on the chemical properties of the surface, allowing for a wider choice of the substrates for a better control of surface cleanliness and provides layer thickness control. Its major drawback is that it requires the stability of molecules to the thermal treatment.

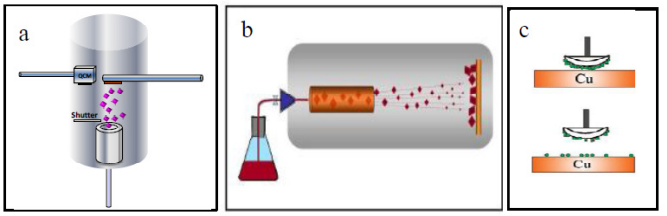

Figure 2.4: Scheme of the deposition chamber of molecular adsorbates at surfaces in a vacuum environment using thermal evaporation **(a)** vacuum spraying **(b)**[62] dry-imprint method **(c)**. [46]

In fact, most polynuclear compounds have a limited thermal stability and only few volatile cluster comprising exclusively pivalate or β-dichetonate ligands [70-72] are reported. Attempts to deposit more complex molecular architectures like SMMs using physical methods had only partial success. Thermal evaporation, for instance of the archetypal compound Mn_{12}-ac, is not feasible because they are thermally labile. For this reason, softer variants of the traditional evaporation technique have been proposed, like Pulsed Laser Deposition (PLD), [59] Matrix Assisted Pulsed Laser Evaporation (MAPLE) [60] and vacuum-spraying. In the latter approach, used by Moroni *et al.* to deposit films of Mn_{12}-ac, a solution of the complex is injected in a high vacuum chamber through a fast acting pulsed valve (**Figure 2.4 b**).[61] Rapid evaporation of the solvents brings clusters to the vapour phase under very mild conditions. The demonstration that SMM properties are conserved after a thermal vacuum deposition process has been only recently demonstrated in few cases like lanthanide bis-phthalocyaninato ($LnPc_2$) complexes which were the first samples investigated by STM. However evaporation deposition procedure of the $LnPc_2$ molecules on surface could produce some secondary products due to the thermal treatment, despite the more pronounced stability of this molecular structure compared to other polynuclear SMMs. This result was evidenced by Katoh *et al*. who described the STM investigation of a thermally evaporated MPc_2 monolayer deposited on Au(111) substrate.[44]

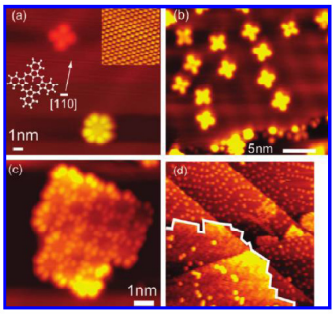

Figure 2.5: STM images of $TbPc_2$ and TbPc. **(a)** single molecules of TbPc (upper) and $TbPc_2$ (lower). An atomic image of the Au(111) is shown in the inset. **(b)** TbPc molecules on the terrace part of the Au(111) surface (25×23 nm^2). **(c)** $TbPc_2$ film composed of 21 molecules (7.8×7.8 nm^2). **(d)** Coexisting $TbPc_2$ island and isolated TbPc molecules. [44]

Here we report in **Figure 2.5** the STM imagines of the evaporated $TbPc_2$ molecules where it is possible to distinguish two types of isolated molecules containing four lobes (as showed in the upper part of **Figure 2.5 a**) and eight lobes (as showed in the lower part of the **Figure 2.5 a**). Moreover the authors estimated the heights of both molecules: 140 pm for the four-lobe and 400 pm for the eight-lobe molecules. In **Figure 2.5 b**, a group of the isolated four lobe molecules adsorbed on the terrace part of the substrate are shown; while in **Figure 2.5 c** the formation of islands of the eight lobe molecules is observed. In **Figure 2.5 d**, is shown the coexistence of square lattice islands and isolated molecules. The measured height of ~140 pm of four lobe molecules is in the range of height of isolated molecules of CoPc, FePc, and metal free Pc, which have been observed at cryogenic temperature with a cross-like shape in the topographic STM images similar to the ones showed in **Figure 2.5 a**. Thus, the authors concluded that the four-lobe molecule corresponds to either a TbPc or a Pc molecules produced by a fragmentation of $TbPc_2$ in the sublimation process. A height value of ~400 pm obtained in the eight lobe molecules is consistent with the size of $TbPc_2$ molecules determined by using X-ray Diffraction analysis of single crystals. A rough estimation of the ratio of the MPc_2 and MPc molecules from **Figure 2.5 b** is 4:1. The molecule shape and the bonding configuration of **(a)** Pc, **(b)** MPc, and **(c)** MPc_2 molecules are illustrated in **Figure 2.6**, and the four-lobe molecules should correspond either to **(a)** or **(b)**, while the eight lobe molecules should correspond to the configuration shown in **Figure 2.6 c**.

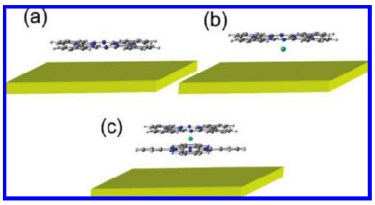

Figure 2.6: Schematic illustrations of the adsorption configurations of (a) Pc, (b) MPc, and (c) MPc_2 on the Au (111) substrate. [44]

A variant of this method is the dry imprint technique used by Vitali et al. to deposited a sub-monolayer of $Tb(phtalocyanine)_2$ molecules in ultrahigh vacuum (UHV) conditions. [46] Specifically, a soft applicator, formed by a fiberglass bundle coated with a fine-grained powder of $TbPc_2$ crystals, is brought in gentle contact with the surface.

2.3. Chemical characterization of the deposited molecules

In the examples reported up to now, the characterization of the layers has relayed mainly on the topographical insight provided by STM technique. However, when the molecules contain reactive moieties necessary to link covalently on surface or if they are deposited using a physical method in UHV condition it is important to verify the intactness of the compound on surface using sophisticated tools suited for the surface investigation. In particular in this thesis work we have checked the chemical composition of the SMMs adsorbates on surface by using Time of flight Secondary ions mass spectrometry, ToF-SIMS, because it is an extremely powerful tool for the inspection of the thick film and above all for the monolayer deposit on surface. This technique consists in the ionic bombardment with gold ions from a liquid-metal primary ion source. The topmost layers of the deposit release adsorbed molecules or fragments in the form of secondary ions. The mass of these ions can be obtained by measuring the exact time at which they reach the detector (time of flight). The adsorbed molecules or their fragments are thus characterized as in a mass spectrometer with counting the occurrence of ions as function of the *m/z* ratio. In fact the time of flight is proportional to the mass of the fragment and thus the ions with lower *m/z* reach the detector faster than the ions with higher *m/z*. For the investigation of the monolayer or submonolayer coverage it is important to control the dose of the primary ions working in the so called "*static condition*" that allow the analysis of the only uppermost monolayer.

In fact, if the dose of the primary source is too high few layers could be removed because of the big erosion rate (*"dynamic condition"*) (**Figure 2.7**).

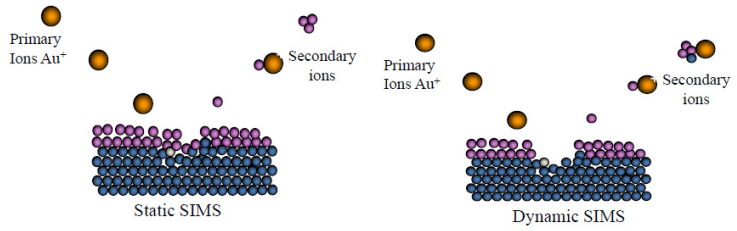

Figure 2.7: Scheme of the ionic bombardment used in the ToF-SIMS technique in static and dynamic condition.

Application of this technique to complex systems, like Mn_{12} and Fe_4 cluster,[73] has provided useful information because the ionization mechanism used by this type of spectrometry is particularly suited for the desorption of non-fragmented bulky molecules that are kept together by coordination bonds. For example the ToF-SIMS measurements on Fe_4C_9Sac cluster whose STM topography was reported in **Figure 2.2**, showed in bulk phase and in monolayers quite difference in the fragmentation pattern revealing the presence in the monolayers of an oxidized molecules, with one sulphur atom that loses the acetyl group and becomes a sulphonate. However the ToF-SIMS technique is not able to quantify this two fractions. This problem can be overcome by using a combination of electron spectroscopic techniques such the photoelectron spectroscopy (UPS or XPS) with static SIMS.[73]

2.4. Molecular spintronic devices

At the beginning of this chapter we have mentioned the use of SMMs in the emerging molecular spintronics field. Recently our research group has started a collaboration with the spintronics group of Prof. V. A. Dediu in order to investigate the spin transport properties of SMMs in the spin valve device. In this paragraph we will describe shortly the principles of the spin transport phenomena.

Spintronics was born with the discovery of the giant magnetoresistance by Peter Grunberg and Albert Fert research groups that received for their discovery and the contribution in the spintronics field the Nobel Prize for Physics in 2007. However we can also recall as starting point of this research field in the 1936, when Mott[74] for the first time proposed the influence of the spin in the mobility

of the electrons in a ferromagnetic metal. In 1986 Grunberg [75] observed the existence of a ferromagnetic interlayer between the Fe and Cr layers and revealed that by applying a magnetic field the orientation of the magnetization could change from parallel to antiparallel, thus leading to a change in electrical resistance. Thanks to this in the 1988 giant magnetoresistance was dscovered indipendently by both the Fert and Grunberg groups.[76-77] Rapidly, these results attracted attention for their fundamental interest and for the many possibilities of application to magnetic sensors for the automotive industry, and to the read heads of hard discs that led rapidly to a considerable increase of the density of information stored in discs.

Here we focus our attention on system formed by two layer of ferromagnetic material sandwiching an organic semiconductor and we will report the most representative example of the spintronic injection and transport in organic semiconductor. These kind of devices are called "*spin valve*" because are formed so that the magnetic moment of one of ferromagnetic layer is very difficult to reverse in the applied magnetic field, while the moment of the other layer is easier to reverse and then acts like a valve control that can be manipulated by an external magnetic field. In particular when the magnetizations of the two ferromagnetic metals are in an aligned state, the resistance is low, whereas the resistance is high in the anti-parallel state (**Figure 2.8**).

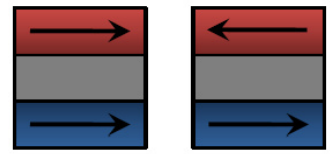

Figure 2.8: Simple scheme of spin valve device composed by two ferromagnetic layers (blue and red) separated by the organic semiconductor (gray layer). The arrows represent the magnetization of the two metals: parallel on the left and anti parallel on the right.

Recently Dediu and co-workers summarized the main experimental results obtained in the last years on the spin injection and transport in different organic semiconductors (OSCs) material. OSCs are mainly families of π-conjugated molecules, merging a considerable delocalization of carriers inside the molecule with weak Van der Waals[78] intermolecular interactions, which considerably limit the carrier mobility. The selected ferromagnetic materials were a Co layer and the manganite ($La_{0.7}Sr_{0.3}MnO_3$, or LSMO) used for its highly polarizability feature.

In particular the author consider the device formed by the *tris*(8-hydroxyquinoline)Aluminium(III) (Alq_3) semiconductors and the LSMO and cobalt electrodes as an important step for the fabrication of a vertical spin-valve device because it is characterized by an antiparallel magnetization configuration but a lower resistance that usually corresponds to parallel magnetization of the electrode. The spin transport mechanism described by the authors involve the lowest unoccupied molecular level (LUMO) and the highest occupied molecular level (HOMO). This is clearly explained by the energy diagram of the LSMO/Alq_3 /Al_2O_3 /Co. (**Figure 2.9**). In fact the metal/Alq_3 interfacial barriers aligns the LUMO level of Alq_3 with the spin-down bands of both LSMO and Co, considering similar Fermi energy (*EF*) values for Co and LSMO (*EF*=4.9–5 eV). Thus the spin-up electrons injected by either the LSMO (negative voltage) or the Co electrode (positive voltage), propagate by the hopping mechanism along the organic material where they gradually lose part of their spin polarization. Eventually, the electrons tunnel from the LUMO of Alq_3 into the spin-down bands of either the Co or LSMO electrode, respectively.

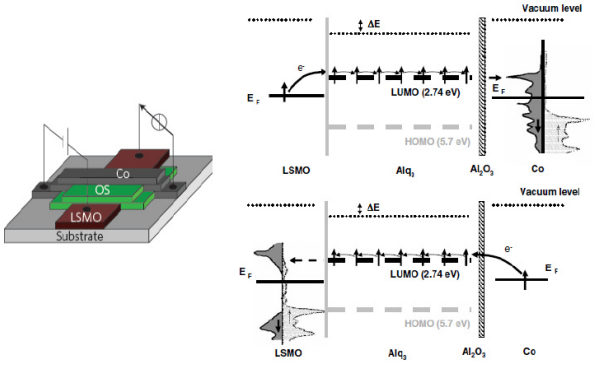

Figure 2.9: on the left a sketch of spin device as published by Dediu *et al.,* on the right Energy diagram for a $La_{0.7}Sr_{0.3}MnO_3$ /Alq_3/tunnel barrier/Co organic spin valve at V = 0V. Upper panel: Injection of spin-up electrons from LSMO into Alq_3 and the alignment of LUMO with the Co spin-down band. Lower panel: Injection of spin-up electrons from Co through the Al_2O_3 barrier into Alq_3 and the alignment of LUMO with the LSMO spin-down band. The light gray represents the spin-up bands, while the dark gray represents the spin-down ones.[78-79]

DFT calculation on Fe_4 complexes reveled to have a Fermi Energy value able to be used as spin transport in a spin valve device.[80] For this reason our group started to consider the possibility to develop a Fe_4-based devices and then we

began to investigate the magnetic properties of Fe_4 SMM on LSMO and Co substrate and to verify the stability of Fe_4 in presence of LSMO in order to exclude that these substrates can modify the chemical and magnetic properties of the molecules. In particular in **Chapter 5** we will describe the magnetic properties and the electronic structure of the interface between Fe_4 SMM and manganite substrate in order to understand if the presence of the SMM can influence the spin injection of the LSMO electrode.

2.5. Conclusions

The field of molecular magnetism is undergoing rapid changes. A major challenge is now the investigation and organization of SMM on surfaces, for their electric or magnetic addressing using SPM methods and for their wiring into nanodevices. However, much work remains to be done to ensure structural and electronic intactness, to control the interaction with the substrate and to drive the formation of completely ordered monolayers or submonolayers comprising iso-oriented molecules over large areas. Moreover in order to efficiently develop molecular spintronics, the library of molecules and of substrates must now be rapidly enlarged. For this reason we have expanded our study to $TbPc_2$ molecules and we have deepened the investigation on Fe_4 SMM since it shows a more robust structure compared to Mn_{12} and is able to retain the SMM behavior once deposited on surface at the monolayer level.[81]

In particular in this thesis work we attempted to face a challenge trying to deposit by thermal evaporation in UHV condition Fe_4 SMMs on different substrates laying the foundations for the creation of multicomponent nanostructures based on SMMs.

Chapter 3.

Thermal Deposition of a thick film of Fe_4 Single Molecule Magnets

3.1. Introduction

As describe in the first two Chapters, the interest for the Single Molecule Magnets has shifted toward the potential incorporation of magnetic molecules into nanodevices for spintronic applications. This development is based on the fabrication of molecular nanostructures and on the investigation of molecular properties at the nanoscale. This last goal was achieved by our research group developing SMMs grafting on specific surfaces by using opportune functionalizations in order to form monolayers deposits directly from solution.[81] On the other hand the Ultra-High Vacuum (UHV)-based deposition techniques, described in the second chapter, allow to extend the investigation to reactive surfaces, e.g. ferromagnetic metals, and to work in cleaner conditions as usually required for the development of the devices. In particular the standard thermal deposition technique in UHV conditions, is a well established method that provides layer thickness control, but requires first of all molecules stable to the thermal treatment.

In this chapter we will describe the evaporation process of a class of tetrairon (III), Fe_4, containing different tripodal ligands and we will report the chemical and magnetic characterization of the deposited films by combined the use of time-of-flight secondary ion mass spectrometry, ToF-SIMS, superconducting quantum interference device (SQUID) magnetometry, high frequency electron paramagnetic resonance (HF-EPR) and alternating current (ac) susceptibility measurements. In particular we will focus our attention on the deposition of thick films of Fe_4 and we will demonstrate that for some of them it is possible to

evaporate films of different thickness keeping intact the Single Molecule Magnets behaviour.

3.2. Thermal evaporation technique

Synthesis. Fe_4 compounds were synthesized replacing the methoxo bridge in the standard precursor, $[Fe_4(OMe)_6(dpm)_6]$, Fe_4std (**Figure 1.4**), where Hdpm is the dipivaloylmethane, with the tripodal ligands, H_3L = R-$C(CH_2OH)_3$. The reaction, proceeded smoothly in organic solvents and allows to modulate the molecular structure and magnetic parameters of the clusters. In **Figure 3.1** are reported all the tripodal ligands used for the synthesis of Fe_4 molecules evaporated on different substrates, selected on the base of the following investigation. In particular we choose the Al foil for the chemical analysis carried out with ToF-SIMS, the diamagnetic LiF and Kapton substrates for the magnetic measurement and the soda lime glass for the morphological study by AFM.

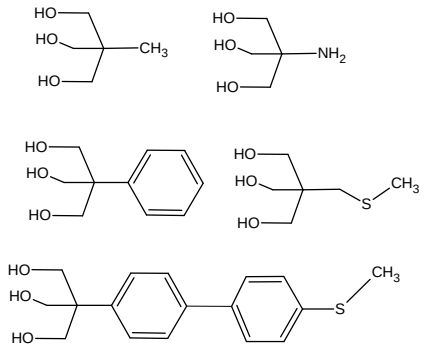

Figure 3.1: Tripodal ligands used in this thesis.

The experiments relative to the thermal evaporation deposition were conducted at the Laboratory of Dr. Buatier de Mongeot of the Department of Physics in Genova where I spent the period necessary for performing the described experiments. Film depositions were performed in an unbaked HV apparatus pumped to a pressure in the 10^{-6} mbar range. In **Figure 3.2** a simple scheme represents the chamber used for the evaporations. The evaporation chamber includes Knudsen cell useful for the preparation of organic films in high vacuum systems. The heating element allows to produce an uniform and constant molecules flux in order to produce an homogenous film. In particular it consists of a furnace containing a crucible of quartz and a single Tantalium heater filament. This part is designed in a special way to keep the upper part of the cell at a slightly higher temperature in order to avoid the tendency of the molecules to condense at the outlet orifice. The temperature of the furnace is monitored by a

K-type thermocouple. The thickness of the film has been monitored by means of a quartz-crystal-microbalance (QCM), measuring the change in frequency of the quartz that can be correlated *a posteriori* to the actual thickness of the film by means of AFM measurements on a scratched sample, thus allowing to determine the actual deposition rate, expressed in nm per second. Finally, thanks to a dedicated software, it was possible to follow the time evolution of the crucible temperature, the pressure and the deposited thickness during the evaporation procedures.

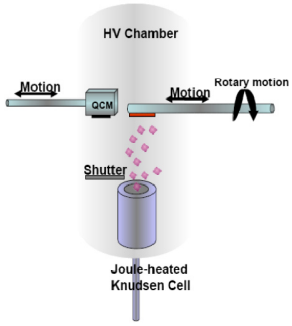

Figure 3.2: Schematic UHV-deposition chamber used to prepare Fe_4 films on different substrates.

In the experimental section (**Chapter 7**) are described the details relative to the instruments used for the ToF-SIMS experiments, the magnetic measures and the AFM images.

3.3. Thermal deposition in High Vacuum condition of a thick film of Fe_4 SMMs

3.3.1. Thermal evaporation of Fe_4std SMM

Thermal evaporation parameters. $[Fe_4(OMe)_6(dpm)_6]$ compound, Fe_4std, described in the first Chapter, was deposited using the thermal evaporation chamber in HV conditions. Following each evaporation parameters, like pressure, temperature and the deposited thickness, during the deposition procedure we can get a first indication on the feasibility of the evaporation process. The **Figure 3.3** shows the presence of four peaks of pressure at different temperatures:100°C, 200°C 230°C and 240 ° C. We attributed the first one to the degassing process of the crucible and the second one to some volatile fragments of Fe_4std that was not detected by the QCM. Moreover the other two peaks well corresponded to the signals detected by the microbalance thus revealing the presence of two different

compounds deposited on the substrate. This behavior could indicate a decomposition of Fe_4std compound due to the high temperature of the thermal evaporation process. Finally at the end of the thermal evaporation we noted the presence of a dark residue in the crucible which clearly indicates a partial decomposition of the molecules caused by thermal process.

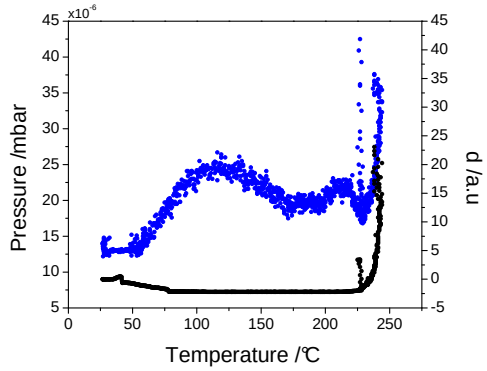

Figure 3.3: Pressure(blue line) and thickness (black line) trend as function of the temperature recorded during Fe_4std thermal evaporation.

This hypothesis was confirmed by the ToF-SIMS analysis of the evaporated film on Al foil able to give information on the chemical composition of the sample. In particular the comparison between the evaporated thick film and the powder pressed down on Indium foil evidenced many differences. In fact as shown in **Figure 3.4** and **Figure 3.5** we observed fist of all a different fragmentation pattern of both negative and positive ions reported for the evaporated thick film and the pristine powder. In particular the negative ions spectra of the evaporated Fe_4std film (**Figure 3.4**) evidenced the absence of peaks in the high mass region including the region of the molecular ion peak at *m/z* 1508 and no peaks were detected above *m/z* 605. In the negative ion distribution of both evaporated film and powder we detected the low mass peaks at *m/z* 16 and *m/z* 183 attributed to ion fragments $[O]^-$ and $[dpm]^-$ maybe formed as a consequence of the procedures of the ToF-SIMS technique. The low mass region (*m/z* 200 and 600) evidenced the first differences between the two samples: in fact the only signal detected in the evaporated sample at *m/z* 288 and attributed to the $[Fe(dpm)(OCH_3)H_2O]^-$ fragment was absent in the pristine material in which were detected many other signals at *m/z* 301, 404 and 587 assigned to $[Fe(dpm)(OCH_3)_2]^-$, $[Fe_2(dpm)(OCH_3)_3{+}O]^-$, and $[Fe_2(dpm)_2(OCH_3)_3 + O]^-$ fragments. In the high mass region (*m/z* 600-1000) of the deposited film the only peak observed at *m/z* 605 was attributed at the mononuclear compound

$[Fe(dpm)_3]^-$ that we consider the most important species generated as a consequence of the evaporation process, that is lacking in Fe_4std powder spectrum.

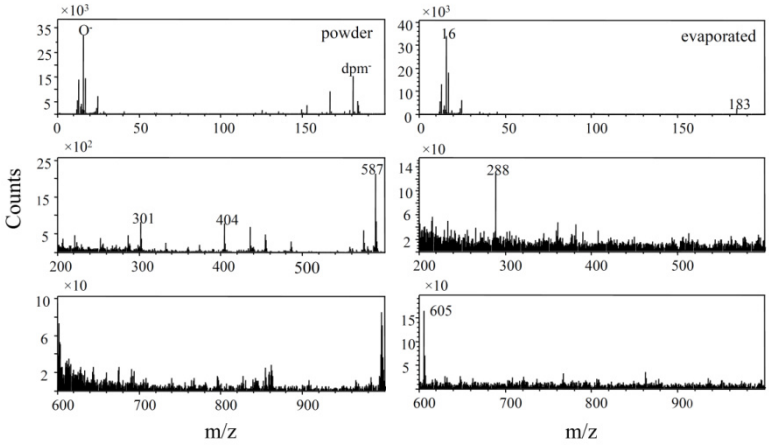

Figure 3.4: Negative ToF-SIMS spectra in the mass region between *m/z* 0-1000 of Fe_4std film deposited by thermal evaporation on Al and of the powder press down on In foil.

In the positive ions spectra (**Figure 3.5**) the situation did not change: in the thermal evaporated sample the peak detected at *m/z* 57 was assigned to the ter-Butil group $([C\text{-}(CH_3)_3]^+$ lost from the dpm ligand; while the peaks at *m/z* 239, *m/z* 365, *m/z* 422 were assigned respectively to the fragments containing the Fe ion and the dpm ligand: $[Fe+dpm]^+$,$[Fe+dpm+C_7H_{10}O_2]^+$ and $[Fe(dpm)_2]^+$. In the high mass region the only two peaks containing Fe_4 core structure observed at *m/z* 1004 and *m/z* 1187 were attributed to the fragment $[Fe_4(dpm)_3(C_{10}H_{16}O_2)(OCH_3)_2H]^+$ and $[Fe_4(dpm)_4(C_{10}H_{16}O_2)(OCH_3)_3H]^+$. All these signals were revealed also in the positive ion spectra of the pristine material that show in addition many other peaks, thus confirming the differences of the fragmentation pattern of the two samples.

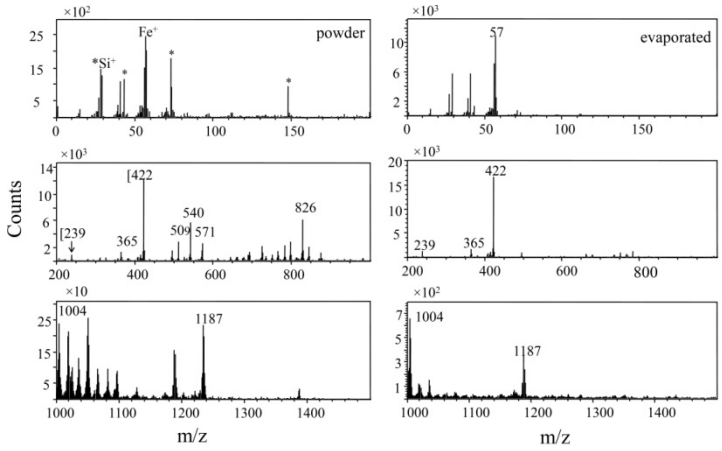

Figure 3.5: Positive ToF-SIMS spectra in the mass region *m/z* 0-1500 of Fe_4std evaporated film on Al and of the powder press down on In foil.

This first data did not deterred us, in fact we know that the replacement of the six methoxyl ligands with the tripodal ligand, in addition to enhanced magnetic properties, makes Fe_4 structure much more stable and robust.

3.3.2. Thermal evaporation of Fe_4Me SMM

Thermal evaporation parameters. Following the same deposition procedure used for Fe_4std compound, we evaporated $Fe_4(dpm)_6(CH_3\text{-}C(CH_2OH)_3)_2$, Fe_4Me complex. In **figure 3.6** is reported the pressure and deposition rate as a function of the temperature. Fe_4Me started to evaporate at 250°C and except for a weak peak of pressure observed at 150°C, maybe due to the evaporation of some volatile fragments, we could observe only one peak that corresponds to the correct evaporation temperature. Also in this case the presence of a dark residue attributed to the decomposed compound was present in the crucible at the end of the thermal process.

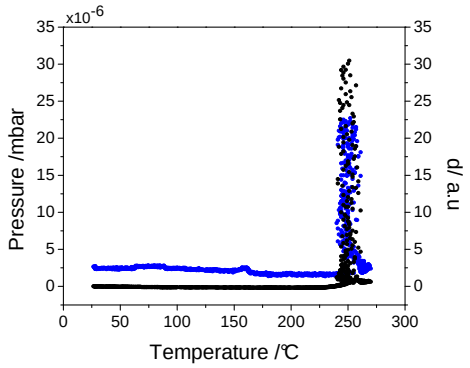

Figure 3.6: Pressure (blue line) and thickness (black line) trend as function of the temperature recorded during Fe_4Me thermal evaporation.

ToF-SIMS. Looking at the ToF-SIMS analysis of Fe_4Me evaporated film on Al foil we realize immediately the presence of peaks in the high mass region in both positive and negative ions spectra that could indicate the chemical integrity of the cluster. In this case, contrary to what observed for Fe_4std compounds we obtained the same fragmentation patterns for both pristine powder and evaporated films. Moreover surprisingly we noted in the high mass region of the negative ions (**Figure 3.7**) the peak at *m/z* 1556 that corresponds to the molecular peak ion. This indicates that Fe_4Me is more robust and resistant to the thermal treatment than the standard compound and could evaporate keeping intact the chemical composition.

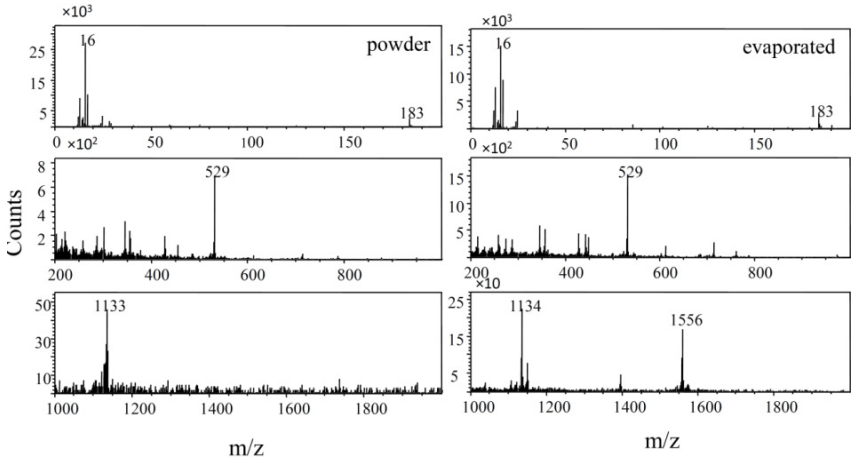

Figure 3.7: Negative ions in the region *m/z* 0-1900 of Fe_4Me thermal evaporated film and of the powder press down on In foil.

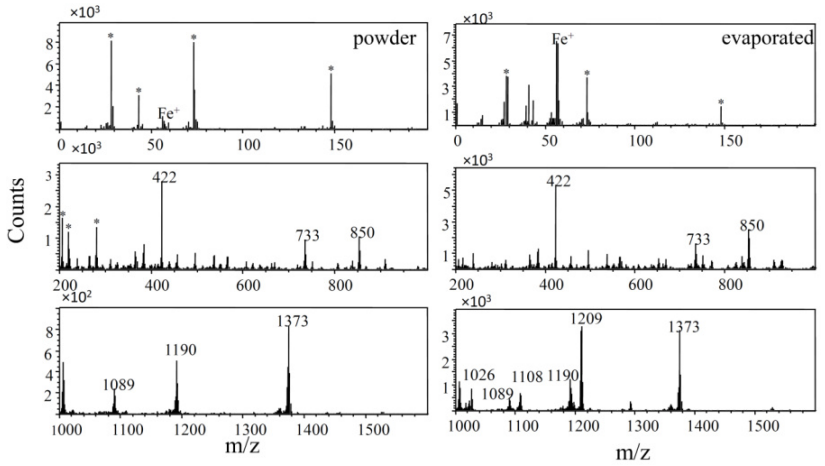

Figure 3.8: Positive ions in the *m/z* 0-1600 region of Fe_4Me evaporated film on Al foil and of the powder press down on In foil. (the signals marked with the asterisks were assigned to silicon grease contamination).

This first hypothesis was confirmed by the positive ions spectra (**Figure 3.8**) that evidenced the presence of many signals in the high mass region in which Fe_4Me compound shows their intact core structure. In particular we attributed the peaks at *m/z* 1373, 1190, and 1008 to the loss of respectively one, two and three dpm ligand molecules from the peripheral Fe ions. A similar distribution was found for different Fe_4 derivatives using electrospray ionization mass spectrometry (ESI-MS) carried out on bulk samples.[82]

Magnetic properties. The good results evidenced by the ToF-SIMS analysis encouraged us to deepen our investigation on the evaporated thick film. In particular to prove that SMM behavior was retained after the thermal deposition process, the magnetic characterization was performed on the film evaporated on diamagnetic LiF substrate (whose area was ca. 0.5×0.5 mm^2).

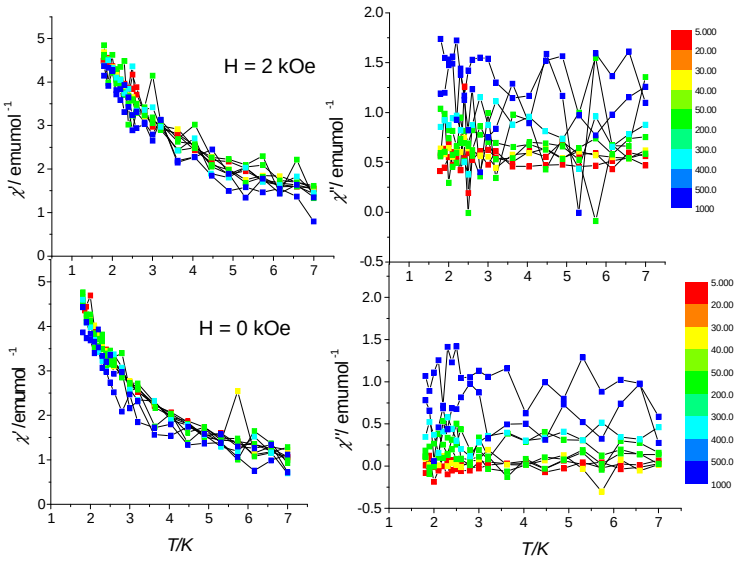

Figure 3.9: Temperature dependence of the real and imaginary components of the ac susceptibility measured for evaporated Fe_4Me in zero and 2 kOe static fields in the frequency range from 10 Hz to 10000 Hz (see color scale).

We measured the frequency and temperature dependencies of the ac susceptibility of Fe_4Me film in the frequency range 10-10000 Hz at low temperature in the zero field (**Figure 3.9**). This measure clearly indicated the absence of the frequency dependent maximum for both the real (χ',in phase) and imaginary (χ'', out of phase) components of the susceptibility as commonly observed for a Single Molecule Magnet and as described in the **Chapter1**. In order to improve the signals and confirm the absence of the maximum in the susceptibility we repeated the same experiment applying a magnetic field of 2 kOe. However, the response of the signal remained the same demonstrating that the typical behavior of SMMs was lost. This result proves that the chemical integrity detected by the ToF-SIMS is not a sufficient condition to retain the SMM behavior.

3.3.3. Thermal evaporation of Fe_4NH_2 SMM

Thermal evaporation parameters. In **Figure 3.10** are reported the pressure and the deposition thickness parameters as a function of the temperature of the crucible, recorded during the evaporation of $Fe_4(dpm)_6(NH_2\text{-}C(CH_2OH)_3)_2$, Fe_4NH_2,compound. We can observe that the evaporation starts at ca. 320°C,

higher than the other Fe_4 compounds, and that the only peak of pressure coincides with the deposition of the material on the quartz microbalance. At the end of the thermal evaporation the presence of a dark residue in the crucible was obtained.

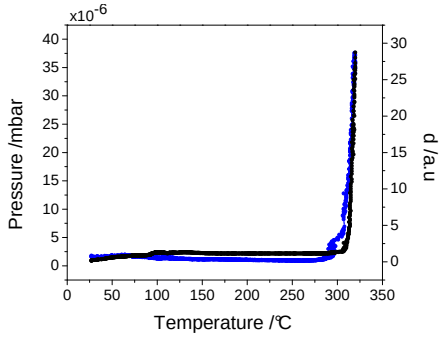

Figure 3.10: Pressure (blue line) and thickness (black line) trend as function of the temperature recorded during Fe_4NH_2 thermal evaporation.

ToF-SIMS: The negative and positive ions ToF-SIMS spectra of the evaporated film were compared with those obtained on the powder pressed down on Indium foil. The fragmentation patterns were significantly different. In particular in the negative ions region of the evaporated sample (**Figure 3.11**) were detected only few peaks at *m/z* 183, *m/z* 605 attributed to the dpm ligand molecular ion and to the mononuclear compound $[Fe(dpm)_3]^-$, respectively.

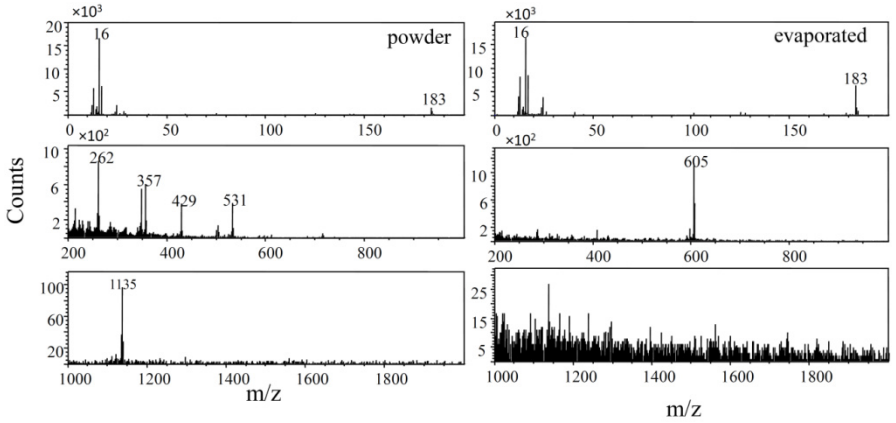

Figure 3.11: Negative ions in the *m/z* 0-1900 region of Fe_4NH_2 evaporated film on Al foil and of the powder press down on In foil.

Also in the positive ion spectra (**Figure 3.12**) we observed a different fragmentation pattern in the region between *m/z* 0 and 1000 with few peaks

detected in the evaporated sample at *m/z* 57, 365 and 422, assigned to the ter-buthyl ion, and to the fragments containing the Fe ion and the dpm ligand, $[Fe+dpm+C_7H_{10}O_2]^+$ and $[Fe(dpm)_2]^+$, respectively. The high mass region (*m/z* 1000 - 1700) revealed more similarities between the spectra of deposited film and the pristine materials, as evidenced by the peaks recorded at *m/z* 1375 and 1192 attributed respectively to the loss of one and two dpm ligands by the molecular ion. The peaks revealed at *m/z* 1345 and 1106 were assigned to the fragments $[Fe_4(dpm)_5(OCH_2)_6(CN)]^+$ and $[Fe_3(dpm)_4(OCH_2)_6(CN)]^+$. Surprisingly in the evaporated film we observed a peak with a very low intensity at *m/z* 1558 attributed to the molecular ion, which indicates that the evaporated compound was not completely decomposed.

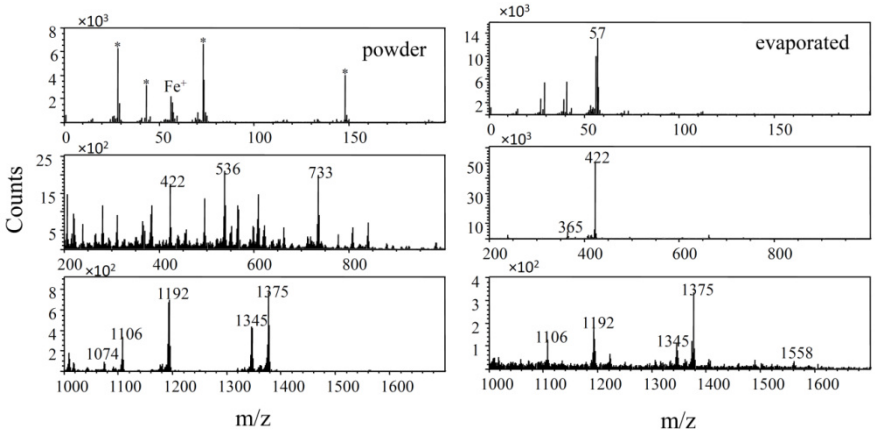

Figure 3.12: Positive ions in the *m/z* 0-1700 region of Fe_4NH_2 evaporated film on Al foil and of the powder press down on In foil.

Although we observed the presence of the molecular ion peak in the high mass region of the evaporated film, the difference revealed in the m/z 0-1000 region and the presence of the dark residue in the crucible formed after the thermal evaporation let us to conclude that the evaporated film was for the most part decomposed.

3.3.4. Thermal evaporation of Fe_4PhPhSMe

Thermal evaporation parameters. In **Figure 3.13** are reported the pressure and deposition thickness as function of the temperature of the crucible containing $Fe_4(dpm)_6((CH_3SPh\text{-}Ph)\text{-}C(CH_2OH)_3)_2$, Fe_4PhPhSMe, compound. During the evaporation procedure we observed an increase of the pressure at two different temperatures (250°C and 320°C) and for both signals the QCM was able to detect

the deposition of some material. This clearly meant that the evaporation of Fe_4PhPhSMe causes a decomposition of the molecules in at least two main compounds revealed by the microbalance.

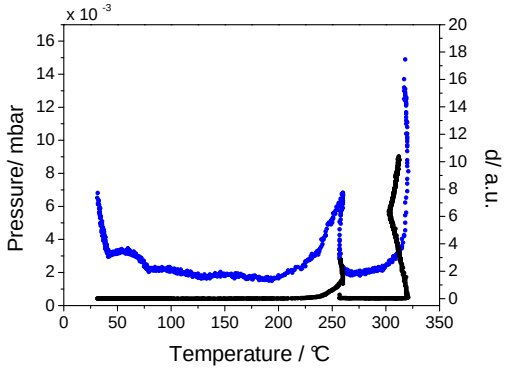

Figure 3.13: Pressure (blue line) and thickness (black line) trend as function of the temperature recorded during Fe_4PhPhSMe thermal evaporation.

ToF-SIMS: Since the thermal deposition evidenced the presence of two peaks that correspond to two different compounds we deposited separately the two products of decomposition at 225 and 300°C. In **Figure 3.14** we have reported the positive ToF-SIMS spectra where we can observe exclusively the presence of peaks at low mass. In particular all the peaks detected, *m/z* 239, 365 and 422, in the positive ions spectra were attributed to the mononuclear compounds $[Fe(dpm)]^+$, $[Fe+ (dpm) + C_7H_{10}O_2]^+$ and $[Fe(dpm)_2]^+$ confirming that it was the main product of the deposition.

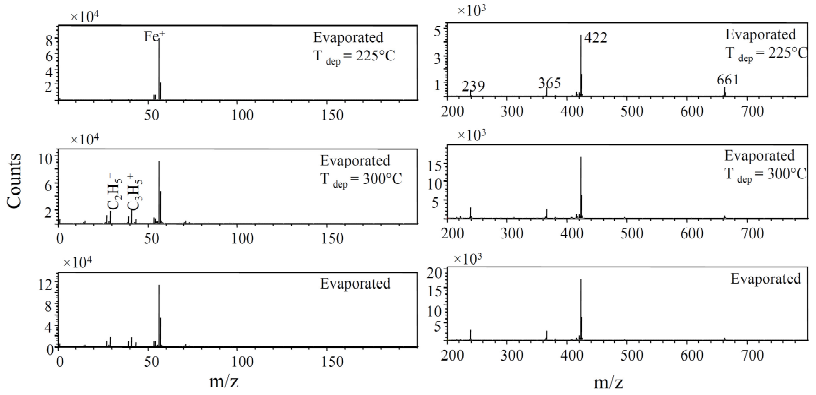

Figure 3.14: Positive ToF-SIMS spectra of Fe_4PhPhSMe film deposited by evaporation on Al in the region between *m/z* 0-700. In the top part is reported the compound evaporated at 225°C, in the middle part the compound evaporated at 300°C and in the bottom one the compound evaporated during the entire process.

Moreover we observed that the peak revealed at *m/z* 661 assigned to the $[Fe(dpm)_3(CH_2CH_3)(CHCH_2)]^+$ and present only in the first part of the deposition at 225°C disappears when increasing the temperature. This data demonstrated that the first fraction of molecules that evaporate at ca. 225°C could be attribute to the mononuclear compound $Fe(dpm)_3$.The negative ions fragments are reported in **Figure 3.15**. For all the deposition products we revealed only peaks in low mass region at *m/z* 183, 207 and 288 that were attributed to the $[dpm]^-$, $[dpm+C_2]^-$ and $[Fe(dpm)(OCH_3)(H_2O)]^-$ fragments.

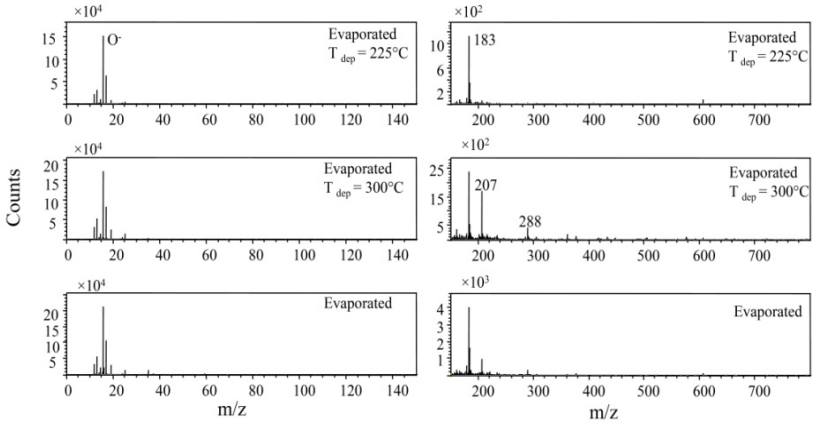

Figure 3.15: Negative ToF-SIMS spectra of Fe_4PhPhSMe film deposited by evaporation on Al in the region between *m/z* 0-700. In the top part is reported the compound evaporated at 225°C, in the middle part the compound evaporated at 300°C and in the bottom one the compound evaporated during the entire process.

The pristine material drop cast on gold (**Figure 3.16**) exhibited clearly a different fragmentation pattern respect to the evaporated compound and showed the presence of the molecular peak at 1924 *m/z* in the negative ion spectrum that confirmed the integrity of Fe_4 core structure. Peaks recorded in the positive ion spectra at *m/z* 1741, 1558 and 1375 were attributed to the lost respectively of one, two and three dpm ligands from the peripheral Fe ions.

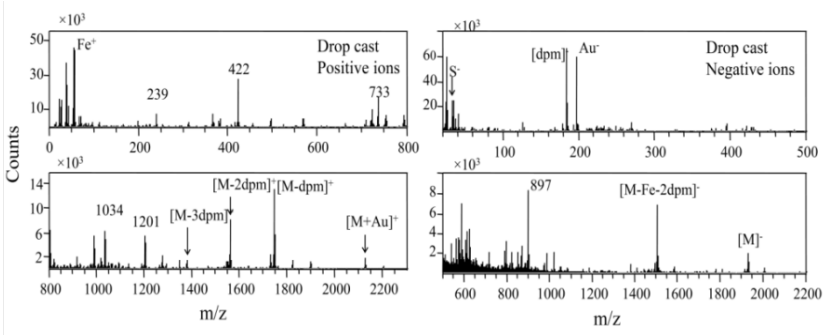

Figure 3.16: Negative and positive ToF-SIMS spectra of Fe_4PhPhSMe powder drop cast on Au from a toluene solution.

Therefore since the chemical investigation leaves no doubt on the thermal decomposition of the evaporated film, it was not necessary to perform the magnetic characterization.

3.3.5. Thermal deposition of Fe_4Ph SMM

Thermal evaporation parameters. The thermal evaporation of $Fe_4(dpm)_6(Ph\text{-}C(CH_2OH)_3)_2$, Fe_4Ph compound started at 280°C as showed in **Figure 3.17**. It was interesting to note that around 220°C the pressure increase drastically, but the QCM did not reveal any deposited materials suggesting the evaporation of some volatile impurities or organic ligands. Moreover at the end of the process we did not observe any residue, but filling the crucible with more starting material (50 mg than the 20 used in the first evaporation) we obtained a residue with the same colour of the pristine compound (orange) whose magnetic properties will be described in the following section.

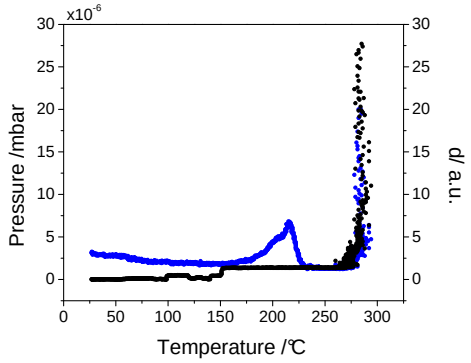

Figure 3.17: Pressure (blue line) and thickness (black line) trend as function of the temperature recorded during Fe_4Ph thermal evaporation.

ToF-SIMS. In order to determine the chemical composition of the deposited Fe_4Ph film, ToF-SIMS analysis was carried out. The negative ion ToF-SIMS spectrum of the evaporated Fe_4Ph film on Al (**Figure 3.18**) was compared with that of Fe_4Ph powder drop-cast on Au from a toluene solution. The fragmentation pattern of Fe_4Ph film was identical to those detected on the drop-cast sample and this was a first evidence of the success of the deposition process. The presence of the peak at *m/z* 1681 in the negative ion spectra was assigned to Fe_4Ph molecular ion $[M]^-$. The experimental isotopic distribution for Fe_4Ph molecular ion peak (inset of the evaporated spectrum in **Figure 3.18**) was in agreement with the expected isotopic pattern shown in the inset of the drop cast spectrum (**Figure 3.18)**, thus increasing the confidence in the identification. In addition, besides the molecular ion peak, an intense peak at *m/z* 1259 was observed in the high mass region, which can be assigned to the molecular ion fragment formed by the loss of one peripheral $[Fe(dpm)_2]^+$ group. The negative ion ToF-SIMS spectra of Fe_4Ph in the low mass region showed a significantly intense peaks detected at *m/z* 183 and *m/z* 653 and assigned to the $[dpm]^-$ and $[2Fe + dpm + 2L]^-$ (L=Ph-$C(CH_2O)_3$) ion fragments, respectively.

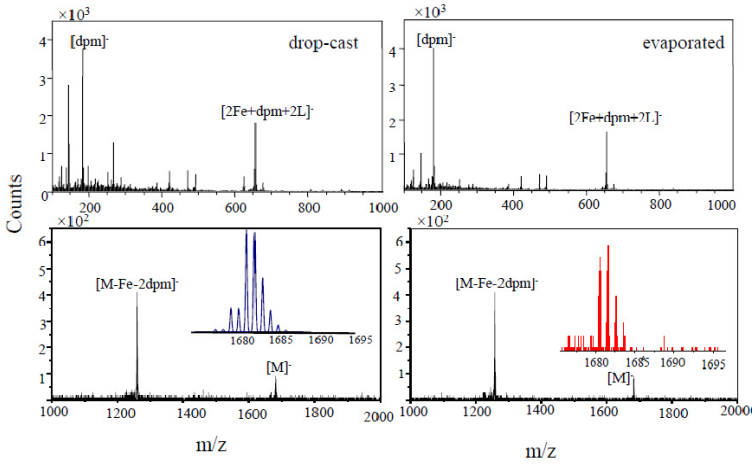

Figure 3.18: Negative ToF-SIMS spectra of Fe_4Ph film deposited by evaporation on Al and of the powder drop cast on Au from a toluene solution. The insets show the isotopic pattern detected for Fe_4Ph molecular ion peak $[M]^-$ (in the evaporated film figure) and the theoretical isotopic pattern for Fe_4Ph molecular ion peak (in the drop cast figure).

The positive ion ToF-SIMS spectrum of Fe_4Ph evaporated film (**Figure 3.19**) was also compared with the spectrum of drop-cast Fe_4Ph. The peaks detected in both spectra at *m/z* 1498, *m/z* 1314 and *m/z* 1131 were assigned to ion fragments

generated by the loss from the molecular ion of one ($[M–(dpm)]^+$), two ($[M–2(dpm)]^+$) and three ($[M–3(dpm)]^+$) dpm ligands, respectively. The experimental isotopic distribution of the $[(M–(dpm)]^+$ fragment in the spectrum of the evaporated film (inset of the evaporated sample, **Figure 3.19**) was in complete agreement with the theoretical isotopic distribution expected for this fragment (inset of the drop cast sample, **Figure 3.19**). In addition, the intense peak at *m/z* 1079 was assigned to the ion fragment $[M–Fe–2(dpm)–L)]^+$ (L = $Ph–C(CH_2O)_3$), and the peaks at *m/z* 1101 and *m/z* 1151 were attributable to the $[M-3(dpm)–2(CH_3)]^+$ and $[M–2(dpm)–L+O]^+$ ion fragments, respectively. The low mass region (*m/z* 100-1000) of the positive ion ToF-SIMS spectra of Fe_4Ph film and of Fe_4Ph drop-cast on Au showed the most intense peaks detected at *m/z* 422 and *m/z* 733 and assigned to the $[Fe + 2(dpm)]^+$ and $[3Fe + 3(dpm) + O]^+$ ion fragments, respectively.

The chemical integrity is however not a sufficient condition to retain the SMM behavior and therefore a full magnetic characterization has been performed on the evaporated film, as shown hereafter.

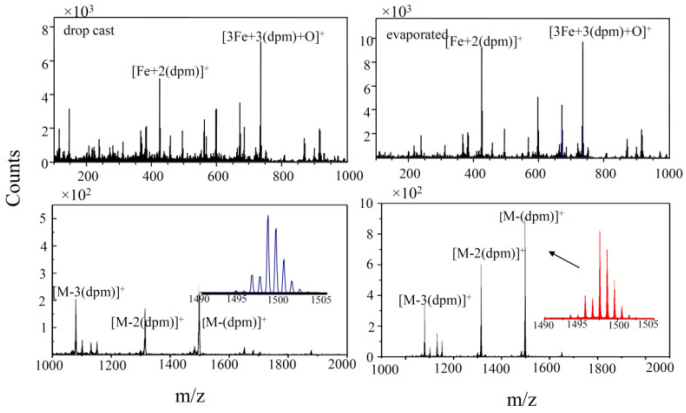

Figure 3.19: Positive ToF-SIMS spectra of Fe_4Ph film deposited by evaporation on Al and of Fe_4Ph powder drop-cast on Au from a toluene solution. The insets show the isotopic pattern detected for the $[M–dpm]^+$ positive ion peak (in the evaporated film figure) and the theoretical isotopic pattern for the $[M–dpm]^+$ molecular positive ion peak (in the drop cast figure).

Magnetic properties. The ac susceptibility of an evaporated thick film (ca. 2.7μm) of Fe_4Ph on a LiF substrate (whose area was ca. 0.5 ×0.5 cm^2) was carried out in the frequencies range of 10-1000Hz and applying a magnetic field of 2 kOe (**Figure 3.20**). Unlike Fe_4Me and Fe_4NH_2 evaporated film, in this case we observed that decreasing the temperature the imaginary component of the

susceptibility increase at the highest frequencies. However, due to the large diamagnetic contribution of the LiF substrate respect to the presence of the evaporated Fe_4Ph, the signal was very noisy and we need a more accurate investigation to clarify if the SMM behaviour is retained.

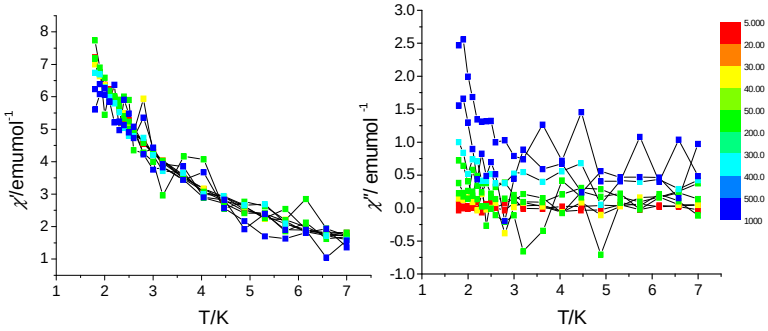

Figure 3.20: Temperature dependence of the real and imaginary components of the ac susceptibility measured for evaporated Fe_4Ph in 2 kOe applied field in the frequency range from 10 Hz to 10000 Hz (see color scale).

In order to improve the detected signal we repeated the evaporation of a Fe_4Ph thick film (ca.3μm) using a big (2×2 cm^2) and thin kapton foil as diamagnetic substrate reducing the diamagnetic contribution and increasing the deposition surface of the substrate. Moreover the use of the VSM magnetometer allowed us to work in a higher frequencies range (500-25000 Hz). In this way we obtained a good result and above all we revealed the typical behavior of SMMs as demonstrate by the presence of a frequency dependent maximum for both the real (χ',in phase) and imaginary (χ'', out of phase) components of the susceptibility at low temperature (T< 5 K) (**Figure 3.21**).

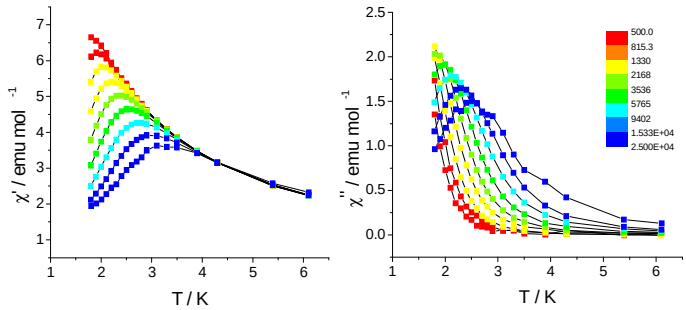

Figure 3.21: Temperature dependence of the real and imaginary components of the ac susceptibility measured for evaporated Fe_4Ph in zero static field in the frequency range from 500 Hz to 25 kHz (see color scale).

These data suggested to deepen the magnetic investigation. Isothermal magnetization curves were recorded at 1.8, 2.5 and 4.5 K as a function of the applied field (**Figure 3.22**). The non coincidence of isothermal magnetization curves for the three different temperatures once plotted vs. the *H/T* ratio was a clear signature of the presence of a relevant Zero Field Splitting (ZFS) - and thus of magnetic anisotropy - of the ground-state multiplet, as described in the first chapter for the original cluster. The solid curves calculated using the best fit parameters (D = – 0.344(11) cm^{-1} and g = 2.051(8)) were in good agreement with the experimental data of the evaporated film and with those obtained on the powder. Moreover, the saturation value of the molar magnetization was close to $M_m = 10N_a\mu_B$ corresponding to the expected value for a system with an S = 5 ground state.

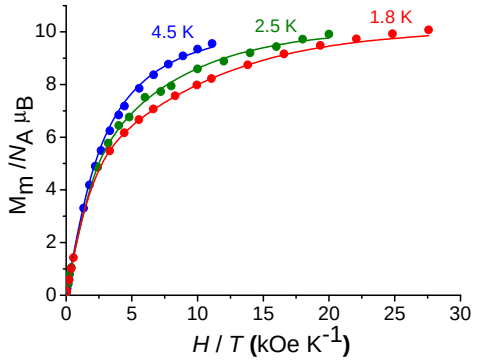

Figure 3.22: Molar magnetization curves recorded at three different temperatures of the evaporated Fe_4Ph thick film on kapton foil. The best fits calculated data are represented as solid lines.

A quantitative estimation of the magnetic anisotropy using the Spin Hamiltonian reported in the first Chapter (eq 1.2) provided an axial anisotropy parameter $D = –0.34\ cm^{–1}$, a value slightly smaller than in the pristine crystals ($D = – 0.42\ cm^{–1}$). However the accuracy of the determination could be significantly affected by the strong diamagnetic contribution of the kapton substrate, only roughly corrected during the data reduction. This hypothesis was confirmed by a more accurate insight on the magnetic anisotropy of the evaporated compound gained by High Field EPR spectroscopy, which demonstrated to be a very powerful tool to investigate highly anisotropic high-spin molecules.

The analysis of the spectra is relatively simple in the strong field limit, i.e. when the resonance field is much larger than the ZFS, and the sign of the corresponding anisotropy is experimentally determined from the temperature

dependence of band intensities. In **Figure 3.23** we report the W-Band EPR spectrum (95 GHz), recorded at 5 K and 10 K. As expected on lowering temperature the intensity moves toward the extremes of the spectrum. In fact comparing the 10 K spectra with those recorded at 5 K, we can observe the typical temperature dependence of band intensities found in high-spin systems with a negative D value. The spectra of the two samples, bulk and evaporated Fe_4Ph, were almost super imposable, with identical separations in the multilines features and intensity patterns typical of a $S = 5$ with negative ZFS. This indicates that the deposition occurs by maintaining the fine structure of the ground-state multiplet, which is responsible for the low temperature SMM behavior. A signal centered at g=2.00 observed in the film was attributed to the presence of an Fe^{3+} impurity, probably the very volatile $Fe(dpm)_3$ complex revealed also by the ToF-SIMS analysis of the evaporated SMM that decomposed during the thermal evaporation.

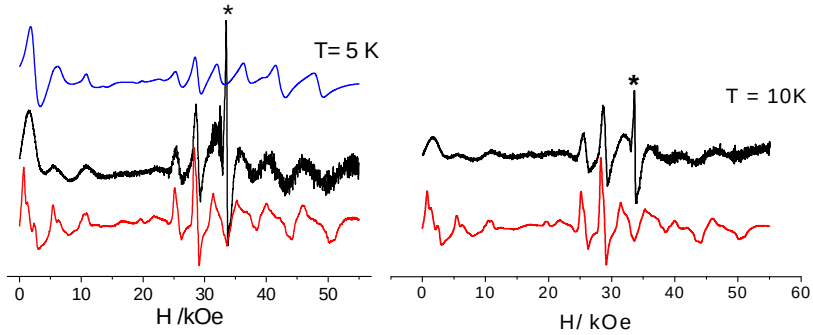

Figure 3.23: HF-EPR spectra (95 GHz) at 5 K and 10K for bulk (red line) and Fe_4Ph evaporated film (black line) samples, along with best-fit simulations (blu line). The asterisk marks the g = 2.00 transition attributed to an Fe^{3+} impurity in the film. Y-axis is in arbitrary units.

A further point to be noted is that the spectra of bulk samples show a splitting of the lines in the parallel region, a feature already reported for this cluster in the **Chapter 1** and attributed to the existence of two non-equivalent molecules with slightly different axial anisotropy. The absence of this splitting in the spectra of evaporated samples suggests that a slight modification of the crystalline environment of the cluster occurs as a consequence of the deposition process, possibly resulting in a distribution of axial anisotropies for the deposited clusters. The spectrum of the evaporated phase was then successfully simulated on the basis of the Hamiltonian:

$$\hat{\mathcal{H}}_{\mathrm{EPR}} = \mu_B \hat{\mathbf{S}} \cdot \mathbf{g} \cdot \hat{\mathbf{H}} + D\hat{S}_z^2 + B_4^0 \hat{\mathbf{O}}_4^0 + \frac{E}{2}\left(\hat{\mathbf{S}}_+^2 + \hat{\mathbf{S}}_-^2\right)$$

where $\hat{\mathbf{O}}_4^0 = 35\hat{S}_z^4 - [30S(S+1)-25]\hat{S}_z^2 + 3S^2(S+1)^2 - 6S(S+1)$ and using the following parameters: $g_{x,y} = 1.995 \pm 0.003$, $g_z = 2.005 \pm 0.003$, $D = -0.421 \pm 0.002$ cm^{-1}, $E = 0.021 \pm 0.004$ cm^{-1}, $B_4^0 = 9 \pm 2 \times 10^{-6}$ cm^{-1} with linewidth of 400 Oe. Notably these values coincide with those reported for one of the species occurring in the bulk. The distribution in the values of D and E was accounted for by parameters $\sigma_D = 0.012$ cm^{-1} and $\sigma_E = 0.036$ cm^{-1}. The absence in the simulated spectrum of the $g = 2.00$ feature confirms the assignment of this transition to an impurity.

To better understand the nature of the impurity detected by EPR, we analyzed the residual powder remained in the crucible after the evaporation process. From the EPR spectra recorded at 10 and 20 K shown in **Figure 3.24** we observed the disappearance of the g = 2 transition attributed to the paramagnetic impurities. This data, associated with the presence of a pressure peak at 220° C showed in the **Figure 3.17** leads us to suppose that the impurity is formed during the first stage of evaporation and can be easily removed by discarding the first portion of the evaporated compound. This hypothesis will be confirmed in the next chapter by XMCD spectra. It is also interesting to note that contrary to the amorphous evaporated film, the residual powder, despite that has been heated to a high temperature, still maintains the crystal feature as demonstrated by the splitting of the lines in the parallel region.

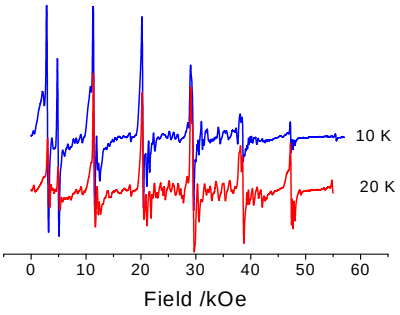

Figure 3.24: HF-EPR spectra (95 GHz) at 20 K (red line) and 10 K (blue line) of the powder remains after the evaporation process of Fe_4Ph SMM.

According to field dependent magnetization and EPR results, the clusters in the film maintain a $S = 5$ ground state, with an Ising-type anisotropy virtually unmodified as compared with the bulk, suggesting the persistence of SMM behavior as well. This results were in good agreement with the ac susceptibility

reported above. Moreover in the framework of the Debye model at each temperature a maximum in χ'' was observed when the relaxation time (τ) corresponds to $(2\pi\upsilon)^{-1}$, where υ is the frequency of the oscillating field. We could then extract from the χ'' vs υ curves the temperature dependence of the relaxation time (**Figure 3.25**). The linearity of the plot of $ln(\tau)$ vs $1/T$ indicated a thermally activated relaxation process, which was then fitted using an Arrhenius law, $\tau = \tau_0 \cdot exp(U_{eff} / k_B T)$, giving as best fit parameters $\tau_0 = 7.6 \cdot 10^{-9}$s and $U_{eff} = 12.2$ K. Both values were significantly smaller than those observed for bulk samples. For the pre-exponential factor τ_0 this may be attributed to a significant variation of the spin-phonon coupling occurring after the deposition process. On the other hand it would be tempting to attribute the observed U_{eff} to a reduced $|D|$ value, but this can be ruled out by the EPR spectra shown above. An alternative explanation is the occurrence in the deposited material of more significant distortions from the ideal trigonal symmetry of the cluster, yielding a stronger transverse anisotropy and a more efficient tunneling of the magnetization, even if these are not evident in the EPR spectra.

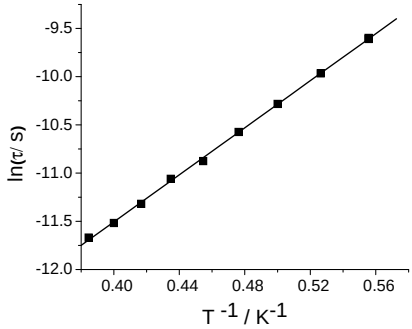

Figure 3.25: Temperature dependence of the relaxation time of the evaporated Fe_4Ph thick film. The line represents the best-fit using Arrhenius law with parameters reported in the text.

The analysis of the Argand plot (**Figure 3.26**) provides information on the width of the distribution of the relaxation times, by introducing in the Debye model a parameter α, which takes into account deviations from the ideal semicircle centered on the χ' axis. The best fit of experimental data at different temperatures provided the following values of $\alpha = 0.21$ at 2 K, $\alpha = 0.22$ at 1.9 K and $\alpha = 0.25$ at 1.8 K, only slightly larger than in the pristine material (**Figure 1.11**). The ac susceptibility confirmed therefore that Fe_4Ph retains its SMM character in films grown by thermal deposition. Moreover the Argand plot allowed us to quantify the fraction of fast relaxing paramagnetic impurity in the sample. By comparing the ratio between the two intercepts on the χ' axis of the

χ" semicircle with those obtained on the pristine material (**Figure 1.10**) we estimated that the molar fraction of the faster relaxing species, probably $Fe(dpm)_3$, does not exceed 6.5%.

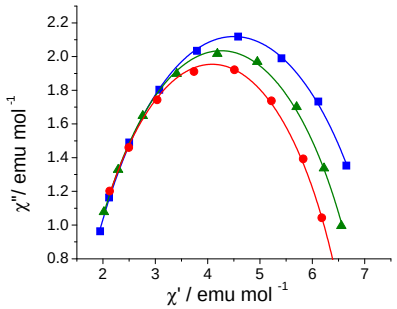

Figure 3.26: Argand plot at three temperatures, T = 1.8 K (blue squares), T = 1.9 K (green triangles) and T = 2 K (red circles), of the evaporated Fe_4Ph thick film. The lines represent the best fit curves using a modified Debye model.

AFM measurements. Once demonstrated the SMM behaviour of the evaporated film we studied *ex-situ* the evolution of the morphology of Fe_4Ph films as a function of the deposited thickness by means of AFM measurements. In fact, the low roughness would be fundamental to develop multilayered nanostructures combining magnetic or conducting layers with SMMs films in order to investigate the interplay of magnetism and transport at the molecular level. In **Figure 3.27 c** (lateral images) we show a sequence of AFM images. Operation of the AFM in contact mode was avoided in order to prevent the modification of the film morphology due to tip-surface interaction. The morphological parameters did not change significantly by acquiring images in macroscopically separated areas, whose thickness decreases increasing the distance from evaporation source. The morphology of the films resulted to be locally very uniform and flat in the whole explored range of thicknesses, showing no evidence of the formation of microcrystalline domains. On a smaller length scale the tendency to form very shallow aggregates of molecules with a lateral extension down to a 50 nm range becomes evident for the thicker film. These observations were made more quantitative by extracting the overall root mean square (RMS) roughness for each value of the deposited film thickness, and the lateral correlation length. From **Figure 3.27 c**, (central image; red squares) it is evident that the RMS roughness was always very low, increasing from about 1 nm for the 100 nm thick film (slightly above the initial roughness of the clean substrate as shown in **Figure 3.27 a**) to about 6 nm when the film thickness increases to 2700 nm. Closely correlated to the increase of the RMS roughness, also the lateral correlation

length (blue squares) appeared to grow monotonically from about 50 nm to about 125 nm. The lateral correlation length was not plotted for the thinnest film (100 nm) since it becomes comparable or lower than the nominal tip radius (20 nm). From the plot of the RMS roughness versus the film thickness, an approximately linear trend can be inferred. These observations, in particular the very low value of the RMS roughness, indicate that the evaporated molecules after reaching the surface have a significant mobility, and can relax diffusively towards highly coordinated sites. This observation is an indirect confirmation of the relatively weak interaction between Fe_4Ph molecules (which is also responsible for the low sublimation temperature of the compound).

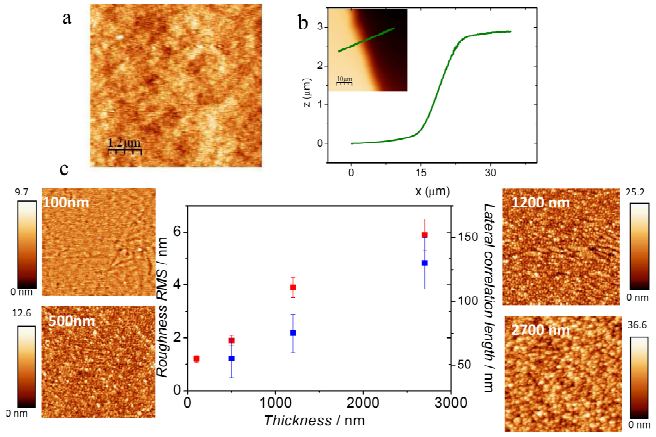

Figure 3.27: (a) AFM image of the initial subtract prior to film deposition. The roughness of the clean substrate was equal to 0.2 nm. (b) Line profile of a AFM topography, showing a Fe_4Ph film thickness of about 2.7 µm. In the inset the AFM 50×50 μm^2 image describes the scratch that allowed us to estimate the actual thickness of the film and to calibrate the microbalance signal. (c) AFM 6×6 μm^2 images showing the evolution of the morphology as a function of the thickness. The lateral bars represent the vertical dynamic range. The central figure provides the evolution of the RMS roughness (red squares) and of the lateral correlation length (blue squares) as a function of Fe_4Ph film thickness.

3.3.6. Thermal deposition of Fe_4SMe SMM

Thermal evaporation parameters. In the **Figure 3.28** is shown the pressure and the deposited thickness profile as function of the temperature of

$Fe_4(dpm)_6(CH_3SCH_2\text{-}C(CH_2OH)_3)_2$, Fe_4SMe compound recorded during the evaporation procedure. We can observe many similarities with that obtained for Fe_4Ph. In fact also in this case we detected two main peaks of pressure at 200 °C and at 280°C but only close to the last one the QCM was able to reveal a material deposition. Furthermore, just as for the evaporation of Fe_4Ph compound, we obtained a orange residue after the thermal evaporation.

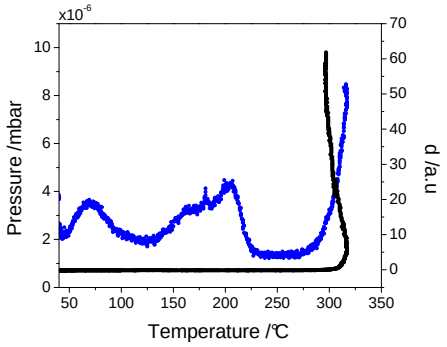

Figure 3.28: Pressure (blue line) and thickness (black line) trend as function of the temperature recorded during Fe_4SMe thermal evaporation.

ToF-SIMS. As for the other evaporated samples we studied the chemical composition of the evaporated film on Al foil by ToF-SIMS analysis. The results are shown in **Figure 3.29** and **Figure 3.30**. Comparing the spectra of the powder drop cast on a Si substrate from a toluene solution with those obtained for the evaporated film, we observed the same fragmentation pattern although the signals in the evaporated sample were less intense than in the drop cast. In particular in the high mass region of the negative ion spectra we revealed the presence of the peak at *m/z* 1648 attributed to the molecular ion.

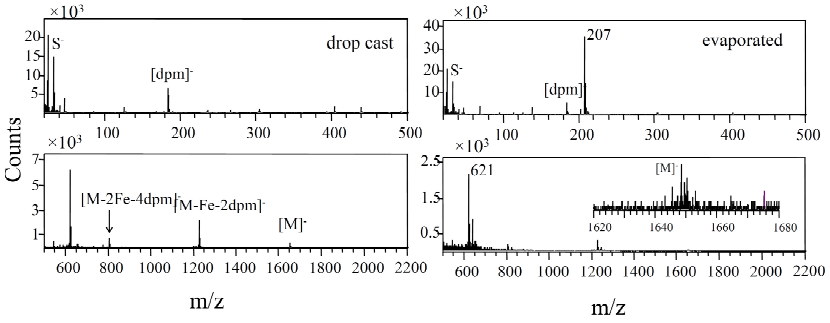

Figure 3.29: Negative ToF-SIMS spectra of Fe_4SMe film deposited by evaporation on Al and of Fe_4SMe powder drop-cast on Si from a toluene solution. The insets show zoom of a very weak peak assigned to the molecular ion.

This trend was confirmed by the positive ion spectra (**Figure 3.30**) in which we detected in both spectra the peaks at *m/z* 1465, 1282, and 1099 assigned to the fragments generated by the loss from the molecular ion of one dpm ($[M–(dpm)]^+$), two dpm ($[M–2(dpm)]^+$), and three dpm ($[M–3(dpm)]^+$). This distribution was found also for Fe_4Ph evaporated film.

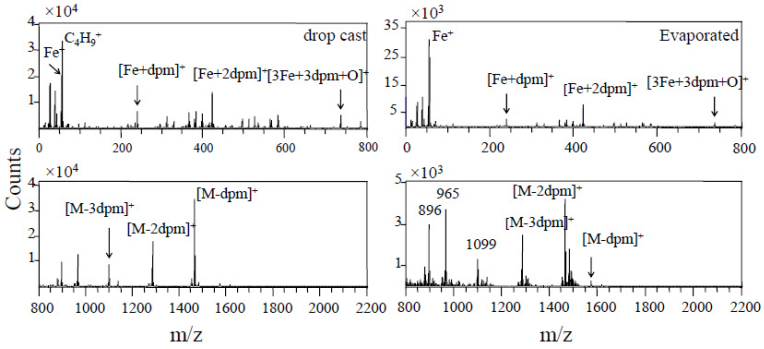

Figure 3.30: Positive ToF-SIMS spectra of Fe_4SMe film deposited by evaporation on Al and of Fe_4SMe powder drop-cast on Si from a toluene solution.

Magnetic properties. As we observed for others evaporated compounds the ToF-SIMS analysis and the detection of the molecular ion peak in the negative spectrum is not enough to confirm the success of the evaporation. Also in this case it was necessary to investigate the magnetic properties of the film evaporated on Kapton foil. The frequency and temperature dependencies of the zero field ac susceptibility of Fe_4SMe film at low temperature indicated the presence of a maximum for the real component of the susceptibility (χ', in phase) but not for the imaginary (χ'', out of phase) components of the susceptibility. Applying a magnetic field of 1 kOe the frequency dependence of both real and imaginary components was increased evidencing the frequency dependent maxima also in the imaginary component, thus allowing us to extract the parameters characterizing the SMM behavior (**Figure 3.31**).

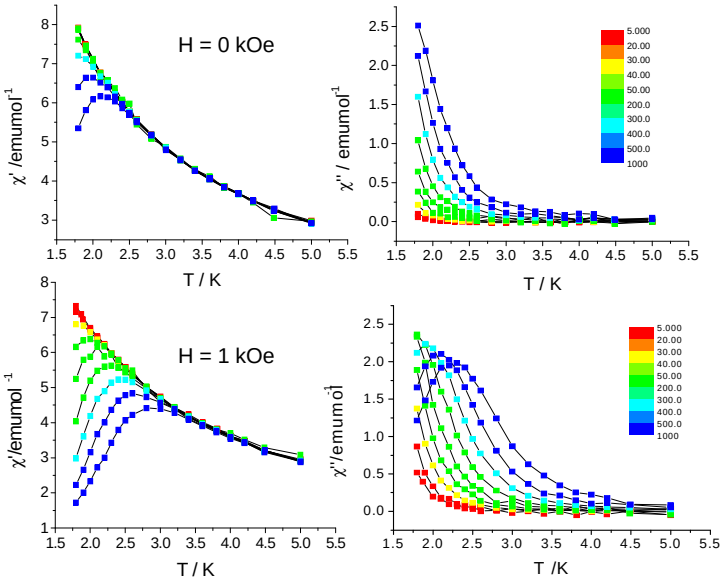

Figure 3.31: Temperature dependence of the real and imaginary components of the ac susceptibility measured for evaporated Fe_4SMe in zero field (upper part) and 1 kOe field (bottom part) in the frequency range from 10 Hz to 10000 Hz (see color scale).

The Arrhenius plot reported in **Figure 3.32** shows that the relaxation time increases on decreasing the temperature. The parameters U_{eff} and τ_0 were evaluated by the linear fit and gave as best fit values U_{eff} = 15.75 K and τ_0 = 1.61×10^{-8} s. Both values were in agreement with those obtained for the bulk material that showed an energy barrier U_{eff} = 14.13 K and a τ_0 = 4.36×10^{-8} s.

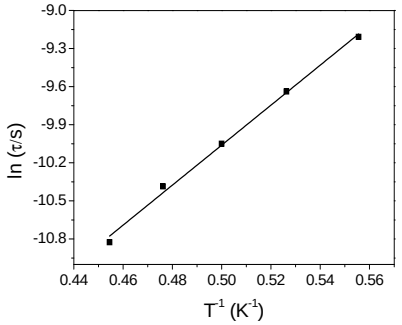

Figure 3.32: temperature dependence of the relaxation time of the evaporated Fe_4SMe thick film. The line represents the best-fit using Arrhenius law with parameters reported in the text.

The saturation value of isothermal magnetization curves (**Figure 3.33**) confirmed the expected spin ground state (S = 5) for the evaporated Fe_4SMe. Moreover the non coincidence of the curves recorded at the three different temperatures supported the presence of a relevant ZFS of the ground-state multiplet, as in the original cluster.

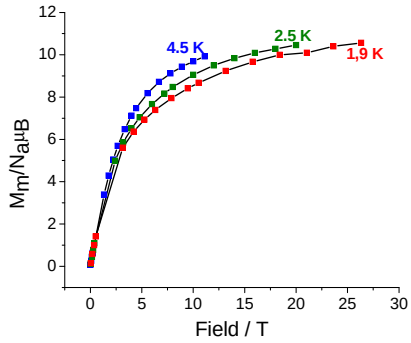

Figure 3.33: Molar magnetization curves of the evaporated Fe_4SMe thick film at three different temperatures.

HF-EPR spectra carried out on the evaporated thick film at 95 GHz and 20 K are reported in **Figure 3.34**. Also these data confirmed the typical behavior of an $S = 5$ state with easy-axis type anisotropy ($D < 0$) as demonstrate by the presence of five parallel and five perpendicular transitions detected for magnetic fields lower and higher than that corresponding to $g = 2.0$ signal (marked in the figure with an asterisk) attributed at the same paramagnetic impurities of Fe^{3+} revealed in Fe_4Ph compound.

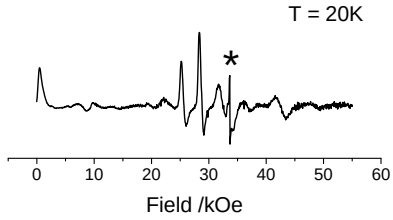

Figure 3.34: HF-EPR spectra (95 GHz) at 20 K of the thermal evaporated Fe_4SMe thick film.

At this point we query what is the factor that allows to Fe_4Ph and Fe_4SMe to remain intact during the evaporation unlike the other compounds. The only difference that we observed during the evaporation is the presence of a pressure peak of some volatile component that cannot be detect by the QCM at ca. 220°C. On the other hand these compounds were the unique to contain solvent molecules

in the crystal structure, one Et_2O molecule in Fe_4Ph and half molecule of Et_2O in Fe_4SMe. For this reason we supposed that this factor makes these two compounds more suited to be evaporated than the other clusters. The peak of pressure detect at 220°C could be due to the evaporation of the solvent from the crystals.

In order to clarify this point, thanks the collaboration with Prof. Cornia, from the University of Modena, we tried to evaporate Fe_4SMe specially synthesized without molecule of solvent in the crystal structure.

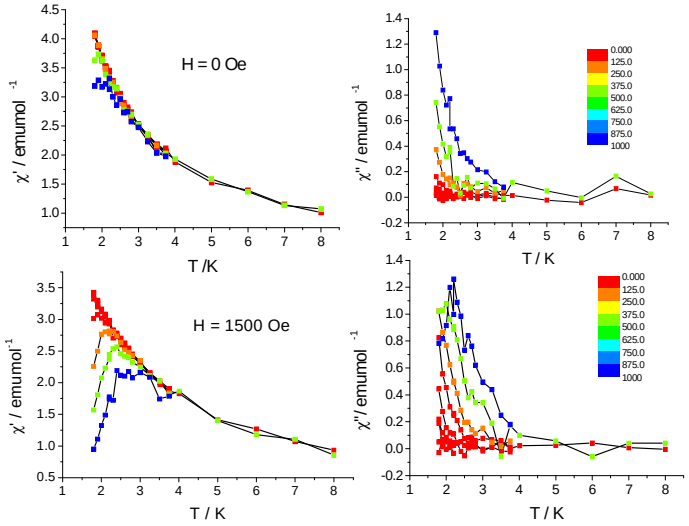

Figure 3.35: Temperature dependence of the real and imaginary components of the ac susceptibility measured for evaporated Fe_4SMe in zero field (upper part) and 1.5 kOe field (bottom part) in the frequency range from 10 Hz to 10000 Hz (see color scale).

Fe_4SMe without solvent in the structures crystallized in the monoclic system. The evaporation behavior and parameters seemed to be the same of the correspondent solvated molecule. Moreover the ac susceptibility measured in an applied field of 1.5 kOe confirmed the SMM behavior of the deposited film although the signal is noisy, maybe due to a lower thickness of the film (ca.1.5 μm instead of 3μm), see **Figure 3.35**.Unfortunately also the EPR (**Figure 3.36**)spectra carried out at 10 and 20 K is very noisy and we can only reveal the transitions in the parallel region and the peak centered at g = 2 attributed, also in this case, to the presence of a paramagnetic contribution.

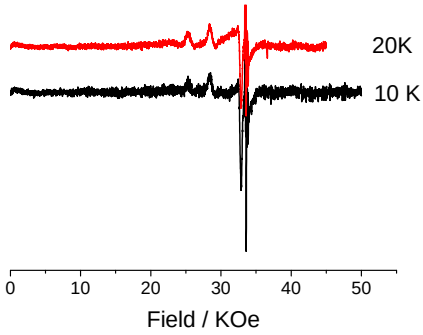

Figure 3.36: HF-EPR spectra (95 GHz) at 20 K (red line) and at 10 K (black line) of the thermal evaporated film.

These experiments demonstrated that the chemical and magnetic integrity of the evaporated film did not depend by the presence of the solvent in the crystal structure although these data should be further confirmed by increasing the thickness of the film. However we think that a particular packing of the molecules in the crystal plays a key role in the feasibility of the deposition by thermal UHV evaporation.

3.4. Conclusions

In this Chapter we have described the deposition of a Fe_4 SMMs family. We have proved that it is possible for two of them, Fe_4Ph and Fe_4SMe, to deposit a thick film on different substrates using the thermal deposition technique in UHV conditions without inducing changes in the chemical structure and in the magnetic properties. Furthermore, thermal deposition allows growing films characterized by low roughness and uniform morphology and with controlled thickness. These are fundamental characteristics to develop multilayered nanostructures combining magnetic or conducting layers with SMMs films. This finding opens interesting perspectives for the deposition of Fe_4 cluster monolayers so as to promote a stronger or more specific interaction with the substrate. In the next chapter we will describe the magnetic properties of a monolayer deposited on two different substrates.

Chapter 4.

X- Ray magnetic studies of SMMs on surface

4.1. Introduction

The Self-Assembly of Monolayer (SAM) technique has been employed to assemble arrays of SMMs since 2003[50] while the attempts of using thermal evaporation to grow SMM films has been introduced only recently with this thesis work.[83] However the most difficult aspect related to the organization of SMMs, that hampered a larger activity of research, is related to the impossibility of using standard techniques to study the magnetism of monolayers of magnetic molecules. In fact, notwithstanding the great advances in sensitivity of SQUID detection, standard magnetometry is incapable of picking up the signal of such a small ensemble of molecules; the picture is worsened by the fact that, at such degree of dilution, the diamagnetic contribution of the substrate, as well as paramagnetic signals from impurities become preponderant. A good candidate for this kind of studies would be EPR: if not able to give direct information on magnetization dynamics in fact, EPR spectroscopy is in principle both an excellent technique to gain information on the spin structure of magnetic complexes and an extremely sensitive spin probe. Unfortunately, one of the key features of single molecule magnets is the large spin ground state (for instance Fe_4 complexes $S = 5$), which is associated with a large magnetic anisotropy that spreads the resonances over a wide field range. This reduces the sensitivity of the technique, which is expressed in number of spins per unit of field. Moreover the large anisotropy requires, for a full characterization, the use of unconventional high-field/high-frequency EPR, so this type of measurement is very challenging and very sensitive to paramagnetic impurities, which are likely to give rise to huge sharp signals with respect to the signal from Fe_4. As mentioned in the **Chapter 2** another possible approach is the use of scanning probe microscopies,[53] that can be used to extract information on the magnetic

properties of the scanned surface.[84] Among the "*magnetism-oriented*" techniques, MFM (Magnetic Force Microscopy),[54] SP-STM (Spin Polarized STM), SHPM (Scanning Hall Probe Microscopy) and ESN-STM (Electron Spin Noise STM) have been suggested to be used for the detection of the magnetism of magnetic molecules. In particular the SP-STM technique is the top candidates for the study of SMMs grafted to surface, since in principle it allows to probe with a spin polarized current the transport properties of a single molecule, that are expected to be directly related to their magnetism. However no conclusive results have been presented up to now using this "*local*" approach. On the other hand, successful results in characterizing magnetism have been already obtained by using a spectroscopic approach based on dichroism (Magnetic Circular Dichroism, MCD and X-ray Magnetic Circular Dichroism, XMCD). In particular XMCD is an element and surface selective technique with an extreme sensitivity that carried out under extreme conditions of strong magnetic field and cryogenic temperatures can be used to demonstrate the conservation of SMM properties at the nanoscale.

In the following paragraphs we will provide a detailed description of this synchrotron based technique. We will show how it can be used to magnetic ultrathin layers and its application to molecular magnetism by summarizing the results obtained in the investigation of the magnetic properties of Mn_{12}, Fe_4 and $TbPc_2$ SMMs monolayers.

4.2. How do synchrotrons work?

Synchrotron radiation is electromagnetic radiation generated by charged particles, usually electrons, whose trajectory is deviated by magnetic fields and forced to move along a curved path. The bending of the particles trajectory causes the emission of an electromagnetic radiation, and generally the peak of the emission is in the wavelengths of X-rays. Electrons are generated by an electron gun and then accelerated up to very high speeds through a series of accelerators: the linear accelerator used to speed up the electrons to hundreds of MeV, the booster ring and the storage ring. When the electrons enter into the booster ring their trajectories are curved by dipole magnets (bending magnet) and a radio frequencies source is used to accelerate the electrons in the straight sections of the ring. Here they reach an energy of several GeV before they are transferred into the storage ring. This consists of a series of straight sections (accelerating the beam) and curved one (constituted by bending magnets, and insertion devices) together to form a circle (**Figure 4.1**). From those curved sections origin the

beam-lines that use the electromagnetic radiation produced by bending the electrons trajectory.

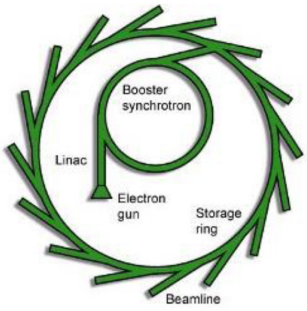

Figure 4.1: Schematic view of the Synchrotron structure

The bending magnets are dipole magnets that produce a very stable beam over a broad spectrum including infrared; while the insertion devices (**Figure 4.2**) are arrays of magnets capable to produce more intense, tuneable light. Insertion devices come in two main types: wigglers and undulators.

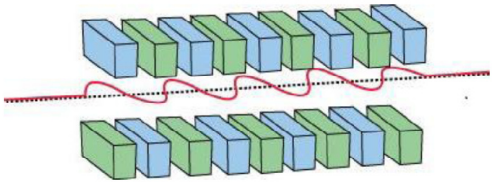

Figure 4.2: Insertion device scheme that consist of magnet arrays which cause the electron beam to follow a wiggling or undulating path

A wiggler consists of an array of magnets which cause the electron beam to follow a "*wiggling*" path. This causes the light to be produced in a wide cone, spanning a broad spectrum of X-rays. Wigglers are used in beamlines where the priority is for very high energy X-rays. An undulator, produces very bright light in a very narrow beam over a continuous energy range. By varying the relative orientation of the upper and lower magnet arrays, it is possible to tune the photon polarization from linear to circular.

4.3. X-Ray Absorption spectroscopy and related techniques

X-Ray absorption spectroscopy (XAS) can be used to obtain information about the elemental composition of the sample and on the chemical environment of a specific element and their magnetic state by exploiting the energy dependent absorption of X-rays. Core electrons are excited in the absorption process into empty states above the Fermi energy and thereby used to probe the electronic and magnetic properties of the empty valence levels. The absorption process is usually detected by monitoring the current flowing to re-establish neutrality of the sample after that secondary electrons are emitted through the Auger process induced by the X-ray. This total electron yield (TEY) detection mode is sensitive to the first few nanometers, corresponding to the escape depth of secondary electrons.[85] This unique surface sensitivity makes XAS and related techniques a key tool for the investigation of thin films.

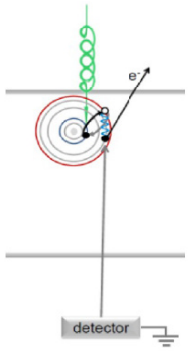

Figure 4.3: Simple scheme of total electron yield detection mode.

In the following we report as an example the spectra of the magnetic *3d* transition Fe metal elements. The magnetic properties are largely determined by the *3d* valence electrons and since the X-ray absorption process is governed by dipole selection rules, the *d*-shell properties are best probed by *L*-edge absorption studies (*2p* to *3d* transitions) (**Figure 4.4**).

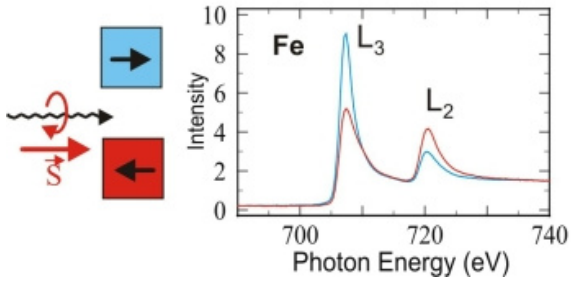

Figure 4.4: *L*-edge X-ray absorption edge spectra of Fe in the form of the elemental metals. They two main structures are called the L_3 and L_2 absorption edges.[86]

The two main peaks in the spectra arise from the spin orbit interaction of the 2*p* core shell and the total intensity of the peaks is proportional to the number of empty 3*d* valence states. In some case the spectra exhibit a multiplet structure due to the spin and orbital momentum coupling of different 3*d* valence holes (or electrons) in the electronic ground state, and from coupled states formed after X-ray absorption between the 3*d* valence holes and the 2*p* core hole.

The concepts of XMCD spectroscopy, pioneered by Gisela Schütz et al. in 1987, are illustrated in **Figure 4.5**. [87]For a magnetic material the *d* shell has a spin moment which is given by the imbalance of spin-up and spin-down electrons or equivalently (except for the sign) by the imbalance of spin-up and spin-down holes. In order to measure the difference in the number of *d* holes with up and down spin, we need to make the X-ray absorption process spin dependent. This is done by use of right or left circularly polarized photons which transfer their angular momentum to the excited photoelectron. The photoelectron carries the transferred angular momentum as a spin or an angular momentum, or both.[88-89] If the photoelectron originates from a spin-orbit split level, e.g. the $p_{3/2}$ level (L_3 edge), the angular momentum of the photon can be transferred in part to the spin through the spin-orbit coupling. Right circular photons transfer the opposite momentum to the electron as left circular photons, and hence photoelectrons with opposite spins are created in the two cases. Since the $p_{3/2}$ (L_3) and $p_{1/2}$ (L_2) levels have opposite spin-orbit coupling (*l*+*s* and *l*-*s* respectively), the spin polarization will be opposite at the two edges. In the absorption process, “spin-up” and “spin-down” are defined relative to the photon helicity or photon spin, which is parallel (right) or antiparallel (left) to the X-Ray propagation direction.

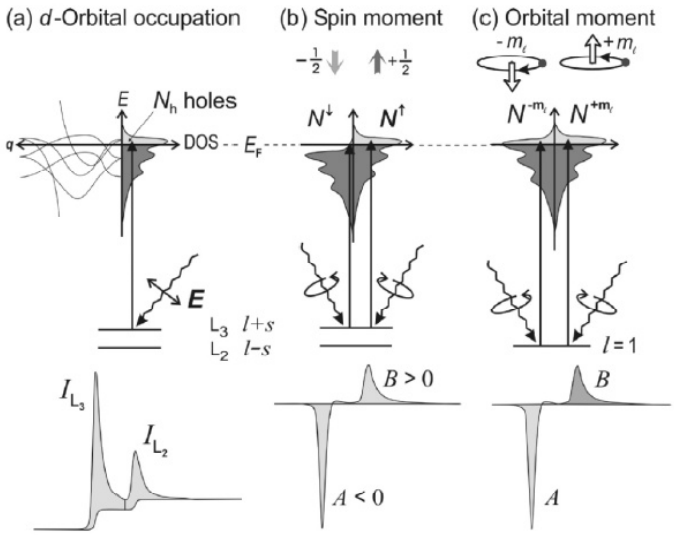

Figure 4.5: Electronic transitions in conventional L-edge x-ray absorption (a), and X-ray magnetic circular X-ray dichroism (b,c), illustrated in a one-electron model. The transitions occur from the spin-orbit split *2p* core shell to empty conduction band states. By use of circularly polarized x-rays the spin moment (b) and orbital moment (c) can be extracted exploiting the sum rules from linear combinations of the integrals of dichroic signals A and B.

Since spin flips are forbidden in electric dipole transitions, spin-up (spin-down) photoelectrons from the *p* core shell can only be excited into spin-up (spin-down) *d* hole states. Hence the spin-split valence shell acts as a detector for the spin of the excited photoelectron and the transition intensity is simply proportional to the number of empty *d* states of a given spin. The quantization axis of the valence shell "*detector*" is given by the magnetization direction which for a maximum dichroism effect needs to be aligned with the photon spin direction. The size of the dichroism effect scales like $cos\theta$, where θ is the angle between the photon spin and the magnetization direction. Hence the maximum of the dichroic effect is observed if the photon spin direction and the magnetization directions are parallel or anti-parallel as shown on the left side of **Figure 4.4**. When the photon spin and the magnetization directions are perpendicular the resonance intensities at the L_3 and L_2 edges lie between those obtained for parallel and anti-parallel alignments. In **Figure 4.5 b** is represented the XMCD intensity as A (L_3 -Edge) and B (L_2 Edge). Note that A and B have opposite sign reflecting the opposite spin-orbit coupling of the $p_{3/2}$ and $p_{1/2}$ levels. If the *d* valence shell possesses an orbital moment, as shown in **Figure 4.5 c**, it will act like an orbital

momentum detector. The orbital moment sum rule links the orbital moment in the *d* shell to the dichroism intensity.[89] In fact by summing the L_3 (l+s) and L_2 (l-s) intensities the contribution due to the spin *s* is eliminated and then the orbital moment of the valence shell is measured.

Finally we briefly mention the X-ray natural linear dichroism technique, XNLD, that we have used in this thesis work to describe the angle dependent effects of the sample respect the vertical and horizontal polarized light. In non magnetic samples the dichroism is due only to an anisotropic charge distribution and empty state distribution caused by bonding. Hence the transition intensity is directly proportional to the number of empty states in the direction of the electronic field vector. In this thesis work we have used the XNLD technique in order to reveal preferential orientation of SMM deposit on surface. In fact by fixing the X-ray linearly polarization light and rotating the sample it is possible to investigate by the shape and the intensity of the detected signal, the orientation of easy axis of magnetization of the molecules respect the surface. This kind of technique can be applied also on magnetic samples where an additional geometrical anisotropy may be induced when applying a magnetic field (in this case we speak of X-Ray Magnetic Linear Dichroism, XMLD). For example by fixing the X-ray polarization vector along the easy axis and rotating the magnetization from the easy to the hard axis applying a magnetic field, it is possible to argue directly the magneto-crystalline anisotropy of the sample.

4.4. XAS and XMCD studies of Single Molecule Magnets

As underlined in the previous paragraph the XMCD method is able to probe the electronic and magnetic structure of the SMMs. XAS spectra can be used to ascertain the electronic structure of the metal centers, while XMCD spectra can reveal the coupling between spins in the system. The use of XMCD in molecular nanomagnets characterization started, before the beginning of this thesis work, with the investigation of the archetypal SMM, Mn_{12}; for this reason we believe that is necessary to summarize here the results that have been obtained since 2001 studying this system in both the bulk and nanostructured phases.

4.4.1. Redox studies on Mn_{12} SMM.

In the Mn_{12} cluster the XAS characterization allows to provide direct information on the oxidation state of the transition metal ions that constitute the core of this system that include redox-active ions like Mn^{3+} and Mn^{4+}.[90] In particular in this molecule the external spins of the Mn^{3+} ions (S = 2) are aligned anti-parallel with

the internal Mn^{4+} ions (S = 3/2) producing a spin ground state value S = 10 (**Figure 4.6**).[1-2, 91]

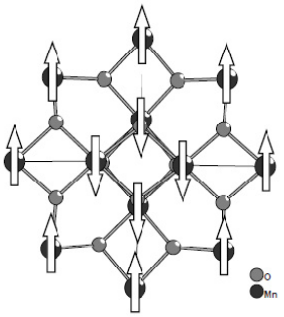

Figure 4.6: Core structure and coupling scheme in a Mn_{12} cluster.

The mixed valence composition has been confirmed by the XAS investigations performed on bulk Mn_{12}-*acetate* in which absorptions at Mn $L_{2,3}$ edge ($2p \rightarrow 3d$ transitions) were observed that correspond to the expected proportions of Mn^{3+} and Mn^{4+} ions. Similar experiments performed on bulk samples of Mn_{12} molecules functionalized with ligand containing thioacetyl ($C_{15}SAc$) and thioether group (PhSMe), included in the molecular structure in order to anchor Mn_{12} to a gold surface, yielded essentially the same results, indicating that both groups are compatible with the high oxidation state of manganese ions in Mn_{12} clusters. However, when monolayers of Mn_{12}-$C_{15}SAc$ and

Mn_{12}-PhSMe were investigated, XAS spectra clearly indicated the presence of Mn^{2+} beyond the expected Mn^{3+} and Mn^{4+} components (**Figure 4.7**). Several attempts were made to obtain intact Mn_{12} clusters on surface, by varying the ligand shell and/or the deposition procedure. Partial reduction to Mn^{2+} was invariably observed and it was impossible to obtain systems containing only Mn^{3+} and Mn^{4+}. [92]

Moreover XMCD characterization of the bulk non-functionalized and functionalized Mn_{12} systems confirmed the ferrimagnetic structure of the cluster and later evidenced more clearly the presence of a strong Mn^{2+} component in Mn_{12} derivatives assembled on gold and the modification of the expected magnetic polarization of each Mn ion.

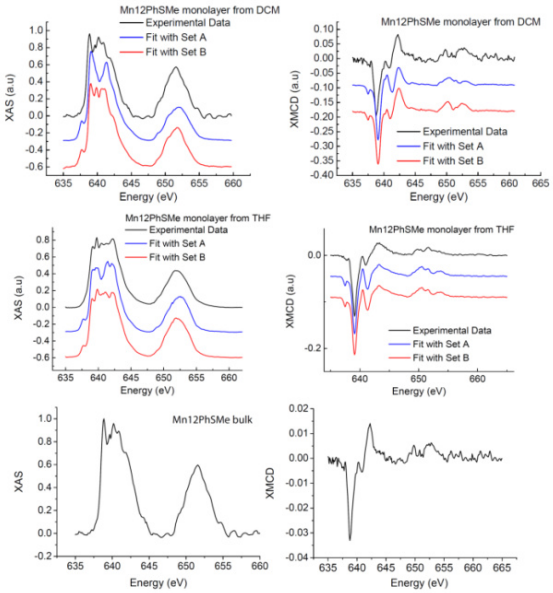

Figure 4.7: Experimental XAS and XMCD spectra of Mn_{12}PhSMe monolayer prepared from CH_2Cl_2 (top), from THF(middle) compared to the fittings using two different sets (A and B). More details relative to the fitting parameters are reported in the Pineider PhD thesis. On the bottom part XAS and XMCD spectra of bulk is reported [92,69]

Additionally, by monitoring the dependence of the XMCD as function of the magnetic field that in 3*d* metals, due to Spin-orbit coupling, is proportional to the total magnetic moment, it has been possible to monitor the dynamics of magnetization of the SMM. Surprisingly the data obtained for Mn_{12}-PhSMe bulk film, obtained by drop cast on gold surface did not reveal the opening of the magnetic hysteresis loop down to 700 mK (**Figure 4.8**).[67] The hysteresis, on the other hand is clearly visible also at higher temperatures (up to 2.5K) by performing traditional magnetometry experiments on the same sample.

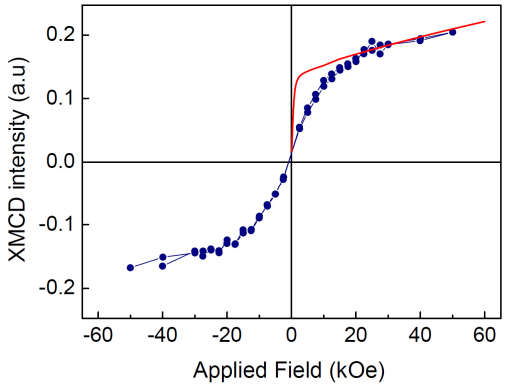

Figure 4.8: Hysteresis curves of a drop cast sample of Fe_4C_9SAc measured with XMCD in TEY detection mode at different temperatures (straight line represents the simulation).

The loss of slow relaxation of the magnetization in the topmost layers of the deposit, investigated thanks to the surface selectivity of the TEY detection mode, without a degradation of the inorganic core of Mn_{12} can be explained considering that the energy barrier originating the SMM behaviour is the result of a delicate interplay between electronic and structural parameters of the single metallic centers and their mutual interaction: the surface, even that of the material itself, is a strongly asymmetric and strained environment, and it is very reasonable to suppose that these strains are more than enough to cause distortions in the clusters that are crucial, if not to the spin coupling pattern, for the necessary axial anisotropy of the complex.

4.4.2. Spin structure of Fe_3Cr and Fe_4 SMMs.

XAS/XMCD technique has been not only used to evidence that Mn_{12} complexes are not the ideal SMM to be employed in nanostructures, but also to evidence more promising candidates. Among them the most studied one is Fe_4 system that recently has been demonstrated to retain the SMM properties at the nanoscale through an XMCD-based magnetic characterization that revealed the opening of the hysteresis loop (**Figure 4.9**).[67]

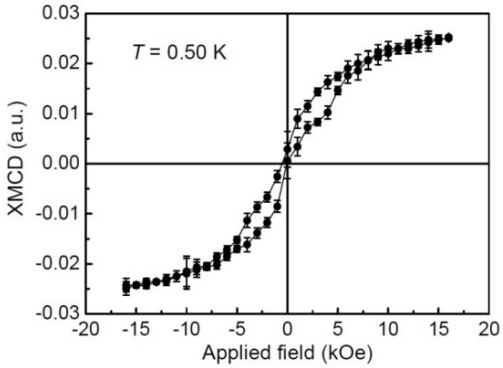

Figure 4.9: Hysteresis curves of a monolayer of Fe_4C_9SAc on gold measured with XMCD (E = 709.2 eV) in TEY detection mode at different temperatures.

To understand the features of the XMCD spectra of Fe_4 systems we compared two isostructural clusters, one belonging to the Fe_4 family and one of the Fe_3Cr family, more precisely the $[Fe_4(L)_2(dpm)_6]$ (H_3L = 11-(acetylthio)-2,2-bis(hydroxymethyl)undecan-1-ol) and the $[Fe_3Cr(L)_2(dpm)_6]$, Fe_3Cr (**Figure 4.10**). The latter compound was synthesized by Prof. Cornia from the University of Modena, by replacing the central Fe^{3+} of Fe_4 SMM with a Cr^{3+}. The central Cr^{3+} ion can then be exploited as an additional internal spectroscopic probe for combined XMCD studies at Fe-$L_{2,3}$ and Cr-$L_{2,3}$ edges.

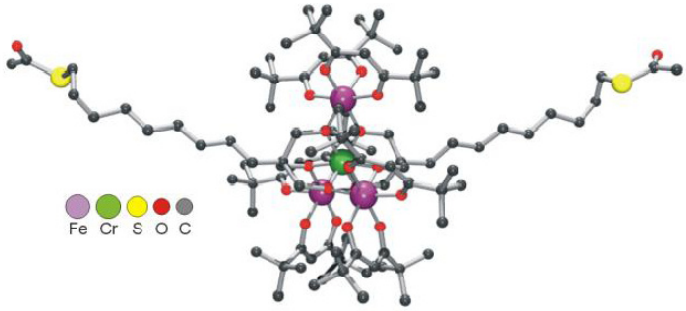

Figure 4.10: Crystal structure of Fe_4/Fe_3Cr derivatives with the tripodal functionalized with thioacetyl group to allow grafting on gold.

Monolayer deposits of Fe_3Cr and Fe_4 on Au(111) were obtained by the self assembly technique described in the second chapter. Their XAS and XMCD spectra at 7 K were similar to those recorded on the bulk phase. In both cases, the

XMCD signal reached its maximum amplitude at 709.1 eV (Fe-L_3 edge) and 577.5 eV (Cr-L_3 edge) and displayed the same fine structure as in the bulk, indicating a similar electronic structure for the monolayer and for the bulk phase (**Figure 4.11**). Moreover, whereas the features observed at Fe-$L_{2,3}$ edge were characteristic for field-polarized high-spin Fe^{3+} ions described in the **Chapter 1**, the signal at Cr-$L_{2,3}$ edge was of opposite sign than for an isolated Cr^{3+} ion. This proved that the magnetic polarization of Cr *opposes* the applied field, *i.e.* the Fe and Cr spins are antiparallel.

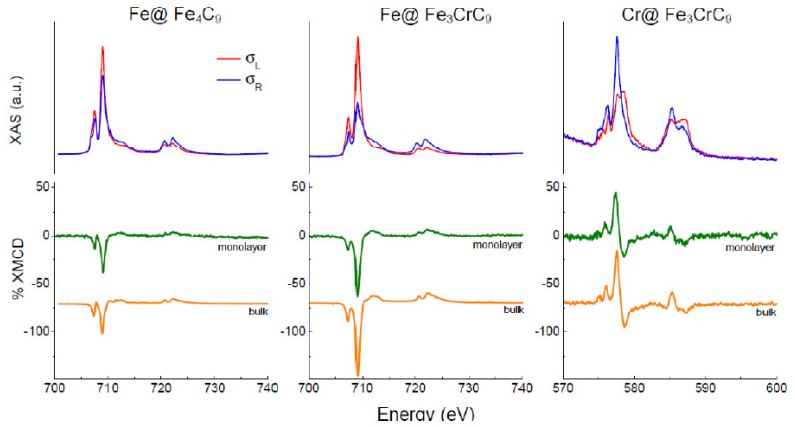

Figure 4.11 (Upper panels) Circularly polarized XAS spectra recorded on bulk samples of Fe_4C_9 at Fe-$L_{2,3}$ edge (left) and of Fe_3CrC_9 at Fe-$L_{2,3}$ (middle) and Cr-$L_{2,3}$ edges (right). (Lower panels) XMCD signals of the two compounds measured on bulk samples and monolayers on Au.[67]

Moreover, since the Fe^{3+} ions in both complexes have very similar coordination environments, a meaningful comparison can be made between the XMCD features shown by monolayers of the two compounds at the Fe-$L_{2,3}$ edge (**Figure 4.12**). At the same temperature and applied field, the amplitude of the dichroic component at 709 eV increases from 39% to 63% when replacing the central Fe^{3+} with Cr^{3+}. We checked whether such a large increase in the magnetic polarization at iron sites can be ascribed to the suppression of the opposing contribution of the central Fe^{3+} so as to provide direct proof of the ferrimagnetic ground state spin structure in Fe_4 molecule.

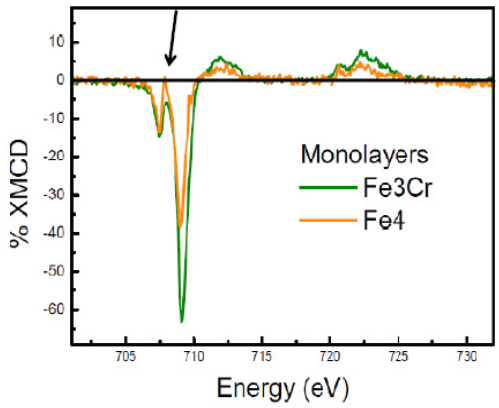

Figure 4.12: XMCD contribution at the Fe-$L_{2,3}$ edge measured on monolayers of Fe_4 and Fe_3Cr at 3T and 7 K.

Assuming the XMCD signal to be site-independent and proportional to the local magnetic moment, the normalized XMCD signal is expected to undergo an approximately twofold increase when passing from Fe_4 to Fe_3Cr complexes, as observed experimentally. Deeper inspection of the XMCD signals reveals other interesting differences. At an energy of ca. 707.9 eV (see arrow in **Figure 4.12**) the dichroic signal is negative in Fe_3Cr but close to zero in Fe_4. The former behavior is typical for octahedral high-spin FeO_6 complexes. Since the coordination geometry of the peripheral Fe ions in the two compounds is virtually identical, the feature observed in Fe_4 at 707.9 eV may reflect differences in the energy dependence of the XMCD contribution for peripheral and central Fe ions, due to their not equivalent coordination spheres. To summarize, the intensity and detailed shape of XMCD signal at Fe-$L_{2,3}$ edge provide an important fingerprint of the ferrimagnetic spin structure in Fe_4 complexes that will be employed in **Chapter 5** to investigate Fe_4 SMMs evaporated on different substrates.

4.5. Conclusions

In this chapter we evidenced the potential of the X-ray Absorption techniques for the characterization of monolayers of magnetic molecules. In fact SMMs are fragile systems that, during the deposition process can be affected by redox alteration and structural rearrangement, like in the case of Mn_{12}. Moreover we have described the most important magnetic features of Fe_4 on surface, its electronic and magnetic structure and we have observed how the intensity and the shape of the XMCD signal recorded at Fe-$L_{2,3}$ edge change by replacing the central Fe with a Cr ion providing a fingerprint of the ferrimagnetic spin structure in Fe_4 complexes.

We will use these information in the next two chapters where we will describe the results obtained in this thesis work by XMCD and XNLD characterization of the evaporated Fe_4Ph and $TbPc_2$ monolayer on different surfaces.

Chapter 5.

X-Ray studies of the thermally evaporated Fe_4Ph monolayer

5.1. Introduction

The experiments described in this chapter have been carried out thanks to the experience acquired in the thermal evaporation of the molecules and to the use of highly performing light sources: the ID08 beamline at ESRF in Grenoble and the SIM-X11MA beamline at SLS in Villigen.

In particular we will describe the XMCD and the XNLD characterization of the thermally evaporated Fe_4Ph monolayer on diamagnetic metallic surfaces, such as Au and Cu, and magnetic surfaces, such as metallic Co film growth on Cu and the lanthanium strontium manganite, LSMO, substrate whose application in the field of spintronics has been described in the paragraph 2.4. As we have underlined in the previous chapters the evaporability of Fe_4 SMM could allow to investigate the transport properties of molecular spintronics devices based on SMMs. In particular here we will highlight how the magnetic properties and in particular the dynamics of the magnetization of Fe_4Ph depend on the nature of the substrate.

5.2. Preliminary morphological study on the deposition of the evaporated monolayer

Before describing the magnetic properties of the evaporated monolayer, we briefly summarize the first attempt of thermal evaporation of Fe_4Ph monolayer carried out at the University of Genova and the morphological characterization.

The substrates used for Fe_4Ph monolayer was evaporated gold (150-200 nm) on mica (Agilent Technologies). In order to improve the quality of the surface, a flame annealing process was carried out with an hydrogen flame (see experimental section). As discussed in the section concerning the characterization of the thick films, we calibrated the monolayer by monitoring the pressure, the temperature and the density of the deposited thickness during the evaporation procedure. In order to accurately control the deposition coverage we worked with a low and constant flux of molecule attaining slowly the deposition temperature. In particular the evaporation was conducted adjusting the deposition rate to a value between 0.5 and 0.7 Å /s. The substrate was exposed to the constant molecular flux once reached a temperature of 280°C, a pressure of 3×10^{-5} mbar and when QCM was able to read the deposited thickness. Subsequently the presence of a monolayer was confirmed through the acquisition of images carried out *ex-situ* by Scanning Tunneling Microscopy, STM, (see experimental section) that revealed the presence of round objects of ca. 2 nm, in good agreement with the dimensions of the molecules as determined from crystallographic data. Interesting we noted that all the inspected areas were homogeneously covered with only few densely packed molecules. A representative topography image of the monolayer obtained is given in **Figure 5.1**.

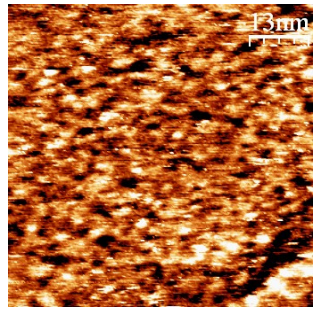

Figure 5.1 STM topography images of the evaporated Fe_4Ph monolayer. The most efficient tunneling conditions was reach using U = 0.5 V, I = 8.9 pA.

5.3. Evaporation procedure used at Synchrotrons Radiation Light Source: ESRF and SLS

Both synchrotrons endstation we used for these experiment have the facilities to evaporate and to measure XAS *in situ* without losing the UHV conditions. In the set up used in the Grenoble beamline we have taken advantage from the possibility to clean the surface by sputtering and annealing and thus we used Gold (111), Cu(100) single crystals and LSMO. Moreover this set up is able to

evaporate in situ ferromagnetic metal, like cobalt, overcoming the problem of the easy oxidation of the first layers of the surface exposed to the air. In **Figure 5.2** is reported a simple sketch of the used apparatus. In the experimental section we will describe the cleaning process of the substrates used in the experiments carried at ESRF.

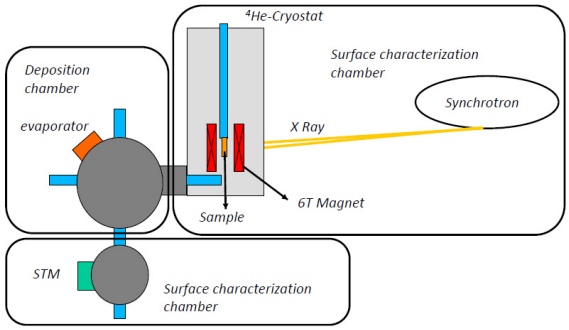

Figure 5.2: Sketch of the ESRF set up formed by the deposition chamber, the STM and magnetic characterization chamber.

Unfortunately this set up is equipped with a ^{4}He cryostat that cannot reach temperatures on the sample below ca. 8 K. Since Fe_4Ph SMM shows the opening of the typical hysteresis only below 1 K, we have been obliged to complete our investigation at SLS where the beamline is equipped with a ^{3}He-^{4}He dilution system, the French TBT endstation,[93] which is able to reach temperatures of the order of few hundreds mK (for more details on this set up see experimental section) (**Figure 5.3**).

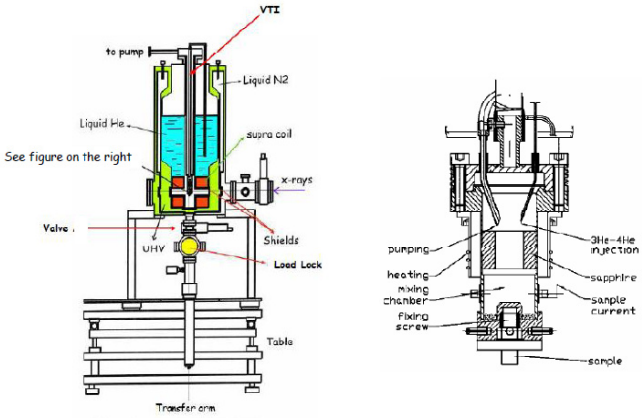

Figure 5.3: Sketch of the cryostat used at the SLS beamline (on the left) and of the ^{3}He-^{4}He dilution set-up (on the right).

The SLS set up allows the *in situ* evaporation of molecules, but not of ferromagnetic metals. Moreover it is not possible to clean the substrates by sputtering and annealing procedures. For this reason Fe_4Ph monolayer samples investigated at the SLS synchrotron were evaporated on gold coated mica and on LSMO substrates. In the last case the magnetic properties are independent from the cleaning procedure as we will demonstrated in the next paragraph. Finally we have to specify that at both Synchrotrons, although for different reasons, we could not employ the QCM to estimate the thickness of the deposit. We therefore monitored the pressure, the temperature, the deposition time, and correlated them to the XAS intensity to estimate the thickness of the deposit.

As we shall describe in the next paragraph, the first evaporation of Fe_4Ph on Au(111) carried out in the ESRF Synchrotron revealed the presence of a small fraction of thermal decomposition products, confirming the results obtained by the EPR experiments on the thick film discussed in **Chapter 3**. After many efforts and a deep study of the deposition parameters we have identified a procedure that allows to isolate the pure Fe_4Ph from the film the decomposition products. We can summarize this procedure in three main points. The figures described below were acquired in the SLS Synchrothron, but can be extended to the experiments carried out at the ESRF:

1) *Degassing process of the powder*. In **Figure 5.4** it is reported the pressure dependence as a function of the temperature revealed by two different pressure sensors: one placed close to the evaporator and the other one placed close to the tube pump. Obviously, the pressure revealed near the evaporator is higher than the other one. In this first step we heated the powder up to 190°C and we degassed all the solvent used to wash the crucible and some impurities of the powder.

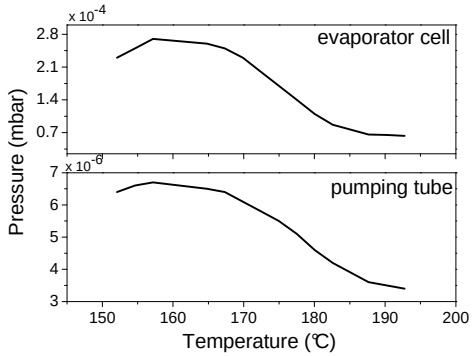

Figure 5.4: Pressure profile as function of the temperature of the degassing process of Fe_4Ph molecules.

2) *First heating process*. In **Figure 5.5** is reported the pressure curves as a function of the temperature of the first heating process. We can observe the presence of the peak at 220°C that in **Chapter 3** we attributed to a paramagnetic impurities of the mononuclear compound $Fe(dpm)_3$.

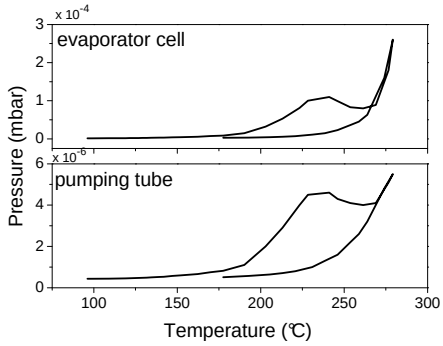

Figure 5.5: Pressure profile of the first heating process as function of temperature of Fe_4Ph molecules.

3) *Cleaning process*. In order to purify the powder and to eliminate all the impurities, we heated and cooled down the powder for three times. We observed that after the first heating process the peak at 220 °C disappears. **In Figure 5.6** are represented three different cycles with different colors. The black line indicates the last step: the evaporation of the monolayer.

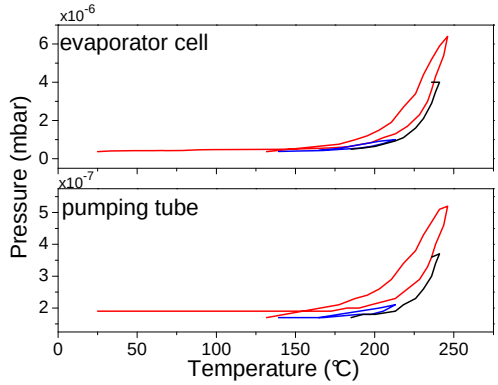

Figure 5.6: Pressure profile as function of temperature of the cleaning process (red and blue line) and of the evaporation process (black line) of Fe_4Ph molecules.

5.3.1. Characterization of monolayers by XAS signal

In order to check the coverage of the molecules on surface we used the X-Ray Absorption spectra. In fact since the ratio between the Edge jump and pre-edge signal ($\frac{I_{peak}-I_{pre}}{I_{pre}}$) can be related to the amount of molecules covering the surface, we compared the XAS of the evaporated film with those obtained for a monolayer deposit formed using the Self Assembly technique. In **Figure 5.7** are reported only some examples of samples evaporated at SLS synchrotron with different deposition times. The black square not connect to the line corresponds to the reference measurement obtained for Fe_4C_9Sac self assembled from solution on gold surface and considered to correspond to the monolayer coverage.

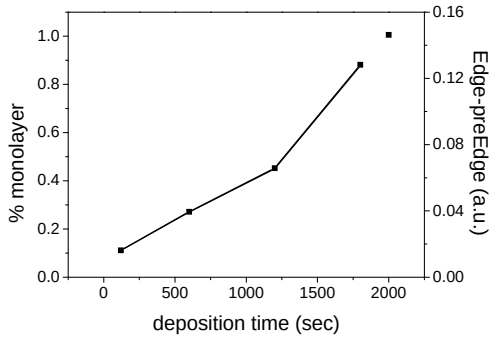

Figure 5.7: XAS signal and coverage percentage of monolayer as function of the deposition time. The symbol not connected by the line is related to Fe_4C_9Sac deposited by Self Assembly technique.

5.3.2. X-Ray studies of the LSMO substrate

Before using the substrate for the evaporation of Fe_4Ph we investigated the electronic structure and the magnetic properties of the LSMO by XAS/XMCD. This analysis was carried out at ESRF Synchrotron before and after the annealing procedure in order to understand if this process, apart from removing the carbon contamination of the surface, affects the chemical structures and the oxygen stoichiometry of the LSMO. In **Figure 5.8** we have reported the complete magnetic characterization performed at the $L_{2,3}$-Mn Edge for a LSMO sample on $NdGaO_3$ substrate (see experimental section) before the annealing procedure. XMCD spectra have been obtained as the difference of two sets XAS spectra with photon helicity parallel and antiparallel to the external field respectively (see

experimental section).[94] TEY detection mode has been used as detector to probe the first layer of the surface. The spectra indicated as XAS are the isotropic spectra (i.e. the average of the two dichroic spectra); this formalism have been adopted throughout the text. The XMCD spectrum recorded at a magnetic field of 3T and T = 8K did not reveal any difference by changing the angle of incidence of the photons, indicated by the angle θ with the normal to the surface. This finding is well rationalized with the fact that the magnetic anisotropy of LMSO is completely overcome by a 3T magnetic field. On the contrary the effect of decreasing the temperature from 300 K to 8 K induces a significant increase in the XMCD signal.

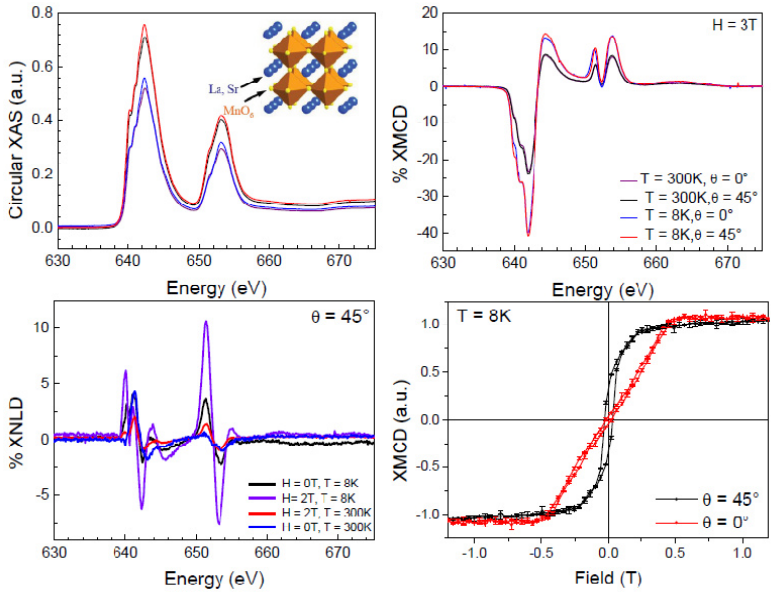

Figure 5.8: Experimental XAS, XMCD, XNLD and Magnetization curves of the LSMO substrate before the annealing process. Dichroic percentage contribution in the XMCD and XNLD spectra are normalized to the isotropic signal at its maximum. In the inset of the XAS spectrum the crystal structure of the LSMO is reported.

Also the linear dichroism defined as the difference between vertically, σ^{V}, and horizontally, σ^{H}, polarized light, has been measured at θ = 45° both in zero field and in an applied field of 2 T. The presence of a signal in zero field is consistent with the epitaxial growth of LSMO on $NdGaO_3$ substrate. Finally, in order to investigate the field dependence of the magnetization, the photon energy corresponding to the strongest negative XMCD peak at L_3-edge (642 eV) was

selected and the results are shown in **Figure 5.8**. The hysteresis loop at 8 K and θ = 45° propagation showed a coercive field of 1.7 mT. By setting the θ angle at 0° we observed that the saturation value was not changed, in agreement with the XMCD spectra discussed above, but saturation is achieved at a higher field and the coercive field was significantly reduced, thus confirming the presence of an in-plane easy magnetization anisotropy.

In **Figure 5.9** we have reported the XMCD investigation carried out on the same LSMO substrate after the annealing procedure. These data are in complete agreement with those reported in the literature, confirming that the cleaning process produces only few changes. In fact we observed first of all an increased intensity in the XMCD, XNLD spectra as well as an increase of the saturation value of the magnetization. The annealing process confirmed thus to be useful to eliminate the carbon impurities on the surface and to improve the XMCD signal without significant modifications of the magnetic properties.

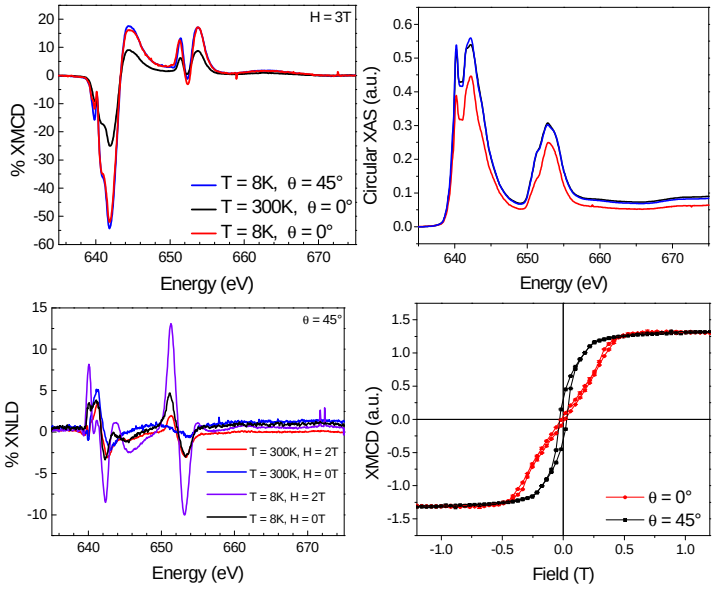

Figure 5.9: XAS, XMCD XNLD and Magnetization curves of the LSMO substrates after the annealing process.

The main difference detectable is the appearance in the XAS and XMCD spectrum of the annealed sample of an additional peak at 639.8 eV **(Figure 5.10)**, evidenced in the figure by an arrow, that was attributed to the presence of a little amount of Mn^{2+} ions.[95] This could be caused by the valence instability of the Mn^{3+} ions that tends to dismutate in Mn^{4+} and Mn^{2+} species during the annealing procedure.

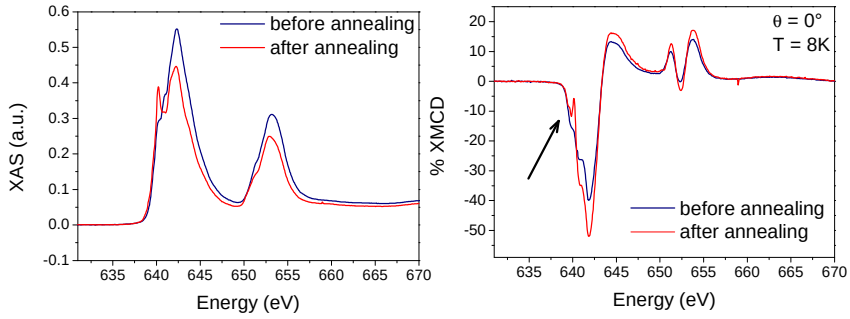

Figure 5.10: Comparison between the XAS and XMCD spectra of the LSMO substrate before the annealing (blue line) and after the annealing (red line).

5.4. XMCD studies on evaporated Fe_4Ph Monolayers on different surfaces

In this paragraph we will describe the XAS/XMCD studies of Fe_4Ph evaporated monolayer and we will use as reference the results obtained on Fe_4C_9SAc monolayer deposited on gold surface by self assembly technique described in **Chapter 2**. The first thermal evaporation of Fe_4Ph SMM was recorded at ESRF Synchrotron on Au(111) single crystal without carrying out the pre-treatment procedure of the powder described in the previous section and then without discarding the first fraction of the evaporated molecules. From the investigation of the isotropic signal of the XAS spectra we estimated a molecular sub-monolayer coverage of Fe_4Ph SMM of ca. 30%.

In **Figure 5.8** are reported the XAS and XMCD spectra at the Fe-$L_{2,3}$ edge obtained at T=8 K by applying an external magnetic field of 3 and 5T normal to the surface of the evaporated film.

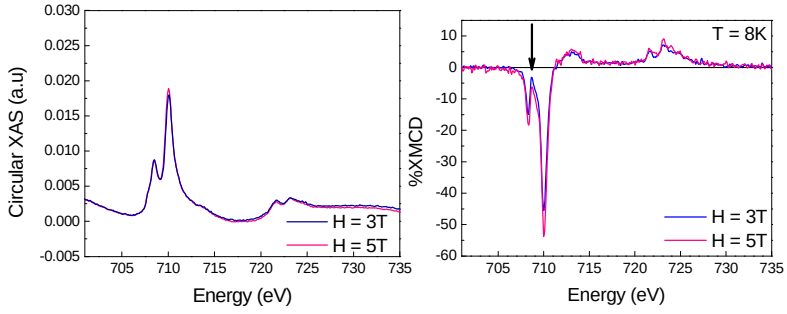

Figure 5.11: Experimental XAS and XMCD spectra of Fe_4Ph SMM evaporated on the (111) face of a gold single crystal measured at T = 8 K and H = 3 and 5T.

The shape of the XAS spectra gave indication that no photoreduction was occurring during the experiments or during the thermal treatment. On the other hand XMCD spectra was found to be not in complete agreement with the features observed in the intact monolayer deposit of Fe_4C_9SAc molecules reported in the **Chapter 4**. In the latter case the ferromagnetic arrangement of the iron(III) spins and the slightly different crystal field of central and external iron sites was considered at the origin of XMCD feature at ca. 707.9 eV. A weak but non-zero signal was observed in this sample, although the intensity of the XMCD signal at 710 eV is in good agreement with those reported in literature and was only slightly higher than that observed for Fe_4C_9Sac (45% compared to the 39% for Fe_4C_9Sac self assembled).[67] This confirmed that the antiferromagnetic coupling between the central ion and the three peripheral ones is substantially retained. We tentatively attributed the observed small difference to the presence of impurities of a paramagnetic compound generated as a consequence of the first fraction of the thermal evaporation in agreement with the EPR signal centered at g = 2 already discussed in **Chapter 3** (paragraph 3.3.5).

X-ray Natural Linear Dichroism, was measured setting the angle θ to 45° and the temperature to 8K. The presence of a small dichroic signal (**Figure 5.9**) evidenced that the molecules had a preferential orientation in the film. The shape of the XNLD spectrum, although very weak is similar to that reported recently by Mannini and co workers on a self assembled monolayer of a thioacetyl functionalized Fe_4 with a shorter linker, carrying only a five carbons in the aliphatic chain instead of the nine present in the first investigations. [68, 81] In the case of Fe_4C_5Sac a preferential orientation of the molecules on the surface, with the trigonal molecular axis distributed inside a cone defined by an angle $\theta_D = 35°$, was predicted by DFT calculations and confirmed by both linear and circular dichroism investigations. [68]

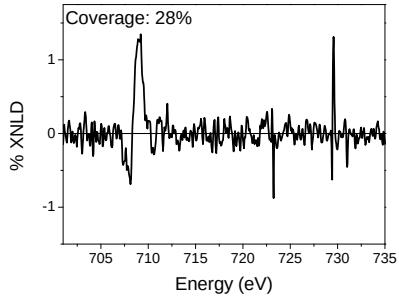

Figure 5.12: XNLD spectra of Fe_4Ph SMM evaporated on Gold surface recorded at θ = 45° and H = 3T and T = 8K.

The magnetization curves obtained following the XMCD signal at L_3 edge in function of the magnetic field at the two temperatures (T = 8K and 15 K) were compared with magnetization curves calculated for a random distribution of molecular orientation. These are reported in **Figure 5.13** as solid dark gray lines superimposed to the experimental data. The Spin-Hamiltonian parameters used in the simulation (Eq. 1.2) were those determined from magnetic investigation of bulk, i.e. S = 5, and $D/k_B = -0.44$ cm^{-1}. As can be seen, the agreement between calculated and experimental data are very good at 8K temperature, thus confirming that the magnetic properties are unaltered, and even if they are not completely superimposable at 15K, deviations are comparable to the experimental error. At T = 8K the field dependence of the XMCD intensity was measured by applying the field normal to the surface and at 45°. However, no significant differences are observed. On the contrary, by assuming in the simulation of the magnetization curves that a preferential orientation of the easy axis of magnetization is achieved similarly to the case of Fe_4C_5Sac, a significant difference between the two field orientations is expected (see **Figure 5.13** right). This result is apparently in contradiction with the observation of the XNLD signal. However, from the very weak intensity of the observed signal compared to the noise, we can expect only a limited preferential orientation of the molecules on the surface.

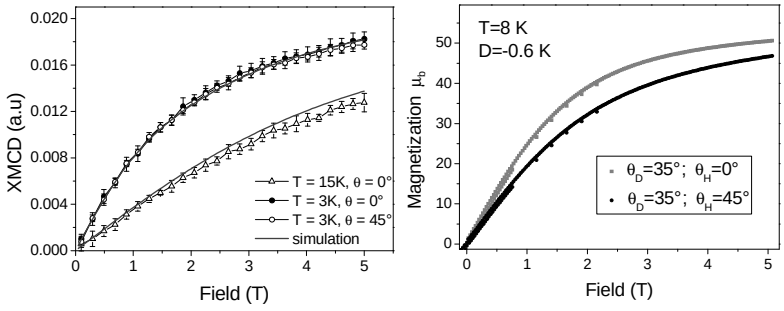

Figure 5.13: on the left magnetization curves of Fe_4Ph SMM evaporated on Au(111) single crystal at different temperatures and angles. The continuous lines represent the simulation obtained for a random distribution of the molecules on surface. On the right magnetization curves calculated at two angles by assuming the presence of orientation of the molecular axis inside a cone defined by a distribution of angle $\theta_D = 35°$.

We have also to keep in mind that this evaporated sample contains a low coverage of the molecule on surface and that a little percentage of these are damaged during the thermal treatment. For this reason we refined these results modifying the preparation of the sample by excluding the first fraction of the

evaporated molecules (following the procedure described in the paragraph 5.3) and increasing the coverage. In this case in order to establish a preliminary work that involve the evaporation of metals like cobalt or nickel, we chose a Cu(111) single crystal as surface since it facilitates the epitaxial grow along the crystallographic cell. In **Figure 5.14** we have reported the XAS and XMCD spectra recorded applying a magnetic field of 3T and 5T at a temperature of 8K. The analysis of the intensity of L_3 Edge jump of the XAS peak normalized respect the pre-edge at 705 eV revealed a coverage of ca 80%. Moreover in the XMCD spectrum reported in **Figure 5.14** we observed the typical feature of the intact Fe_4 core as evidence by the dichroic signal going back to zero at 707.9 eV. As already discussed, this fingerprint confirms the antiferromagnetic coupling of the central Fe with the three external ones and suggests the absence of any paramagnetic impurities due to the thermal decomposition of Fe_4 molecules.

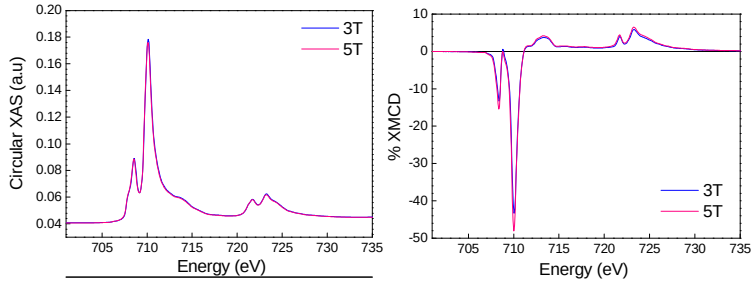

Figure 5.14: field dependence of the XAS and XMCD spectra of Fe_4Ph SMM evaporated on Cu(100) single crystal recorded at T = 8K and θ =0°.

The magnetization curve recorded at 8K and 15K (**Figure 5.15**) were quite similar to those detected in the deposited thick film by a traditional magnetometer and in the evaporated monolayer on Au(111) including a low saturation value at a higher temperature thus confirming the anisotropy of the sample.

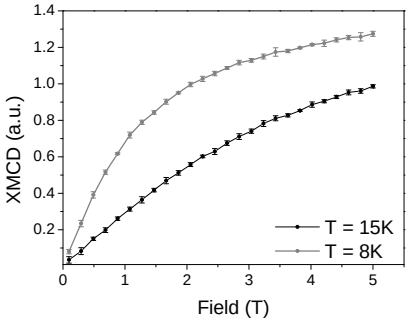

Figure 5.15: Magnetization curves of Fe_4Ph evaporated on Cu(111) single crystal recorded at two different temperatures and at θ = 0°.

In order to clarify the presence of a preferential orientation on surface and to understand if it depends on the percentage of evaporated molecules on substrate, we prepared another sample using the more conservative thermal treatment that discard the first fraction of the evaporation. The thermal evaporation was performed on Au(111) single crystal obtaining a coverage of the substrate of ca 80%.

The choice to shift back to the gold substrate was motivated by the fact that flat terraces are easily obtained for this substrate. In **Figure 5.16** we have reported the XMCD spectra recorded at two different angle ($\theta = 0°$ and $\theta = 45°$) in which was evident that almost superimposable curves were obtained. Also the magnetization curves recorded at 8 K and at two different angles (45° and 0°) were almost coincident. The XNLD spectra showed a little percentage of noisy dichroic signal that could be attributed to a partial orientation of the molecule. Also in this case we have to take into account the high signal/noise ratio of the XNLD did not allow to estimate the fraction of molecules lying with their easy axis preferentially along the normal to the surface.

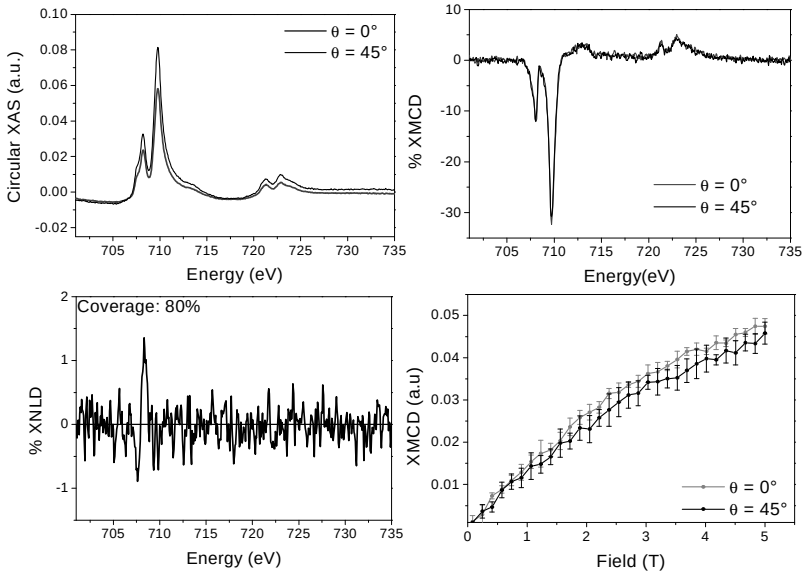

Figure 5.16: on the top part XAS and XMCD spectra recorded at two different angles respect the photon propagation at T = 8K and H = 3T; on the bottom part XNLD (carried out at $\theta = 45°$, T = 8K and H = 2T) and magnetization curves (T = 8K)of the evaporated Fe_4Ph monolayer on the Au(111) single crystal.

Finally the XNLD spectra in function of three different percentages of coverage by molecules deposited on gold surface (30%, 50% and 80%) was investigated. We observed as the XNLD signal strongly depends on the percentage of coverage of the gold surface with evaporated molecules increasing in presence of a low coverage (**Figure 5.17**).

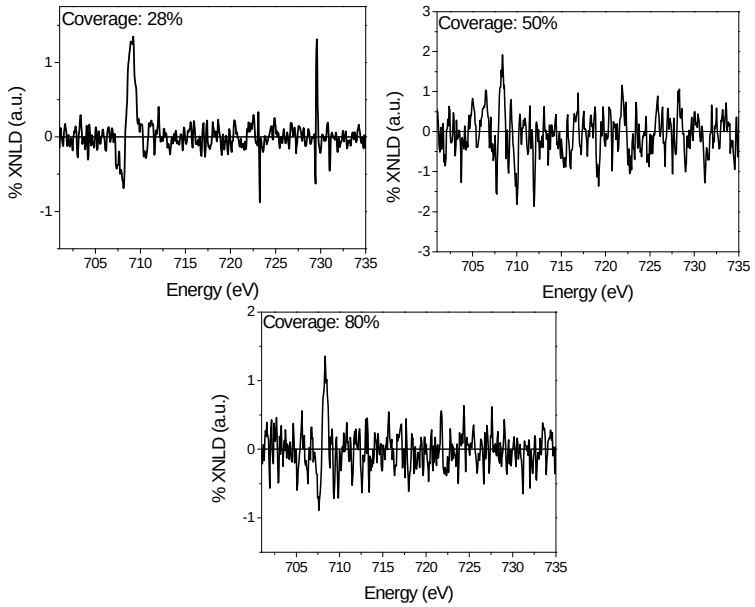

Figure 5.17: Comparison between the XNLD spectra of Fe_4Ph evaporated on Au(111) single crystal with different coverage measured at T = 8K, H= 2T and $\theta = 45°$.

Since molecular spintronics devices are fabricated using LSMO and Co as electrode, we investigated the magnetic properties of Fe_4Ph on this two substrates in order to verify if the substrates could modify the chemical and magnetic properties of Fe_4Ph evaporated monolayer. Thermal evaporation of Fe_4Ph monolayer was conduct on LSMO. Since the background signal of the XAS spectra strongly depend on the substrate, we could not estimate exactly the coverage because we had no data on the SAM deposited on this surface; although comparing the deposition time with those used for the deposition on gold substrates, we can estimate a coverage of ca. 50%. The XMCD spectra recorded at the Fe $L_{2,3}$ Edge confirmed the ferrimagnetic structure of intact Fe_4 and revealed the same intensity of the XMCD signal at two different angles. The magnetization curves recorded at two different angles were almost

superimposable and the XNLD spectrum recorded at 45° angle and a 2T showed the presence of a weak and noisy signal demonstrating that only a very low percentage of molecules, if any at all, are oriented on the surface (**Figure 5.18)**. This result did not surprise us as LSMO substrates are more rough than metallic ones.

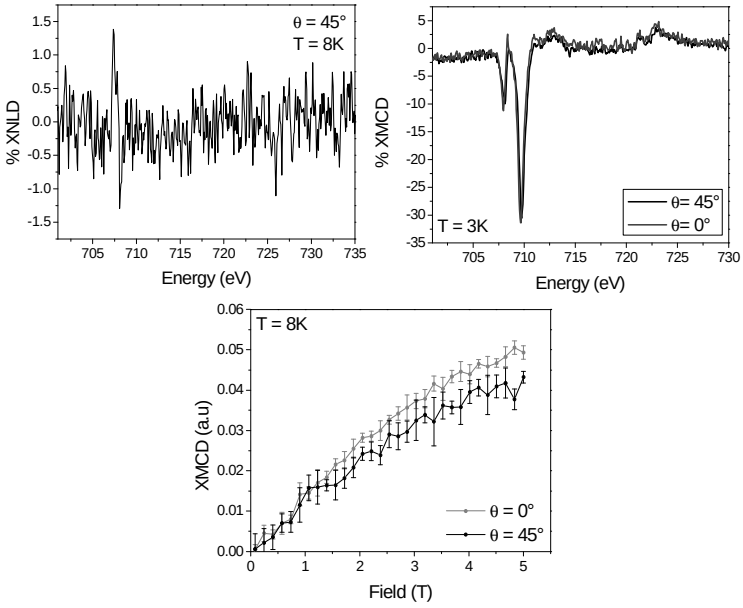

Figure 5.18: XMCD, XNLD recorded at the $L_{2,3}$ Fe-Edge at T = 8K and H = 2T and magnetization curves carried out at T =8K of Fe_4Ph evaporated on LSMO.

We also checked if the deposition of Fe_4Ph molecules induced any change in the electronic and magnetic properties of LSMO by repeating the investigation done on pristine and thermally annealed LSMO substrates after the evaporation of Fe_4Ph. The XMCD spectra at the Mn-edge showed identical shape and intensity to those detected for the LSMO substrate reported above, including the presence of the Mn^{2+} peak generated after the thermal annealing procedure. The presence of a XNLD signal and the shape of the hysteresis loop were recorded at different angles and confirmed the observed magnetic anisotropy of the LSMO substrate (**Figure 5.19**). These results proved that Fe_4 molecules did not induce any significant modification in the substrate structure.

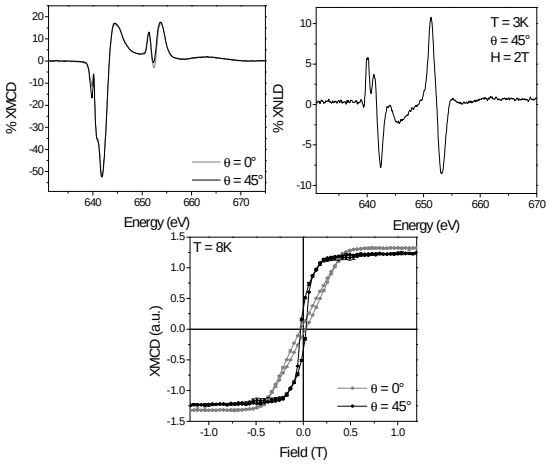

Figure 5.19: XMCD, XNLD and magnetization curves recorded at the $L_{2,3}$ Mn-Edge of Fe_4Ph SMM evaporated on LSMO substrate

Finally a preliminary investigation on the electronic and magnetic structure of Fe_4 evaporated on a Co surface was performed. In **Figure 5.20** is reported the XAS and XMCD spectra carried out at the Fe $L_{2,3}$-edge with T = 8K in a 3T magnetic field. On the basis of the deposition time we have estimated a coverage of the surface of ca. 50%. The XMCD spectra clearly indicate the presence of the intact Fe_4 core structure characterized by the ferrimagnetic spin arrangement. Unfortunately we have no data on the XNLD spectrum, but the magnetization curves at two different angles (0° and 45°) reveals some orientation. The absence of deep investigation due to the impossibility to evaporate the metal substrate at the SLS synchrotron radiation prevent us to make any conclusion on possible effects of the magnetic substrate on the dynamics of the magnetization of Fe_4, and we are working to make this kind of experiments possible in a future assigned beamtime.

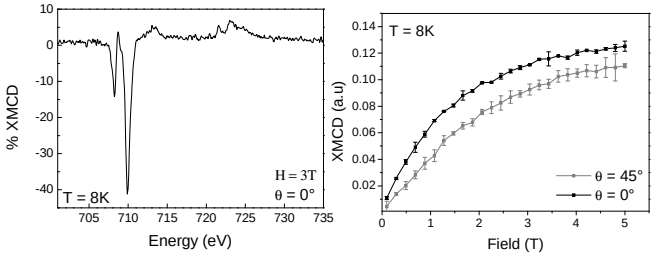

Figure 5.20: XMCD and magnetization curves of Fe_4Ph SMM evaporated on Co film recorded at T =8K.

5.5. Dynamics of magnetization studies on the evaporated monolayer

Once demonstrated that the spin structure and the oxidation state of the evaporated monolayer is retained regardless of the substrate we investigated in detail the dynamics of the magnetization of the grafted molecules measuring the field dependence of the magnetization selecting the negative XMCD peak at the L_3-Edge. This kind of measurements were performed at the SLS synchrotron that, as we have described in the first section of this Chapter, is able to reach sub-Kelvin temperatures.

The evaporation of Fe_4Ph on Au coated mica substrate was conducted in parallel with that made for LSMO thus obtaining the same coverage of the surface, i.e. ca. 80%.

We will start with the description of Fe_4 evaporated on gold surface. In order to be sure that Fe_4Ph was evaporated without producing any decomposition we have performed a XAS and XMCD at 600 mK with the sample normal respect to the photon propagation and the magnetic field. The XMCD spectra reported in **Figure 5.21** confirmed the presence of the antiferromagnetic spin coupling of the intact Fe_4 core.

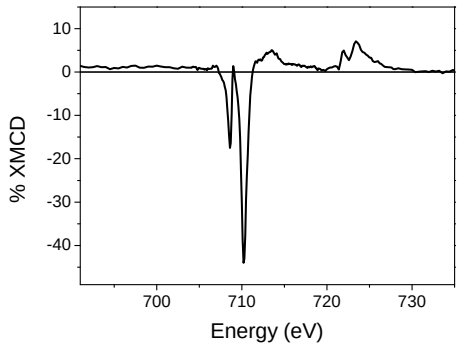

Figure 5.21: XMCD spectrum of Fe_4Ph evaporated on Gold coated on mica substrate recorded at T = 8K, H = 600 mK and θ = 0°.

After finding the exact energy at which the XMCD signal is maximum in its absolute value (710 eV), we recorded the hysteresis loops at the same temperature as that at which XAS and XMCD spectra were acquired. The magnetization curves recorded as a function of the θ angles (**Figure 5.22**), clearly show the

presence of the opening of the hysteresis loop with the strong tunneling of Fe_4 SMM in zero field that is at the origin of the butterfly shape.

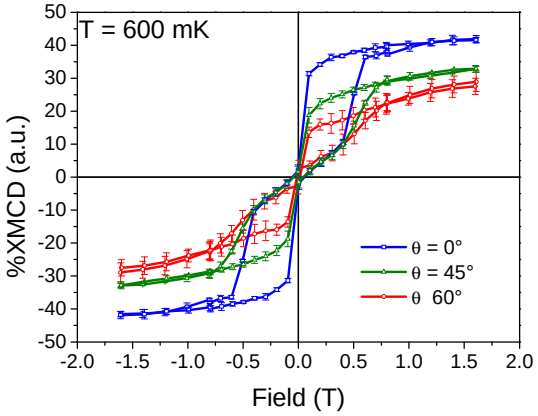

Figure 5.22: Hysteresis curves of Fe_4Ph SMM evaporated on Gold substrate recorded at different angles.

Moreover the angular dependence of the magnetization, which is largest when the sample is normal respect to the magnetic field, revealed the presence of a preferential orientation of the molecule and thus of the easy axis of magnetization on surface. This observation is in agreement with the presence of a weak XNLD signal detected at ESRF at a higher temperatures reported in **Figure 5.12**.The angular dependence of the hysteresis loops strongly resembles that observed in the monolayer of partially oriented Fe_4C_5Sac molecules.[68] In that case, the recorded hysteresis loops revealed evident steps at ± 0.5 T, attributed to the resonant quantum tunneling occurring at the first level crossing, $H_1=|D|/g\mu B$. On increasing the angle between the field and the normal to the surface a smoothing of the step and its shift to higher field was detected. A very similar behavior is indeed observed for the evaporated film of Fe_4Ph as shown in **Figure 5.22**.

It has also been possible to measure the time decay of the XMCD signal after having rapidly changed the polarization of the magnetic field. For this type of measurement, previously employed to characterize a self assembled monolayer of Fe_4C_9Sac,[67] the fast polarization switching obtained with the tune/detune mode, coupled to the extreme beam stability at SLS, proved to be a necessary condition for the success of the experiment. In the present case the experiment was conducted by magnetizing the sample with a rather strong field (1.6T) and then quickly sweeping the field either to zero or to a very small value of opposite sign (–0.25T) measuring the XMCD signal as a function of time. The time decay of the XMCD signal was recorded at two different angles (θ =0° and 45°), and are

shown in **Figure 5.23** where a clear time dependence of the signal is visible. The magnetization decay process of dynamic origin can be modeled as a mono-exponential process:

$$I(t) = I_\infty + (I_0 - I_\infty)e^{-\frac{t}{\tau}}$$

where I, I_0 and I_∞ represent the XMCD intensity at the time t, at the beginning of the experiments (t = 0) and at the equilibrium (t = ∞) respectively and τ is the characteristic time of the process. This equation was used to fit the two time decays measured at θ= 0° and 45°.The fittings, represented in **Figure 5.23** as solid lines coincided to the experimental data, gave the values of the characteristic time of the process τ , which is, as expect, higher when the sample is perpendicular to the magnetic field. Such values, τ = 1101 (18) s at θ = 0° and τ = 635 (17) s at θ = 45°, was compared to those estimated from the Arrhenius law with U_{eff} = 15.6 K and a $\tau_0 = 1.9\times10^{-8}$ sec estimated from the ac susceptibility of bulk Fe_4Ph crystals. The results are comparable within the incertitude on the temperature of the XMCD experiments.

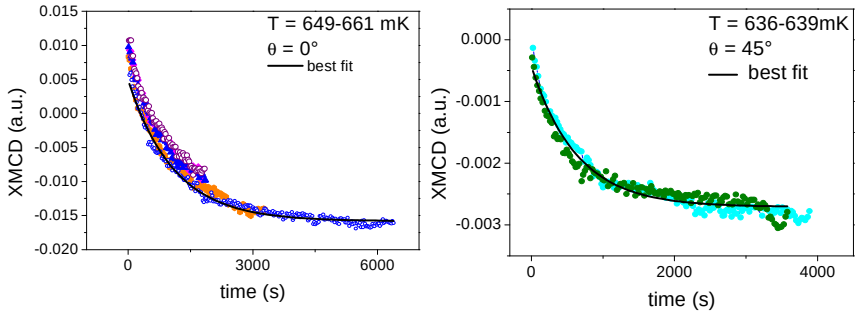

Figure 5.23: time decay measurement of the XMCD signal of Fe_4Ph evaporated on Gold at different angles

The opening of the hysteresis, the time decay experiments and the field dependence of the magnetization measured in XMCD experiments confirmed that Fe_4Ph evaporated monolayer maintains also the typical slow dynamics of the magnetization that characterizes a SMM. This finding opens the possibility to extend this investigation to LSMO and possibly detect the effects of the interaction with the magnetic substrates in the SMM behavior.

The preliminary XAS/XMCD study carried out on the Fe and Mn -$L_{2,3}$ edge are reported in **Figure 5.24**. While the spectra recorded at the Fe-Edge revealed

the typical feature of the spin coupling of the intact Fe_4, in agreement with the results obtained at ESRF and reported in **Figure 5.18**, the XMCD relative to the Mn-Edge showed some differences compared to the ones recorded at ESRF. In particular the XMCD spectrum shows a significant contribution at 640.5 eV. We can formulate several hypothesis on the observed differences. The very low temperatures used in this investigation have never been employed to characterize LSMO, which has a relatively high Curie temperature. However, we believe that is rather unlikely that the observed differences are solely due to the very low temperature used in the investigation. We have to remind that he SLS set-up does not allow thermal treatment of the substrate. However, we have shown above that minor changes in the spectral features are induced by the thermal heating. The last hypothesis is that the LSMO substrate was from origin slightly different from the batches used at ESRF. Unfortunately the very limited beam time and the complexity of the measurement procedures at this end-station reaching very low temperatures did not allow us to perform a complete characterization of the LSMO substrate before the deposition of Fe_4Ph.

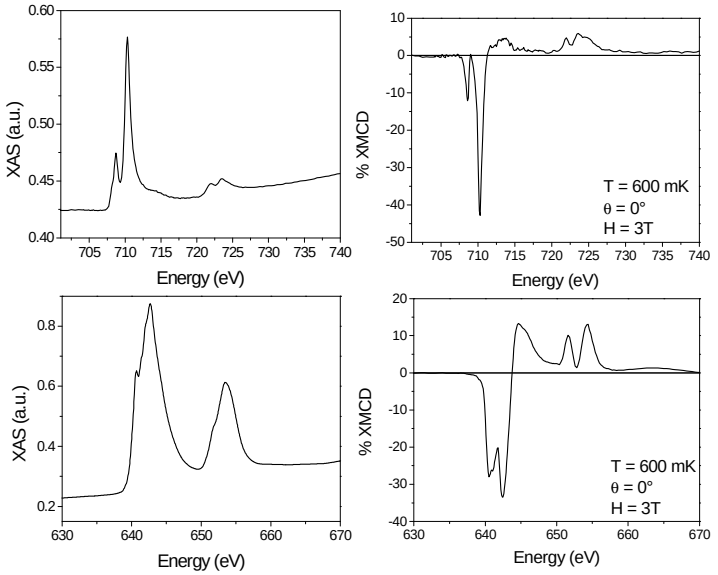

Figure 5.24: on top part is reported the XAS, XMCD spectra of Fe_4Ph evaporated on LSMO substrate recorded at the $L_{2,3}$-Fe Edge. On the bottom part is reported the XAS and XMCD spectra of Fe_4Ph evaporated on LSMO recorded at the $L_{2,3}$-Mn Edge.

However, we monitored the XMCD signal at the Mn- L_3 edge as a function of the applied magnetic field and of the θ angle and the hysteresis loops obtained, shown in **Figure 5.25**, well compared with those recorded at the ESRS synchrotron (**Figure 5.9**). In particular the saturation value of the magnetization did not change with the angle, but the different shape observed for θ = 45° and θ=60° compared to θ= 0° confirmed in plane magnetization anisotropy.

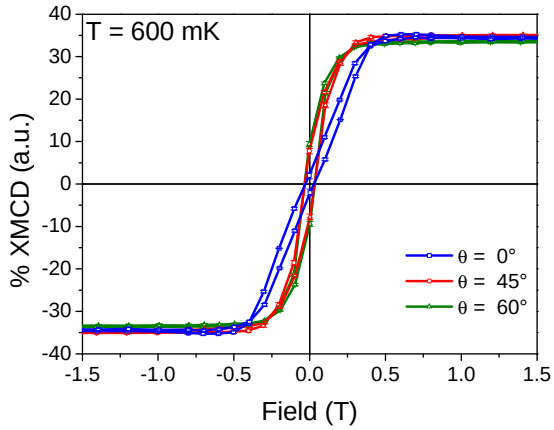

Figure 5.25: Hysteresis curves of Fe_4Ph evaporated on LSMO substrates recorded at the L_3 Mn-Egde

We can therefore assert that the overall magnetic behavior of LSMO is not affected by the presence of Fe_4 SMM. At this point we wonder whether is also possible the inverse effect, i.e. if the manganite surface can influence the dynamics of the magnetization of Fe_4 molecules. Surprisingly when we moved to the Fe-L_3 Edge to follow the XMCD signal as a function of the applied field we obtained a drastic change in the dynamics of Fe_4 as evidenced by the disappearance of the typical butterfly shape of the hysteresis. The remnant magnetization in zero field was visible for all the three investigated angles and is particularly large when the surface is normal to the magnetic field. Moreover the angular dependence of the saturation value of the magnetization revealed a much lower difference between the three angles compared to what observed for the evaporated monolayer on gold surface. This behavior indicated a lower orientation of the molecules on surface, confirming the XNLD data obtained at the ESRF beam line and can be rationalized taking into account that LSMO substrates are much rougher than metallic ones.

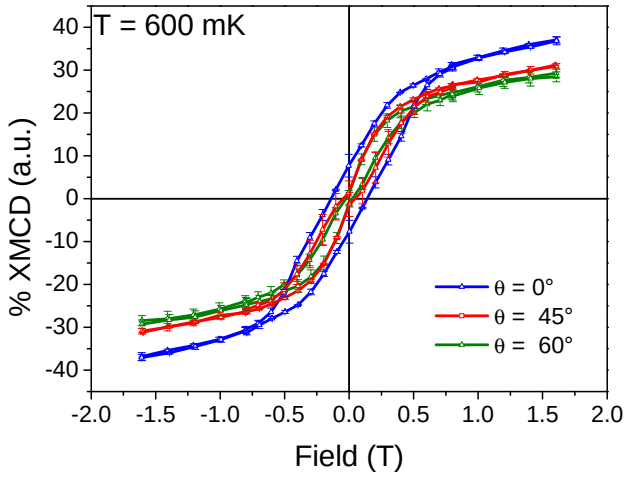

Figure 5.26: Hysteresis curves of Fe_4Ph evaporated on LSMO surface recorded at the Fe-Edge.

Another interesting observation can be done considering the hysteresis shape. Indeed increasing the θ angle with the photon propagation, the remnant magnetization contribution in zero field decreased significantly becoming much more similar to those recorded for the manganite substrate.

Finally, further evidences of the presence of slow relaxation of magnetization were gathered by measuring the time decay of the XMCD signal, in the same way it was done for Fe_4 evaporated on gold surface. In fact also in this sample the time decay curve of the monolayer was obtained magnetizing the sample in a strong positive magnetic field (1.6T), then sweeping the field to a very small value of opposite sign (– 0.25T), and measuring the XMCD signal as a function of the elapsed time. The measurement was repeated following the dichroic signal at both Mn and Fe L_3-Edges and at different angles. In **Figure 5.27** the time decay detected with the sample normal to the applied field is reported. We can observe that the time evolution recorded at the Mn-Edge is significantly noisier and decays in opposite direction than the ones measured on the Fe-Edge. The fitting made with the mono-exponential decay function is shown as the solid line and gave the relaxation time value of $\tau = 218(21)$s. The same measurement performed at the Fe-Edge gave the value of $\tau = 255(11)$ s, which is lower than that observed for Fe_4 evaporated on gold sample but still comparable.

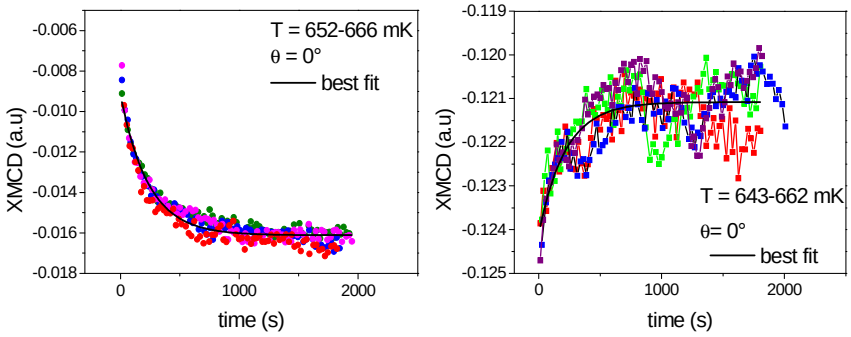

Figure 5.27: Time decay measurements of Fe_4Ph evaporated on Au surface recorded at the Fe edge (on the left) and Mn edge (on the right).

Surprisingly rotating the sample the time decay of the Fe disappears while that detected at the Mn edge become increasingly noisy (**Figure 5.28**).

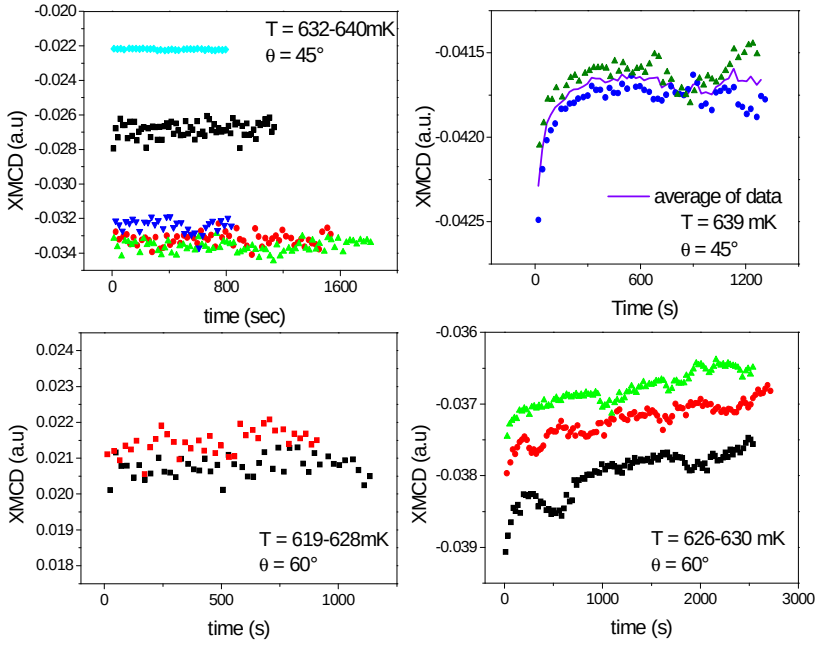

Figure 5.28: Time decay measurement of Fe_4Ph evaporated on LSMO surface recorded at different angles. In the left part are reported the data obtained at the Fe-Edge and on the right part are reported the data obtained at the Mn edge.

Both hysteresis loops and the time decays experiments clearly indicated an influence of the LSMO substrate on the dynamics of the magnetization of the evaporated Fe_4Ph. This influence becomes important and more visible when the sample is no more orthogonal to the magnetic field, i.e. when the field is closer to the in plane magnetization of the LSMO substrate. The observed opposite trend of the Mn-Edge signal compared to the Fe- Edge one in the time decay experiments could suggest an antiferromagnetic coupling between the magnetic moment of the substrate and those of Fe_4 SMMs. Further experiments, and in particular the investigation of the time dependence of the XMCD signal in pristine LSMO substrates are necessary to confirm the presence of an interaction between the two magnetic materials. It is interesting to note that the presence of such an interaction could also justify the suppression of the quantum tunneling of the magnetization in zero field[96] and the changes in the shape of the hysteresis loop of Fe_4 molecules when they are evaporated on LSMO. However, up to now a possible mechanism for this interaction has not been rationalized and a second hypothesis can also be formulated. This takes into account that Fe_4 molecules evaporated on LSMO can experience different local fields, depending on their distance from domain boundaries of the magnetic substrate. To have some hints on the width of the distribution of local fields that is necessary to suppress the step in zero field, the hysteresis loop has been simulated using a quantum transfer matrix approach(ref), taking into account a Gaussian distribution of local fields with half width of 0.2 T(see **Figure 5.29**). The zero field step is indeed suppressed although the shape of the hysteresis is not fully comparable to the observed one, especially close to saturation. In this rough modelization the width has been assumed to be constant over the entire field scan, which is not the case, because the distribution is expected to be larger when the manganite is not polarized but divided in domains, and to become narrower close to saturation. A more quantitative analysis would require additional information on the domains' structure of the LSMO substrate. Magnetic force microscopy and scanning hall-probes experiments are in program to clarify this aspect.

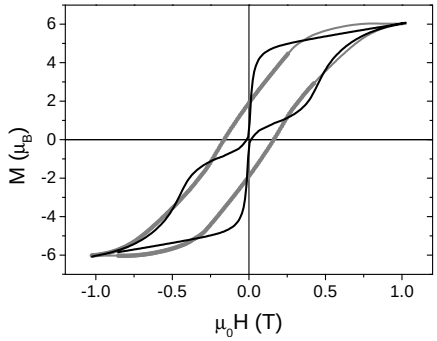

Figure 5.29: Calculated hysteresis loops for Fe_4 molecules with a quantum master matrix approach assuming developed in. In black is the hysteresis loop calculated for the magnetic field applied at 45° from the easy axis of magnetization (to mimic the absence of orientation of Fe_4 molecules in the evaporated monolayer). The spin Hamiltonian parameters are the same used in ref. In gray the same data have been convoluted assuming a distribution of local fields with center at H = 0 T and half width at half height of 0.2T.

5.6. Conclusions

The magnetic characterization of evaporated Fe_4Ph monolayer on gold and LSMO surfaces confirms that chemical and magnetic structure of Fe_4 core is preserved after thermal deposition. Nevertheless we have evidenced significant differences in the dynamics of the magnetization of deposited Fe_4 depending on the substrate. On one hand the tetranuclear iron (III) cluster evaporated on gold surface preserves a SMM behavior similar to the crystalline phase, while on the other hand the same compound evaporated on LSMO shows a suppression of the tunneling near the zero field. Further investigations are necessary to clarify the origin of this feature.

Chapter 6.

X-Ray studies of thermally evaporated Terbium Double-Decker films

6.1. Introduction

The results described in the previous chapter have demonstrated that the dynamics of magnetization of an evaporated Fe_4Ph monolayer can change with the substrate. In fact, while on gold surface we have observed the typical butterfly shape of the SMM hysteresis loop, on the magnetic substrate, LSMO, we have observed a remnant magnetization in zero field. These data have left open the question about the mechanism of the suppression of tunneling and have encouraged us to extend the investigation on other evaporable Single Molecule Magnets. The choice fell on $TbPc_2$ molecules because of their slow dynamics of magnetization due to a strong single ion anisotropy, as described in the first chapter. Moreover, very recently Stephanow end co-workers have confirmed the structural and magnetic characterization of a sub-monolayer deposit of $TbPc_2$ molecules with synchrotron-light techniques, confirming their intact deposition on surface[97] but revealing the absence of the of typical slow dynamics of the magnetization (the authors attributed this behaviour to the long time-scale of the X-ray based experiments).

We report in this chapter a synchrotron-based investigation of neutral $TbPc_2$ evaporated thick film on Al substrate and thin films on Au and LSMO surfaces, pointing out the slow relaxation of the magnetization and the opening of a butterfly hysteresis cycle at temperatures as high as 15 K for the thick film. Moreover, we found out that, once again, the magnetization of the thin film is influenced by the substrate, in contrast with the last results described by Stephanow end co-workers.[97]

6.2. Evaporation procedure

A 200 nm thick film of $TbPc_2$ compound was thermally evaporated in HV condition from a quartz crucible filled with 30 mg of microcrystalline powder and heated up in a Joule-heated Knudsen cell. The evaporation of the thick film was carried out in Genoa thanks to the collaboration with Prof. Buatier de Mongeot using the same setup employed for the evaporation of the thick film of Fe_4 SMMs. The K-type thermocouple connected to the crucible is able to measure the temperature profile during the warming up stage. As described in the previous chapter, the apparatus has been equipped with a cold cathode and a quartz crystal microbalance (QCM) placed in front of the source, thus allowing the real-time monitoring of both pressure variations and the thickness of the deposited film (**Figure 6.1**). QCM signal and pressure trends during evaporation coupled with a preliminary AFM thickness calibration have been used to monitor the deposition rate also for in situ experiments at synchrotron facilities.

The QCM signal reported increases at around 450 °C, clearly indicating the starting of compound sublimation; in this way we have obtained the good conditions for keeping a constant flux of molecules during the film growth. The pressure evolution in function of the crucible temperature during the warming up stage exhibits a prominent peak around 280 °C which can be presumably attributable to the emission of a volatile fraction of the compound not detected by the quartz microbalance. During the degassing procedure the sample holder was placed in a shadowed position inside the vacuum chamber, thus avoiding the risk of substrate contamination.

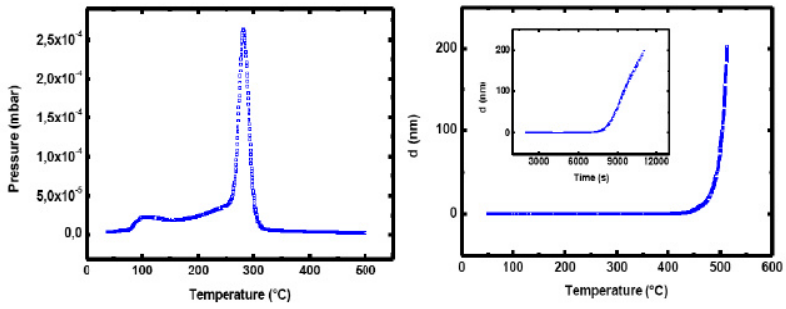

Figure 6.1: Left: evolution of the pressure measured by the vacuum gauge in function of the crucible temperature. Right: QCM detected thickness in function of the crucible temperature. In the inset thickness is plotted in function of time.

6.3. Chemical characterization on the evaporated $TbPc_2$thick and thin film

$TbPc_2$ micro-crystalline powder was evaporated at 500 °C on Al foil in a high vacuum chamber producing a 200 nm-thick film. The evaporation procedure was repeated on a polycrystalline Au substrate reducing the exposition time to the monolayer range. The high sensitivity of the ToF-SIMS technique allowed the chemical investigation of thin film in addition to the thick film. The positive ion spectrum of the evaporated film was compared with that of $TbPc_2$ powder pressed down on an Indium foil (**Fig. 6.2 c**). In the high mass region (*m/z* 600-1500) of both spectra, peaks at *m/z* 1183 and *m/z* 671 have been detected and have been assigned to the molecular ion (M^+) and the molecular ion fragment generated by loss of one Pc molecule ($[Tb+Pc]^+$), respectively. The similarities of the fragmentation pattern of the two spectra indicate that despite the thermal treatment the evaporated molecules retain their molecular integrity. Moreover the positive ions spectrum of the thin film coincides with that observed for the thick film with the additional signal at 1380 *m/z* attributable to the $[M+Au]^+$ ion, confirming the monolayer thickness of the deposit. Finally the peak at 1183 *m/z* assigned to the molecular ion (M^+) shows the isotopic distribution in complete agreement with the theoretical isotopic pattern expected for the $TbPc_2$ molecule (inset of **Figure 6.2**).

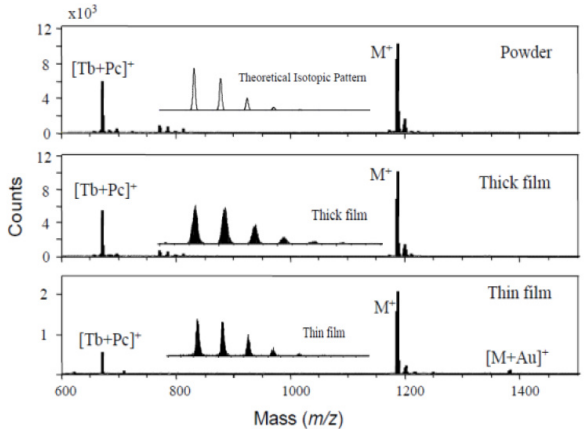

Figure 6.2: Positive ToF-SIMS spectra of $TbPc_2$ powder on In (*top*), $TbPc_2$ evaporated thick film on Al (*middle*) and $TbPc_2$ thin film evaporated on Au (*bottom*) in the mass region between 600-1500 *m/z*. In the inset of each panel ToF-SIMS of the evaporated thick and thin film in the molecular ion mass region and the theoretical isotopic distribution are represented.

The low mass region (*m/z* 0-600) spectra of both $TbPc_2$ powder on In and evaporated thick film on Al is characterized by the very intense Tb signal at *m/z* 159 and by the peaks attributed to the species $C_xH_yN_zTb^+$, $C_xN_yTb^+$, $C_xH_yN_z^+$, and $C_xH_y^+$. In addition, characteristic peaks are observed at *m/z* 2366 and *m/z* 1855 and assigned to $TbPc_2$ dimer (M_2^+) and the dimer fragment generated by loss of one Pc molecule ($[M+Tb+Pc]^+$). The presence of dimer and dimer fragment peaks does not necessarily indicate structural changes; in fact, ion beam-induced dimerization during static SIMS measurements has been reported in literature. (**Figure 6.3**)[98-99]

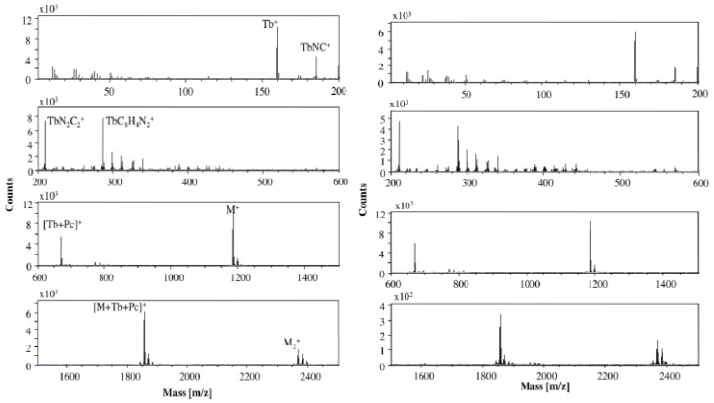

Figure 6.3: Positive ToF-SIMS spectra of the evaporated $TbPc_2$ film on Al (*left*) and $TbPc_2$ powder on In (*right*).

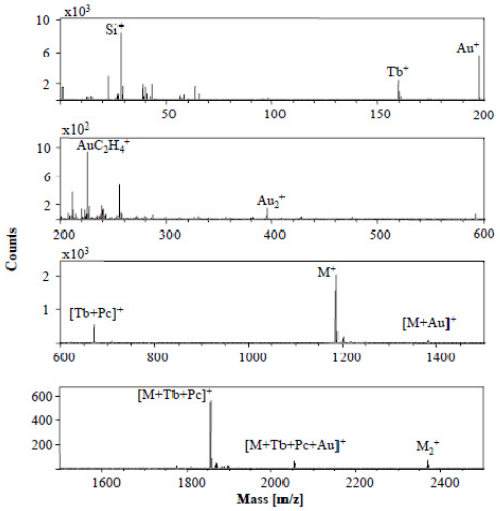

Figure 6.4: Positive ToF-SIMS spectra of the evaporated thin film of $TbPc_2$.

Evaporated thick film	Evaporated thin film	Powder	Fragment
Positive ions			
-	28	-	Si^+
159	159	159	Tb^+
185	185	185	$TbNC^+$
-	197	-	Au^+
199	199	199	$[TbN_2C]^+$
211	211	211	$[TbN_2C_2]^+$
-	225	-	$[AuC_2H_4]^+$
287	287	287	$[TbN_2C_8]^+$
-	394	-	$[Au_2]^+$
671	671	671	$[TbPc]^+$
1183	1183	1183	$[M]^+$
-	1380	-	$[M+Au]^+$
1855	1855	1855	$[M+Tb+Pc]^+$
2366	2366	2366	$[M_2]^+$
Negative Ions			
26	26	26	CN^-
-	197	-	Au^-
263	263	263	$[TbN_4C_4]^-$
1183	1183	1183	M^-
-	-	2366	$[M_2]^-$

Table 6.1. Characteristic peaks detected in the positive and negative ToF-SIMS spectra of $TbPc_2$ thick film evaporated on Al, $TbPc_2$ thin film evaporated on Au and powder on In and their assignments.

The ToF-SIMS spectrum of $TbPc_2$ thin film evaporated on Au (**Figure 6.4**) shows, besides the characteristic fragments detected in both $TbPc_2$ powder on In and evaporated film on Al, very intense signals generated by the gold substrate (*m/z* 0-600) and intense peaks attributed to the molecule-Au clusters (*m/z* 600-

2500). Compared to the positive ToF-SIMS spectra the negative ones (whose main peaks are listed in the **Table 6.1**) are less informative, they show only few peaks distinctive of $TbPc_2$ molecule reported in **Table 6.1**.

Moreover, the UV-VIS spectra carried out for the thick film were compared with those obtained from solution. Both spectra were characterized by the presence of the absorptions band at 667nm (Q band) typical of the neutral compound, at 448 nm (Radical band) and at 320 nm (Soret band) although a relevant broadening of the spectral features upon the evaporation is observed, confirming the data reported in literature.[15-16] (**Figure 6.5**).

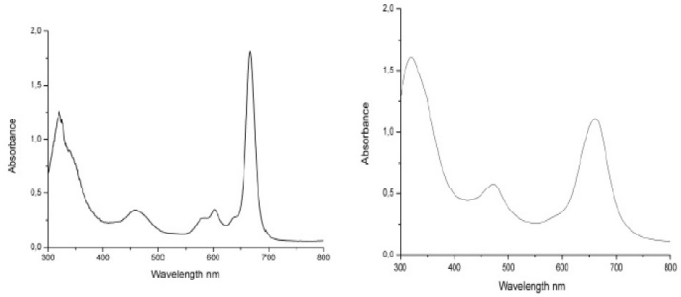

Figure 6.5: UV/Vis spectra of $TbPc_2$ solution in chloroform (left) and of an evaporated thick film $TbPc_2$ (right).

6.4. XMCD and XNLD studies on the evaporated $TbPc_2$ thick and thin film

Structural and magnetic information of the 200 nm thick film of $TbPc_2$ were obtained using variable temperature X-ray Absorption Spectroscopy (XAS) at ID08 beamline of the European Synchrotron Radiation Facility (ESRF) in Grenoble. The linear and circularly polarized XAS spectra recorded at $M_{4,5}$ edge of Tb are presented in **Figure 6.6 a** and **Figure 6.6 d**. The 3*d* to 4*f* transition is strongly dichroic and contains information about the orientation of the molecules and the magnetic moment of the 4*f* orbitals.[100] X-ray Natural Linear Dichroism, XNLD, was measured with the normal to the surface rotated by an angle $\theta = 45°$ from the photon propagation vector. The presence of a relevant dichroic signal (**Figure 6.6 a**) evidences that the molecules have a preferential orientation in the film. The same kind of investigation, performed on a thinner deposit of $TbPc_2$ of the order of a monolayer obtained by *in situ* evaporation on a clean Au(111) single crystal under UHV condition, lead up to different conclusions. In fact the dichroic signal of the XNLD spectra (**Figure 6.6 b**), carried out in the same

conditions of the thick film, has opposite sign and the intensity is twice larger than that obtained for the evaporated thick film.

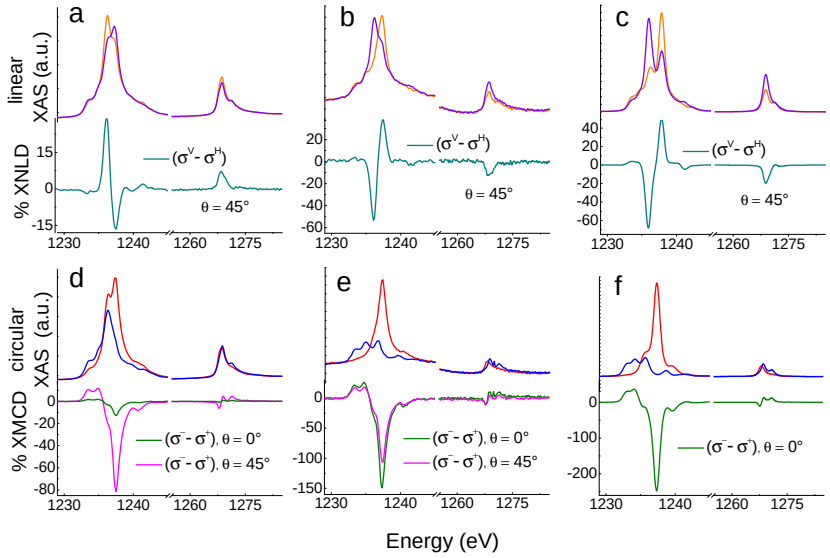

Figure 6.6:. Upper part: X-ray Absorption Spectra obtained with linearly polarized horizontal ,σ^H, and vertical, σ^V, light and the normalized dichroic component recorded at θ = 45°, T = 8 K and B = 0 T for the thick film (a) and the thin film (b) compared to the simulated spectra for |gs> = |J=6(L=3,S=3),M_J=±6> (c). Lower part: left, σ^+, and right, σ^-, circular light XAS and XMCD spectra recorded for the thick film (d) and thin film (e) at T = 8 K and B = 3 T, at two different angles θ between the propagation vector and the normal to the substrate. In f) the simulated spectra are reported for |gs> = |J=6(L=3,S=3),M_J=-6>. Dichroic percentage contribution are normalized to the isotropic signal at its maximum.

In order to clarify the relationship between the detected linear dichroism and the orientation of the molecules we performed Ligand Field Multiplet calculations,[88] LFM, following Goedkoop's seminal paper.[100] The spectra of the $M_{4,5}$ edges were obtained by calculating the electric dipole transitions between the $3d^{10}4f^8$ ground state configuration and the $3d^94f^9$ excited state configuration. For Tb^{3+} the ground state of the initial configuration was defined by the following quantum numbers : L = 3, S = 3 and J = 6, while the first excited state is at too high energy to mix into the ground state. The crystal field, as well as the external magnetic field, lifts the 13-fold degeneracy of the J = 6 ground state. With these

assumptions it was shown that the $M_{4,5}$ edges depend on geometrical factors and averaged values of the total kinetic momentum operator **J** acting on the ground state.[101]

Assuming that $TbPc_2$ molecules lie down on the surface with their pseudo-tetragonal *z* axis parallel to the normal of the substrate, the intensity of the XNLD signal can be written as $\sigma_V - \sigma_H = 1/2\ (\sigma_\perp - \sigma_{//})$, with $\sigma_{//}$ and $\sigma_\perp$ defined as the theoretical cross section measured with the polarization vector parallel and perpendicular to the *z* molecular axis. In the case of molecules standing on the surface with the *z* axes randomly distributed in the plane of the surface the relation $\sigma_V - \sigma_H = -1/4\ (\sigma_\perp - \sigma_{//})$ holds. Having observed a halved and reversed intensity of the linear dichroic contribution in the thick film we can deduce that the molecules are in the *standing* configuration, while they are lying down in the monolayer. These ordering effects are not unusual when flat molecules like phthalocyanines or porphyrins are evaporated, because the strong interactions with the substrate, as well as within the molecules, can affect the orientation and packing of the molecular deposit.[102] In particular in MPc systems the first layers grow with the molecule in *lying* position on noble metal surfaces because of strong molecule-surface interactions, while the molecules adopt a *standing* configuration in the case of rough surfaces and metal-oxide surfaces where molecule-molecule interactions are dominant.[102-105] Our hypothesis is confirmed by the good agreement between the structure of the XNLD signal observed for the thin film and the simulated one (see **Figure 6.6 c**) assuming lying down configuration. In addition, from a quantitative comparison between the experimental and calculated isotropic spectra and linear dichroic signals, one can determine the averaged value $\langle gs \mid (J_z)^2 \mid gs \rangle$ for the molecules, where *gs* stays for ground state. The extracted value of 30.5±1 (in units of $\hbar^2$) is close to the limiting value expected for a ground doublet corresponding to pure eigenstates of J_z with $M_J = \pm 6$, i. e. 36. This result was in agreement with the analysis performed by Spepanow[97] and confirms that the tetragonal symmetry axis of $TbPc_2$ is the easy axis of magnetization; however, small contributions from other eigenstates of J_z or from a non perfect organization of the molecules can be present.

Since $TbPc_2$ molecules are characterized by an easy magnetization axis lying perpendicular to the Pc macrocycles, the angular dependence of their magnetic response can also be exploited to confirm the XNLD data and investigate further the organization of the molecules on surface. The X-ray Magnetic Circular Dichroism, XMCD, was therefore measured. The XMCD signal of the evaporated thick film measured at 8 K with a 3 T magnetic field normal to the substrate is significantly weaker than the one measured at $\theta = 45°$, see **Figure 6.6 d**, indicating that Tb-double-decker molecules were arranged in the *standing* configuration with the easy magnetization axes of the molecules lying in the film

plane. On the contrary, in the thin film the strongest XMCD signal was measured with the photon beam normal to the film (see **Figure 6.6 e**) confirming that the evaporated molecules were arranged in *lying* configuration with the easy axis of magnetization perpendicular to the surface as already reported.[97] It is interesting to notice the weak XMCD signal has been detected at $\theta = 0°$ for the thick film, where the magnetic field is applied along the hard axis of magnetization of $TbPc_2$ molecules. The normalized intensity observed at $\theta = 45°$ is significantly smaller than that observed in the thin film at the same angle. In the former case, in fact, at $\theta = 45°$ there are still molecules with their hard plane parallel to the field due to the random orientation of the molecular axes in the plane of the thick film.

The shape of the XMCD spectra can be nicely reproduced by the LFM calculations introduced above, as shown in **Figure 6.6 f** for a lying down configuration. The normalized intensity observed at $T = 8$ K, $B = 3$ T, and $\theta = 0°$ for the thin film is found to correspond to ca. 60% of the saturation value, i. e. $T = 0$ K, expected for a ground state characterized by $M_J = -6$.

6.5. Dynamic of magnetization of the evaporated $TbPc_2$ thick and thin film

In order to characterize the SMM behavior of $TbPc_2$ in the two types of deposit, magnetic hysteresis loops at different temperatures and sample orientations have been obtained by monitoring the XMCD signal at M_5 edge as a function of the applied magnetic field swept at ca. 8 mT s^{-1}. The temperature dependence of the hysteresis loops obtained for the thick film sample (**Figure 6.7a**) shows that the evaporated film of $TbPc_2$ has a blocking temperature higher than most SMMs, although with a strong tunneling near zero field that cancels the remnant magnetization and gives a butterfly shape to the hysteresis. Nevertheless in the **Chapter 1** we have reported the magneto-optical investigations of frozen solutions of similar compounds[47] that show butterfly-shape hysteresis for the anionic and cationic derivatives, but not for the neutral one. As our UV-VIS spectra exclude that $TbPc_2$ has undergone a redox reaction during the evaporation, we ascribe the difference between the evaporated film and the frozen solution to packing effects of the molecules. Butterfly shape hysteresis loops observable up to $T = 15$ K indeed characterize also the pristine crystalline material.

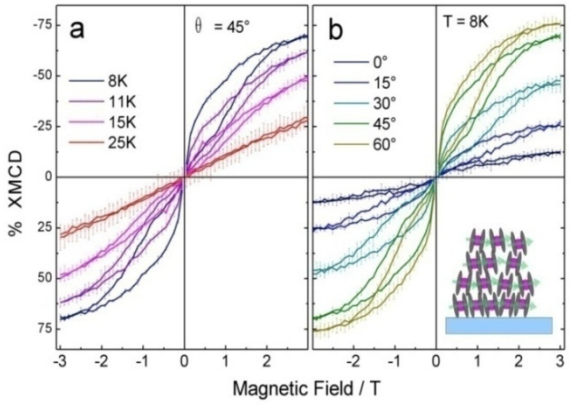

Figure 6.7: Temperature (a) and angle (b) dependence of the hysteresis loops obtained from the field dependence of the XMCD at 1237 eV expressed as percentage of the isotropic XAS. In the inset: scheme of the orientation of $TbPc_2$ molecules and their easy axes of magnetization in the thick film.

The angular dependence of the hysteresis (**Figure 6.7 b**) shows an enhancement of the magnetization on increasing the angle that the magnetic field forms with the normal to the surface, thus confirming our previous assumption about the orientation of the molecules. The thin film was investigated *in-situ* exactly under the same conditions adopted for the thicker film, and the hysteresis loop recorded at T = 8 K is shown in **Figure 6.8**. Interestingly, it was impossible to detect opening of the hysteresis cycle. To explore if slow dynamics of the magnetization is present at lower temperatures we repeated the characterization at the SIM beamline of the Swiss Light Source (SLS) in Villigen, Switzerland, using the TBT setup for lower temperature measurements.[93] A similar *in-situ* evaporation of a $TbPc_2$ thin film was this time carried out on a Au polycrystalline film as the lower temperature apparatus does not allow the single crystal treatment properly. The results we obtained at 4.5 and 2.0 K with normal incidence and sweeping rate of ca. 4 mT s^{-1} are also reported in **Figure 6.8**. The fast saturation at the lowest temperature confirms the preferential orientation of the molecules on surface in *lying* configuration in agreement with the XNLD and XMCD results reported above. Only a very small opening of the loop and at much lower temperatures compared to the thick film is observed.

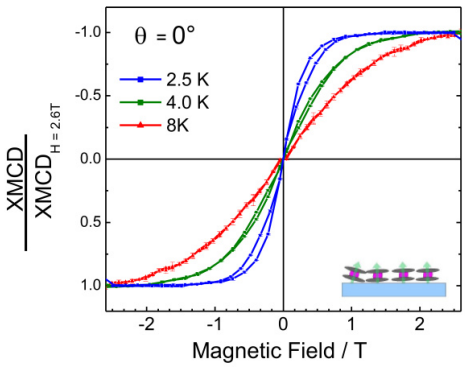

Figure 6.8 Temperature dependence of the hysteresis loops obtained from the field dependence of the XMCD signal at 1237 eV, normalized to the intensity observed at B = 2.6 T. In the inset scheme of the orientation of $TbPc_2$ molecules and their easy axes of magnetization in the thin film.

However, this data are clearly in contradiction with those reported by Stepanow that justify the absence of the opening of the hysteresis loop recorded at 8K with the long time required to measure the magnetization curve by XMCD.[97] At this stage we can exclude major structural modifications induced by the interaction with the surface, because ToF-SIMS analysis of the thin film revealed the presence of intact molecules. The identical XMCD lineshape in thick and thin films does not evidence any strong electronic effect induced by the surface proximity, as confirmed by the identical XMCD lineshape in thick and thin films. It must be stressed also that the lanthanide edge is not very sensitive to the environment and the occurrence of an interaction within the surface and the Pc ligands cannot be excluded. One could argue that the magnetic irreversibility at relatively high temperature is originated by intermolecular magnetic interactions promoted by the stacked arrangement of the molecules that is not present in the monolayer. This hypothesis seems to be confirmed by the evaporation of a thin film of $TbPc_2$ on LSMO surface where, as we will describe in the next paragraph, the molecules adopted a standing configuration.

6.6. XMCD studies on $TbPc_2$ evaporated thin film on LSMO substrates

The same kind of investigation was conducted on $TbPc_2$ SMM evaporated on LSMO substrate. Here we report the XAS/XMCD studies carried out on the $M_{4,5}$-Tb-Edge, omitting the $L_{2,3}$ Mn Edge of the manganite substrate, since the results were in good agreement with those reported in the previous chapter. As described

in the previous paragraph, the XNLD and XMCD evidence the presence of the orientation of the molecule on surface. The XNLD spectrum, (**Figure 6.9**) performed at a θ = 45°, clearly shows a significant dichroic signal with the same intensity, shape, and sign of the spectrum recorded for the thick film evaporated on Al. Moreover the XMCD signal measured at T = 8 K and the sample normal to the applied magnetic field is significantly weaker compared to those obtained rotating the sample of an angle θ = 45°. This behavior, comparable with the thick film sample, confirmed that the molecule on LSMO arrange in standing configuration with the easy axis of magnetization lying in the plane of the surface. This results are consistent with the data reported in literature that demonstrate that this kind of molecules adopt a *standing* configuration in the case of rough surfaces and metal-oxide, like the manganite substrate.[104-105]

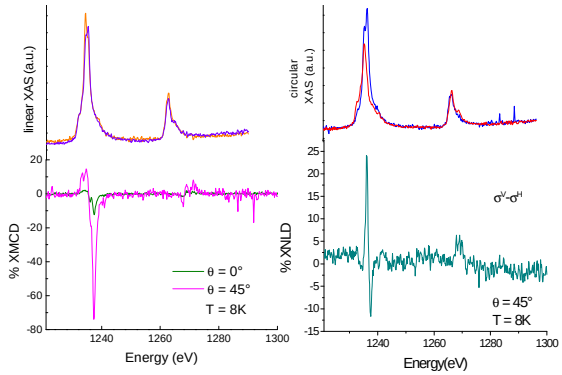

Figure 6.9: Left: X-ray Absorption Spectra obtained with linearly polarized horizontal, σ^H, and vertical, σ^V, light and the normalized dichroic component recorded at θ = 45°, T = 8 K and B = 0 T . Right: left, σ^+, and right, σ^-, circular light XAS and XMCD spectra recorded at T = 8 K and B = 3 T, at two different angles θ between the propagation vector and the normal to the substrate.

The hysteresis cycles recorded at both ESRF and SLS beamlines (where it is possible to detect the hysteresis loop at lower temperature) confirm the enhancement of the magnetization on increasing the angle (**Figure 6.10**). Besides that, the most interesting thing in this experiment was the opening of the hysteresis loop at 8 K that in the evaporated thin film on gold was closed. Moreover the opening of the hysteresis loop did not change by decreasing the temperature. In this case we could not exclude the influenced of the magnetic surface on $TbPc_2$ molecules, since Fe_4 SMM evaporated on manganite surface showed a drastic change of the dynamic of magnetization.

On the other hand, as underline above, the rough surfaces of the LSMO induce a standing configuration that promote a larger magnetic interactions between the molecules compared to the lying one.

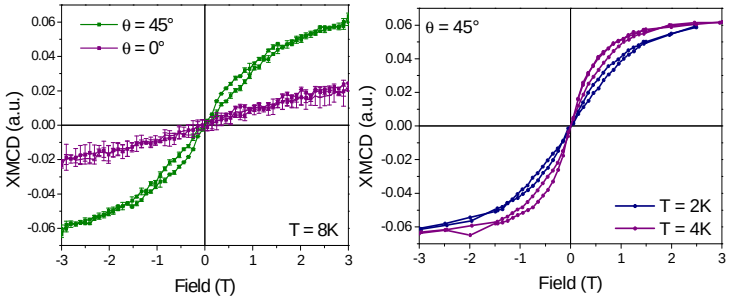

Figure 6.10: Left: angle and dependence of the hysteresis loops obtained from the field dependence of the XMCD at 1237 eV at T = 8K. Right: temperature dependence of the hysteresis loop recorded at θ = 45°.

6.7. Conclusions

To conclude, our magnetic characterization of evaporated $TbPc_2$ molecules carried out on both thick and thin evaporated films on gold and LSMO surfaces confirms that the double decker structure and the peculiar SMM behavior is retained after thermal deposition. Interestingly, this process induces an oriented arrangement of the molecules with the easy axis of magnetization lying in the plane or out of plane depending on the thickness of the film and on the morphology of the substrate. The spontaneous orientation of molecules, combined with the relatively high temperature opening of the hysteresis loop in the thick film, make Tb double-decker compounds promising candidates for the investigation of the interplay of SMM behavior and transport processes in molecular spintronic devices.

However, it is important to underline that, in contrast to tetranuclear iron(III) complexes that preserve unaltered SMM behavior on gold surface in the monolayer deposit,[81] $TbPc_2$ shows significant changes in the magnetization dynamics when the thickness is scaled down to the monolayer regime. On the other hand the opening of the hysteresis loop at higher temperature in the evaporated $TbPc_2$ monolayer sample on LSMO is preserved. Further investigations are necessary to clarify whether this is due to the influence of the magnetic surface or to the morphology and chemical nature of the manganite substrate that induce stronger molecule-molecule interactions compared to the gold surface.

Chapter 7.

Experimental Section

7.1. Thermal evaporation of Fe_4 SMMs thick film:

7.1.1. Chemical characterization with ToF-SIMS

ToF-SIMS analysis was carried out with a TRIFT III spectrometer (Physical Electronics, Chanhassen, MN, USA) equipped with a gold liquid-metal primary ion source. Positive and negative ion spectra were acquired with a pulsed, bunched 22 keV Au^+ primary ion beam, by rastering the ion beam over a 100 µm × 100 µm sample area and maintaining static SIMS conditions. In all spectra reported in this chapter, positive mass data were calibrated to CH_3^+ (*m/z* 15.023), $C_2H_3^+$ (*m/z* 27.023), $C_3H_5^+$ (*m/z* 41.039), and $C_{11}H_{19}O_2Fe^+$ (*m/z* 239.073, [Fe + dpm]$^+$); negative data were calibrated to CH^- (*m/z* 13.008), OH^- (*m/z* 17.003), C_2H^- (*m/z* 25.008), and $C_{11}H_{19}O_2^-$ (*m/z* 183.138, [dpm]$^-$), in the low mass region. A number of peaks of increasing mass were assigned and added to the calibration set for an accurate mass calibration. The mass resolution ($m/\Delta m$) was up to 10,000 depending on the sample.

7.1.2. Magnetic measurements

The frequency and temperature dependencies of the zero field ac susceptibility of Fe_4Ph film in the frequency range 500-25000 Hz have been measured with a home made susceptometer based on Oxford Instruments MAGLAB 2000 in Fe_4Ph evaporated film and with a Cryogenic S600 SQUID magnetometer for the other evaporated samples. Isothermal magnetization curves have been recorded using the SQUID magnetometer.

W-Band EPR spectra have been recorded using a Bruker E600 continuous-wave spectrometer with cylindrical cavity (TE_{001} mode) operating around 94 GHz, equipped with a split-coil superconducting magnet (Oxford Instruments) and a continuous-flow cryostat (Oxford CF 935), to achieve temperature variation. The sample of the evaporated film has been prepared scratching out the evaporated compound deposed on the kapton surface and blocking it in wax to avoid preferential orientation, as done with the bulk microcrystalline sample.

7.1.3. AFM profile analysis

The morphology of the evaporated films has been investigated ex-situ by means of AFM measurements using a Mobile S microscope (Nanosurf AG, Liestal, Switzerland) equipped with a PPP-NCRL-50 tip, (Nanosensor, Neuchatel, Switzerland) working with a scanning frequency of 1 Hz in non-contact mode. Operation of the AFM in contact mode was avoided in order to prevent the modification of the film morphology due to tip-surface interaction. The lateral correlation length of the film was determined from the full width at half maximum of the peak of the bidimensional autocorrelation and derived from numerical manipulation of the AFM images using the WSXM software. The lateral correlation length of the film was determined from the full width at half maximum of the peak of the bidimensional autocorrelation and derived from numerical manipulation of the AFM images using the WSXM software.

7.2. Thermal evaporation of a Fe_4Ph monolayer

7.2.1. The TBT endstation

The good results obtained at the SLS synchrotron have been achieved by exploiting the unique properties of the Trés Bas Temperature (TBT) end-station. This setup, was developed by the efforts of Dr. Philippe Sainctavit of Institut de Minèralogie et de Physique des Milieux Condensès (IMPMC), Universitè Pierre et Marie Curie, Paris and Dr. Jean-Paul Kappler of Institut de Physique et de Chimie des Matèriaux de Strasbourg (IPCMS). In addition to the standard features of a cryogenic endstation suited for studies in magnetism, TBT can be equipped with a ^{3}He-^{4}He dilution insert that allows cooling the sample to temperatures as low as 200 mK in ultra high vacuum and under the X-ray flux of a synchrotron beamline. We will now describe the basic features of this endstation. The advantages of a dilution based refrigeration is twofold: the extremely low temperature it can reach and the long time for which such

temperatures can be kept stable. A liquid ^{4}He bath in fact can be pumped to 0.1 mbar and will reach a temperature around 1 K. On the other hand, a pumped ^{3}He bath can reach temperatures as low as 0.3 K, but the limited supply and high cost of this cryogenic liquid make so that typical helium tank will be able to keep the temperature stable for no longer than a few hours. The ^{3}He-^{4}He dilution refrigerator overcomes both these issues; we will not cover here the theoretical principles of dilutions systems, details of which can be found in several specialized publications.[106] The system is made of two parts. An external shield containing liquid N_2 and an inner liquid ^{4}He tank. The whole dilution refrigerator is mounted on an independent vertical insert at the end of which the sample is attached. In a fully shielded chamber the cryostat can reach 30 mK on the sample; for XAS experiments however, the system must include windows that are transparent to the X-ray beam, thus reducing thermal insulation. In addition, experiments in magnetism require an applied field, so the dilution insert is surrounded by a 70 kOe superconducting split coil mounted on a six-flange cross in the ^{4}He cryostat. Applying of a magnetic induction though, induces eddy currents in the copper sample holder that also limit the minimum temperature. In normal conditions with x-ray photon flux on the sample and switching the magnetic induction, temperatures as low as 200 mK can be achieved, although thermal stabilization is hard to reach. At around 300 mK, the temperature can be constantly controlled over periods exceeding 20 h. Nitrogen and helium refills of the antecryostats must be carried out every 36 h and have no effect on the sample temperature. A constraint of this system is that the sample change has to be made with the mixing chamber at room temperature. This requires heating up the whole dilution refrigerator (mixing chamber and still), so that the process of warming up the sample, changing for a new one and cooling it down to 300 mK takes around 12 hours. This is quite incompatible with the strict scheduling of beamtime in synchrotron radiation facilities: for this reason a special sample holder able to mount four samples was designed and built for our experiments.

7.2.2. XMCD measurement protocol

A XMCD spectrum is defined as the difference between two spectra acquired with opposite photon polarizations on a sample whose spins are mainly oriented in one direction, or spectra recorded with the same photon helicity and opposite spin polarization of the sample. A standard set of spectra that are necessary to properly calculate one XMCD spectrum is made up of 8 acquisitions: four are carried out while applying a positive external field (i.e. polarizing the spins in one direction) and four in a negative field (spins polarized in the opposite direction.). For each of the two field directions, photon helicity is varied twice. When field

and photon helicity have the same sign (photon helicity is taken to be positive according to the right hand rule), the spectrum is called *positive* (σ^+); if field and photon polarization are of opposite sign, the spectrum is referred to as *negative* (σ^-). A typical acquisition cycle is carried out in the following order:

Photon helicity	Applied field	Resulting spectrum
+	+	σ^+
−	+	σ^-
−	+	σ^-
+	+	σ^+
+	−	σ^-
−	−	σ^+
−	−	σ^+
+	−	σ^-

Table 7.1: The complete XCMD acquisition pattern

The order of such sequence is important, since it is able to partially cancel the influence of parameters that vary regularly and in the same direction with time (i.e. drifting), since each type of spectrum is acquired twice and in such a way that drifting is canceled by averaging around a mean value; this principle is explained in **Figure 7.1**. This series of 8 spectra is the minimum repetitive unit to acquire a XMCD spectrum; however, when the signal is very weak, as in the case of monolayers, several acquisitions need to be carried out in order to increase signal to noise ratio to an acceptable level.

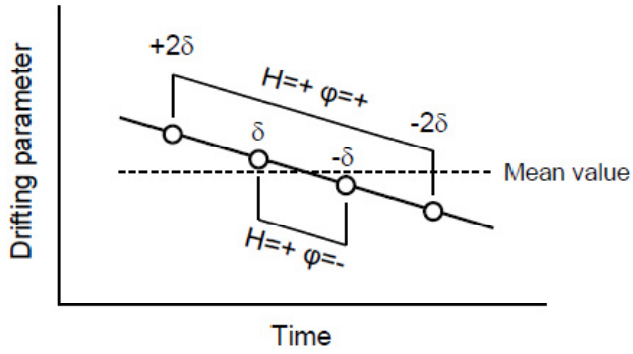

Figure 7.1: Schematic picture of error canceling through the acquisition sequence shown in Table

7.2.3. XNLD and XMCD measurement details

The experimental setup consists of a split coil superconducting magnet which provides magnetic fields up to 5 T in a direction parallel or antiparallel to the x-ray beam direction. The sample was mounted in a cold finger which allows to control the temperature between 8 and 300 K. The incidence angle of the x-rays can be changed rotating the sample along the vertical direction (polar rotation). All x-ray measurements are done under UHV conditions (~10^{-10} mbar). The beam line is equipped with two APPLE-2 type undulators, which produce linear and circular polarized x-rays with a polarization rate close to 100% in all cases. For the XLND and XMCD measurements only one undulator is normally used.

XLND and XMCD contributions were extracted by measuring the X-ray absorption spectra (XAS) around the absorption edge of a given element in the studied compound. These techniques provide element specific structural and magnetic information. XNLD explores the differences of the XAS when the probed atoms are in an anisotropic environment. In this case, the empty density of electronic states (DOS) are directional dependent and can be probed using linear polarized light in different geometries.[107] 94]

In the present work, vertical linear polarized x-ray always probed the in plane DOS. On the other hand, controlling the incidence angle of the horizontally polarized x-rays on the sample, one can also probe the in plane (normal incidence) or the out of plane DOS (grazing incidence, $\theta = 45°$). Here we define the XNLD signal as the difference between the XAS obtained using vertical and horizontal polarized x-rays (σ_V-σ_H). Similarly, the XMCD signal is defined as the difference between the XAS obtained using left and right circularly polarized

x-rays. In our case the individual spectra were measured applying a magnetic field of 3 T along the beam direction. To minimize systematic errors, a suitable spectra sequence was used changing both the xray polarization and the magnetic field direction. The resulting XMCD difference intensity ($\sigma^- - \sigma^+$) is proportional to the magnetic moment of the probed element projected on the x-ray incidence direction.

7.2.4. Preparation of substrates

As described in the previous section we are able to *in-situ* clean the substrate for synchrotron experiments only at ESRF however we employed also other cleaning procedures for the *ex-situ* characterizations. In this paragraph we will describe the cleaning and the preparation procedures of all the substrates employed in this thesis work.

Gold film on Mica. This substrate was clean by the flame annealing process that consists in repeatedly heating to incandescence the substrate's surface with the flame for a short time (in the order of seconds). The gold surfaces thus obtained feature extended terraces of the Au(111) face. In addition to the morphological reconstruction, flame annealing also works excellently as a surface cleaning technique, as organic impurities adsorbed on the surface of gold are decomposed by the high temperature treatment, leaving a layer of gold atoms on the surface. Traces of residual contaminants are removed by subsequent ethanol washing.

Gold (111) and Cu(100) single crystals. The sputtering is a procedure used to remove the contamination from the surface by bombarding a target with energetic ions (Ar^+). The subsequent annealing procedure is useful to expel from the surface the impurity and to flatten the surface made rough by the sputtering procedure. Gold(111) and Copper(100) mono-crystals were cleaned by several sputtering and annealing cycles depending on the dirtiness of the substrates. Usually in the first cycle was applied 1keV of energy for 30-60 minutes and the second one an energy of 0.5 KeV for 15-30 minutes. The base pressure during the sputtering cycles was ca. 4×10^{-6}mbar in both case. After each sputtering we annealed the crystals by heating the surface for 5-10 minutes at 650°C in the case of Au(111) monocrystals and at 540°C in the case of Cu(100) single crystals.

LSMO. A series of 20 nm thick $La_{0.7}Sr_{0.3}MnO_3$, LSMO, films were deposited on matching $NdGaO_3$ substrates by using the pulsed electron deposition in the pulsed plasma deposition configuration. The procedure was performed *ex-situ* in the laboratory of Dr. Valentin Dediu at the ISMN-CNR of Bologna. During the

deposition, the substrates were heated to 800–850 °C, while the oxygen pressure was kept at 10^{-2} mbar. This procedure ensures high quality epitaxial LSMO films with high Curie temperature (T_C = 320–340 K, depending on film thicknesses) and a resistivity lower than 10 mΩcm at 300 K. The LSMO substrates (5×10 mm^2) used at ESRF were annealed in UHV and for 20 minutes at 250 °C. Before using the substrate for the evaporation of Fe_4Ph we investigate the electronic and the magnetic structure of the LSMO by XAS/XMCD. These analysis was carried out in the ESRF Synchrotron in order to understand if the annealing procedure apart from removing the carbon contamination on the surface preserves the chemical structures and the oxygen stoichiometry of the LSMO.

7.2.5. STM imagines of Fe_4Ph evaporated monolayer:

The morphology of the evaporated Fe_4Ph monolayer on Gold surface was conducted by a NT-MDT P47-pro instrument working with a custom made low current head and using 90:10 Pt/Ir tips obtained by mechanical sharpening.

7.3. Thermal evaporation of a thick and thin film of $TbPc_2$ SMM on different surfaces

7.3.1. Synthesis of $TbPc_2$ molecules.

The neutral Bis(phthalocyaninato)Terbium complex of formula $Tb(C_{32}H_{16}N_8)_2 \cdot CH_2Cl_2$, here abbreviated in $TbPc_2$, was synthesized according to literature procedures.[44, 108] In particular the reaction was carried out under aerobic conditions. Unless otherwise stated all reagents were purchased from Sigma-Aldrich and were used as received without further purification. A mixture of 1,2-dicyanobenzene (15,6 mmol), $Tb(OAC)_3 \cdot 4H_2O$ (1 mmol) and 1,8-diazabicyclo[5,4,0]undec-7-ene (DBU) (8 mmol) in 50 mL of 1-hexanol was refluxed for 1.5 days. The solution was cooled to room temperature and then filtered. The resulting dark purple crystalline precipitate was washed successively with acetic anhydride, cold acetone, n-pentane and then dried in air. The purple crystalline precipitate was extracted with several portions of chloroform, concentrated under vacuum with a rotary evaporator and purified using column chromatography (Merck Silica gel 60) of silica gel. A 2% CH_3OH / CH_2Cl_2 was used as eluent. X-ray quality needle-shaped crystals were obtained by slow evaporation of 2% CH_3OH / CH_2Cl_2 solution and a crystal analyzed on Oxford Diffraction Xcalibur 3 single crystal diffractometer at room temperature was found to have the following orthorhombic unit cell parameters: a = 28.36(9) Å,

b = 23.08(4) Å, c = 8.09(5) Å. These values indicate that $TbPc_2 \cdot CH_2Cl_2$ is isomorphous to the previously reported $LuPc_2 \cdot CH_2Cl_2$, which has a = 28.249(2) Å, b = 22.877(8) Å, and c = 8.050(4) Å.[44]

7.3.2. Preparation of substrates.

The deposition of a thick film of $TbPc_2$ has been simultaneously performed on two different substrates. A 0.1 mm thick Al foil with a purity of 99.99 % (ALFA AESAR GmbH & Co KG, Germany) was chosen for a ToF-SIMS characterization and for *ex situ* XMCD and XNLD measurements. Transparency and flatness of a fused silica substrate (roughness RMS < 0.5 nm in the several microns range) have been exploited respectively for UV-VIS spectroscopy and for Atomic Force Microscopy (AFM) film thickness check.

The Au(111) single crystal, the Au film evaporated on mica and the LSMO substrates were used for the *in situ* evaporation at the ESRF and SLS Synchrotrons radiation.

7.3.3. AFM profile analysis.

AFM profile analysis has been performed using a Mobile S microscope (Nanosurf AG, Liestal, Switzerland) equipped with a PPP-NCRL-50 tip (Nanosensor, Neuchatel, Switzerland) working with a scanning frequency of 0.5 Hz in tapping mode. The image reported in **Figure 7.2** describes the scratch on that allowed us to estimate that the thickness of the film was around 200 nm thus allowing to calibrate the microbalance signal.

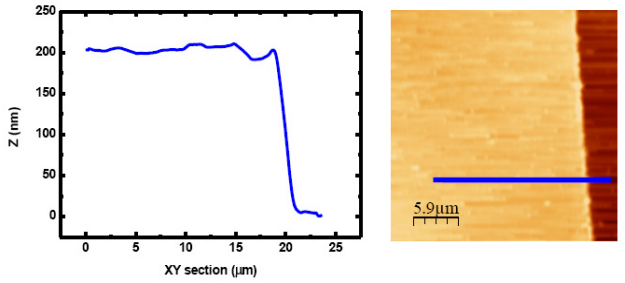

Figure 7.2: Line profile of an AFM topography scratched film deposited on the fused silica substrate.

7.3.4. Chemical characterization.

ToF-SIMS analysis was carried out on $TbPc_2$ thick film evaporated on Al substrate with the set up described in the Chapter 3. Positive mass spectra were calibrated to CH_3^+ (*m/z* 15.023), $C_2H_3^+$ (*m/z* 27.023), $C_3H_5^+$ (*m/z* 41.039), and $CNTb^+$ (*m/z* 184.929); negative data were calibrated to CH^- (*m/z* 13.008), OH^- (*m/z* 17.003), C_2H^- (*m/z* 25.008), and $C_4N_4Tb^-$ (*m/z* 262.938), in the low mass region. A number of peaks of increasing mass were assigned and added to the calibration set for an accurate mass calibration. Mass accuracy was better than 10 ppm. The mass resolution ($m/\Delta m$) was up to 7,000 in $TbPc_2$ film spectra.

The UV/visible spectra on solution were recorded by a Shimadzu 2101 PC Spectrophotometer with 10 mm quartz Suprasil® cells, in chloroform, while the spectra on the evaporated film on quartz substrate were recorded by a JASCO V-670 in range of 300-800 nm.

7.3.5. Ligand Field Multiplet analysis

The X-ray Absorption Spectra of the $M_{4,5}$ edges of Tb^{3+} have been calculated within the Ligand Field Multiplet approach with the Slater integrals associated to the Coulomb repulsions scaled down to 80% of the atomic values and the spin-orbit parameters shell ζ_{3d}=13.368 eV for the 3*d* and ζ_{4f}= 0.221 eV for the 4*f* shell. Further details on the used method can be found in reference. [101]

Conclusions

During this thesis work we have studied the preparation and characterization of films deposited by thermal evaporation technique in UHV. The principal results consist in the proof of evaporability of the polynuclear SMM, Fe_4Ph, in UHV condition allowing to extend the investigation to reactive surfaces, e.g. ferromagnetic metals, and to work in clean conditions as usually required for the development and fabrication of spin valve devices that are based on ferromagnetic electrodes like metallic Co and LSMO. For this reason it has been important to investigate the magnetic properties of Fe_4 SMM on these substrates and to verify if the latter can influence the chemical and magnetic properties of the evaporated molecules. First of all a careful preliminary study of the magnetic properties of the thick film allowed us to verify that the heating process did not lead to a chemical decomposition of the deposited molecules or to a change of their magnetic properties.

The good results obtained for the thermally evaporated Fe_4Ph compound allowed us to deepen the investigation by studing monolayers ,in order to investigate the interaction between the molecules and the substrate. The study of the magnetic properties of Fe_4ph monolayer was conducted thanks to the experience gained in synchrotron radiation facility with the XAS/XMCD technique. The analysis on the intensities and the shape of the dichroic spectrum confirmed the persistence of the electronic structure of the pristine molecular system and the antiferromagnetic coupling between the central ion Fe^{3+} and three peripheral Fe^{3+} ions on Au (111), Cu (100) and LSMO surfaces. Nevertheless the investigations performed on the dynamic of the magnetization carried out by using the ^3He-^4He dilution cryostat able to reach temperatures of the order of few hundred of mK, showed a significant differences in the observed dynamics of the magnetization of deposited Fe_4, depending by the substrate. In fact on one hand

the tetranuclear iron (III) cluster evaporated on gold surface preserves a SMM behavior similar to the crystalline phase, while on the other hand the same compound evaporated on LSMO shows the suppression of the tunneling near zero

field. In addition also the time decays experiments clearly indicated an influence of the LSMO substrate on the dynamics of the magnetization of the evaporated Fe_4Ph. This influence becomes important and more visible when the sample is not orthogonal to the magnetic field, i.e. when the field orientation is closer to the *in plane* magnetization of the LSMO substrate. The suppression of the zero-field tunneling could represent a novel proximity effect of great relevance to increase the blocking temperature of SMM. At the moment, however, we cannot exclude a less exotic origin, i. e. Fe_4 molecules evaporated on LSMO experiences different local fields caused by the domains of the magnetic substrate. Further experiments are needed to shed light on the origin of this unprecedented phenomenon.

Another information that we have obtained by the analysis of the hysteresis loop as function of the angle was a lower orientation of the molecules on the LSMO surface respect to the gold one, probably caused by the increased roughness of the manganite substrate. For this reason we decided to evaporate molecules characterized by a stronger magnetic anisotropy than Fe_4 compounds such as the double decker complex $TbPc_2$, in order to amplify the effect induced by the substrate on the magnetic hysteresis loop. Interestingly, in this case the evaporation process induces an oriented arrangement of the molecules caused by the flatness of the phatolocianine macrocycle, with the easy axis of magnetization lying in the plane or out of plane depending on the thickness of the film and on the morphology of the substrate. The XMCD, XNLD and the hysteresis loop measures as function of the angle showed that $TbPc_2$ adopts a standing configuration when they are evaporated on a metal oxide substrate as the manganite or deposited as thick films, while adopt a lying configuration when the evaporation is performed on a metallic substrate like gold.

Finally it is interesting to compare the magnetic behavior of the two SMMs deposited on surface. In fact, in contrast to tetranuclear iron(III) complexes that preserve unaltered SMM behavior on gold surface, the monolayer deposit of $TbPc_2$ shows significant changes in the dynamics of magnetization when the thickness is scaled down to the monolayer regime as observed by the absence of the hysteresis loop. This observation points out the most robust character of the the SMMs behavior in rationally designed polynuclear clusters. On the other hand the LSMO substrate seems to have a significant influence on both molecules. In fact also the evaporated $TbPc_2$ SMM on manganite surface showed a different

behavior respect the one on gold surface as demonstrated by the opening of the hysteresis loop at higher temperature. Further investigations are necessary to clarify whether this is due to the influence of the magnetic surface or to the morphology and chemical nature of the manganite substrate that could induce stronger molecule-molecule interactions compared to the gold surface.

We can then conclude that our investigations on evaporable of SMMs in UHV condition have provided important findings to develop multilayered nanostructures combining metallic or magnetic layers with SMMs films. Moreover, the synchrotron radiations and in particular the XMCD and XNLD experiments coupled to TBT end station able to reach sub-Kelvin temperature, are confirmed to be a powerful tool to investigate the influence of the substrates on the monolayer deposits of the molecules.

References

[1] A. Caneschi, D. Gatteschi, R. Sessoli, A.-L. Barra, L. C. Brunel, M. Guillot, *J. Am. Chem. Soc.* **1991**, *113*, 5873.

[2] R. Sessoli, H. L. Tsai, A. R. Schake, S. Wang, J. B. Vincent, K. Folting, D. Gatteschi, G. Christou, D. N. Hendrickson, *J. Am. Chem. Soc.* **1993**, *115*, 1804.

[3] D. Gatteschi, R. Sessoli, J. Villain, in *Molecular Nanomagnets*, Oxford University Press, Oxford, UK, **2006**.

[4] S. M. Holmes, G. S. Girolami, *J. Am. Chem. Soc.* **1999**, *121*, 5593.

[5] D. Gatteschi, R. Sessoli, *Angew. Chem. Int. Ed.* **2003**, *42*, 268.

[6] S. Sanvito, *Nat. Mater.* **2007**, *6*, 803.

[7] A. Cornia, A. F. Costantino, L. Zobbi, A. Caneschi, D. Gatteschi, M. Mannini, R. Sessoli, *Struct. Bonding* **2006**, *122*, 133.

[8] M. A. Arrio, P. Sainctavit, C. C. D. Moulin, C. Brouder, F. M. F. Degroot, T. Mallah, M. Verdaguer, *Physica B-Cond. Mat.* **1995**, *209*, 775.

[9] M. A. Arrio, P. Sainctavit, C. C. D. Moulin, C. Brouder,F. M. F. Degroot, T. Mallah, M. Verdaguer, M. *J. Phys. Chem.* **1996**, *100*, 4679.

[10] D. Gambardella, D. H., K. Maiti, M. C. Malagoli, W. Eberhardt, K. Kern, C. Carbone, *Nature* **2002**, *416*, 301.

[11] V. Corradini, R. Biagi, U. Del Pennino, V. De Renzi, A. Gambardella, M. Affronte, C. A. Muryn, G. A. Timco, R. E. P. Winpenny, *Inorg. Chem.* **2007**, *46*, 4937.

[12] H. Wende, M. Bernien, J. Luo, C. Sorg, N. Ponpandian, J. Kurde, J. Miguel, M. Piantek, X. Xu, P. Eckhold, W. Kuch, K. Baberschke, P. M.

Panchmatia, B. Sanyal, P. M. Oppeneer, O. Eriksson, *Nat. Mater.* **2007**, *6*, 516.

[13] N. Ishikawa, M. Sugita, T. Ishikawa, S. Koshihara, Y. Kaizu, *J. Am. Chem. Soc.* **2003**, *125*, 8694.

[14] K. Kambe, *J. Phys. Soc. Jpn.* **1950**, *5*, 48.

[15] J. Van Slageren, P. Rosa, A. Caneschi, R. Sessoli, H. Casellas, Y. V. Rakitin, L. Cianchi, F. D. Giallo, G. Spina, A. Bino, A. L. Barra, T. Guidi, S. Carretta, R. Caciuffo, *Phys. Rev. B* **2006**, *73*.

[16] A. L. Barra, A. Caneschi, A. Cornia, F. F. De Biani, D. Gatteschi, C. Sangregorio, R. Sessoli, L. Sorace, *J. Am. Chem. Soc.* **1999**, *121*, 5302.

[17] A. Cornia, A. C. Fabretti, P. Garrisi, C. Mortalo, D. Bonacchi, D. Gatteschi, R. Sessoli, L. Sorace, W. Wernsdorfer, A. L. Barra, *Ang. Chem. Int. Ed.* **2004**, *43*, 1136.

[18] R. W. Saalfrank, A. Scheurer, I. Bernt, F. W. Heinemann, A. V. Postnikov, V. Schunemann, A. X. Trautwein, M. S. Alam, H. Rupp, P. Muller, *Dalton Trans.* **2006**, 2865.

[19] A. Bencini, D. Gatteschi, *Transition Metal Chemistry* **1982**, *8*, 1.

[20] D. Gatteschi, A. L. Barra, A. Caneschi, A. Cornia, R. Sessoli, L. Sorace, *Coord. Chem. Rev.* **2006**, *250*, 1514.

[21] A. L. Barra, A. Caneschi, D. Gatteschi, R. Sessoli, *J.Magn. Magn. Mater.* **1998**, *177*, 709.

[22] R. Caciuffo, G. Amoretti, A. Murani, R. Sessoli, A. Caneschi, D. Gatteschi, *Phys. Rev. Lett.* **1998**, *81*, 4744.

[23] A. L. Barra, D. Gatteschi, R. Sessoli, G. L. Abbati, A. Cornia, A. C. Fabretti, M. G. Uytterhoeven, *Angew. Chem. Int. Ed.* **1997**, *36*, 2329.

[24] D. P. Goldberg, J. Telser, J. Krzystek, A. G. Montalban, L. C. Brunel, A. G. M. Barrett, B. M. Hoffman, *J. Am. Chem. Soc.* **1997**, *119*, 8722.

[25] A. Bencini, I. Ciofini, M. G. Uytterhoeven, *Inorg Chim. Acta* **1998**, *274*, 90.

[26] L. F. Chibotaru, L. Ungur, A. Soncini, *Angew. Chem. Int. Ed.* **2008**, *47*, 4126.

[27] A. Bencini, D. Gatteschi, Springer-Verlag, Berlin, **1990**.

[28] O. Waldmann, *Inorg. Chem.* **2007**, *46*, 10035.

[29] R. Sessoli, D. Gatteschi, A. Caneschi, M. A. Novak, *Nature* **1993**, *365*, 141.

[30] A. Caneschi, T. Ohm, C. Paulsen, D. Rovai, C. Sangregorio, R. Sessoli, *J. Magn. Magn. Mater.* **1998**, *177*, 1330.

[31] S. Accorsi, A. L. Barra, A. Caneschi, G. Chastanet, A. Cornia, A. C. Fabretti, D. Gatteschi, C. Mortalo, E. Olivieri, F. Parenti, P. Rosa, R. Sessoli, L. Sorace, W. Wernsdorfer, L. Zobbi, *J. Am. Chem. Soc.* **2006**, *128*, 4742.

[32] M. A. Novak, R. Sessoli, in *Quantum Tunneling of Magnetization - QTM'94*, Kluwer, Dordrecht, **1995**, pp. 171.

[33] J. R. Friedman, M. P. Sarachik, J. Tejada, R. Ziolo, *Phys. Rev. Lett.* **1996**, *76*, 3830.

[34] L. Thomas, F. Lionti, R. Ballou, D. Gatteschi, R. Sessoli, B. Barbara, *Nature* **1996**, *383*, 145.

[35] W. Wernsdorfer, R. Sessoli, *Science* **1999**, *284*, 133.

[36] S. Hill, R. S. Edwards, N. Aliaga-Alcalde, G. Christou, *Science* **2003**, *302*, 1015.

[37] R. W. Saalfrank, I. Bernt, M. M. Chowdhry, F. Hampel, G. B. M. Vaughan, *Chem. Eur. J.* **2001**, *7*, 2765.

[38] A. Bouwen, A. Caneschi, D. Gatteschi, E. Goovaerts, D. Schoemaker, L. Sorace, M. Stefan, *J. Phys. Chem. B* **2001**, *105*, 2658.

[39] A. Cornia, A. C. Fabretti,P. Garrisi, C. Mortalò, D. Bonacchi, R. Sessoli,L. Sorace, A. L. Barra, W. Wernsdorfer, *J. Magn. Magn. Mater.* **2004**, *272*, e749.

[40] K. S. Cole, C. R. H., *J. Chem. Phys.* **1941**, *9*, 341.

[41] C. Dekker, A. F. M. Arts, H. W. Wijn, A. J. van Duyneveldt, J. A. Mydosh, *Phys. Rev. B* **1989**, *40*, 11243.

[42] K. S. Cole, R. H. Cole, *J. Chem. Phys.* **1941**, *9*, 341.

[43] N. Ishikawa, M. Sugita, T. Okubo, N. Tanaka, T. Lino, Y. Kaizu, *Inorg. Chem.* **2003**, *42*, 2440.

[44] K. Katoh, Y. Yoshida, M. Yamashita, H. Miyasaka, B. K. Breedlove, T. Kajiwara, S. Takaishi, N. Ishikawa, H. Isshiki, Y. F. Zhang, T. Komeda, M. Yamagishi, J. Takeya, *J. Am. Chem. Soc.* **2009**, *131*, 9967.

[45] N. Ishikawa, *Polyhedron* **2007**, *26*, 2147.

[46] L. Vitali, S. Fabris, A. M. Conte, S. Brink, M. Ruben, S. Baroni, K. Kern, *Nano Lett.* **2008**, *8*, 3364.

[47] M. Gonidec, E. S. Davies, J. Mcmaster, D. B. Amabilino, J. Veciana, *J. Am. Chem. Soc.* **2010**, *132*, 1756.

[48] N. Ishikawa, M. Sugita, N. Tanaka, T. Ishikawa, S. Y. Koshihara, Y. Kaizu, *Inorg. Chem.* **2004**, *43*, 5498.

[49] N. Ishikawa, M. Sugita, T. Ishikawa, S. Koshihara, Y. Kaizu, *J.Phys. Chem. B* **2004**, *108*, 11265.

[50] A. Cornia, A. C. Fabretti, M. Pacchioni, L. Zobbi, D. Bonacchi, A. Caneschi, D. Gatteschi, R. Biagi, U. Del Pennino, V. De Renzi, L. Gurevich, H. S. J. Van Der Zant, *Angew. Chem. Int. Ed.* **2003**, *42*, 1645.

[51] M. Mannini, D. Bonacchi, L. Zobbi, F. M. Piras, E. A. Speets, A. Caneschi, A. Cornia, A. Magnani, B. J. Ravoo, D. N. Reinhoudt, R. Sessoli, D. Gatteschi, *Nano Lett.* **2005**, *5*, 1435.

[52] M. Cavallini, M. Facchini, C. Albonetti, F. Biscarini, *Phys. Chem. Chem. Phys.* **2008**, *10*, 784.

[53] G. H. Kim, T. S. Kim, *Phys. Rev. Lett.* **2004**, *92*, 137203

[54] D. Ruiz-Molina, M. Mas-Torrent, J. Gomez, A. I. Balana, N. Domingo, J. Tejada, M. T. Martinez, C. Rovira, J. Veciana, *Adv. Mater.* **2003**, *15*, 42.

[55] A. Ulman, *Chem. Rev.* **1996**, *96*, 1533.

[56] Y. N. Xia, G. M. Whitesides, *Angew. Chem. Int. Ed.* **1998**, *37*, 551.

[57] M. Ruben, *Angew. Chem. Int. Ed.* **2005**, *44*, 1594.

[58] P. Gambardella, S. Stepanow, A. Dmitriev, J. Honolka, F. M. F. De Groot, M. Lingenfelder, S. Sen Gupta, D. D. Sarma, P. Bencok, S. Stanescu, S. Clair, S. Pons, N. Lin, A. P. Seitsonen, H. Brune, J. V. Barth, K. Kern, *Nat. Mater.* **2009**, *8*, 189.

[59] J. Means, V. Meenakshi, R. V. A. Srivastava, W. Teizer, A. Kolomenskii, H. A. Schuessler, H. Zhao, K. R. Dunbar, *J. Magn. Magn. Mater.* **2004**, *284*, 215.

[60] V. Meenakshi, W. Teizer, D. G. Naugle, H. Zhao, K. R. Dunbar, *Solid State Commun.* **2004**, *132*, 471.

[61] R. Moroni, R. Buzio, A. Chincarini, U. Valbusa, F. B. De Mongeot, L. Bogani, A. Caneschi, R. Sessoli, L. Cavigli, M. Gurioli, *J. Mater. Chem.* **2008**, *18*, 109.

[62] D. Gatteschi, A. Cornia, M. Mannini, R. Sessoli, *Inorg. Chem.* **2009**, *48*, 3408.

[63] T. A. Jung, R. R. Schlittler, J. K. Gimzewski, H. Tang, C. Joachim, *Science* **1996**, *271*, 181.

[64] J. Gomez-Segura, I. Diez-Perez, N. Ishikawa, M. Nakano, J. Veciana, D. Ruiz-Molina, *Chem. Commun.* **2006**, 2866.

[65] F. Pineider, M. Mannini, R. Sessoli, A. Caneschi, D. Barreca, L. Armelao, A. Cornia, E. Tondello, D. Gatteschit, *Langmuir* **2007**, *23*, 11836.

[66] L. Gorini PhD thesis, Dottorato in Scienze dei Materiali, University of Florence, **2007**

[67] M. Mannini, F. Pineider, P. Sainctavit, L. Joly, A. Fraile-Rodriguez, M. A. Arrio, C. Cartier-dit-Moulin, W. Wernsdorfer, A. Cornia, D. Gatteschi, R. Sessoli, *Adv. Mater.* **2009**, *21*, 167.

[68] M. Mannini, F. Pineider, C. Danieli, F. Totti, L. Sorace, P. Sainctavit, M.-A. Arrio, E. Otero, L. Joly, J. C. Cezar, A. Cornia, R. Sessoli, *Nature* **2010**, *468*, 417.

[69] F. Pineider PhD thesis, Dottorato in Scienze Chimiche, University of Florence, **2008**

[70] N. V. Gérbeléu, Y. T. Strucholov, G. A. Timco, A. S. Batsanov, K. M. Indrichan, G. A. Popovich, *Dokl. Akad. Nauk SSSR* **1990**, *313*, 1459

[71] I. G. Fomina, G. G. Aleksandrov, Z. V. Dobrokhotova, O. Y. Proshenkina, M. A. Kiskin, Y. A. Velikodnyi, V. N. Ikorskii, V. M. Novotortsev, I. L. Eremenko, *Russ. Chem. Bull.* **2006**, *55*, 1909.

[72] Z. V. Dobrokhotova, I. G. Fomina, M. A. Kiskin, A. A. Sidorov, V. M. Novotortsev, I. L. Eremenko, *Russ. Chem. Bull.* **2006**, *55*, 256.

[73] F. Pineider, M. Mannini, C. Danieli, L. Armelao, F. M. Piras, A. Magnani, A. Cornia, R. Sessoli, *J. Mat. Chem.* **2010**, *20*, 187.

[74] F. Mott, *Proc. Roy. Soc. A* **1936**, *153*, 699

[75] P. Grünberg, R. Schreiber, Y. Young, M.B. Brodsky, H. Sowers, *Phys. Rev. Lett.* **1986**, *57*, 2442.

[76] M. N. Baibich, J. M. Broto, A. Fert, F. Nguyen Van Dau, F. Petroff, P. Eitenne, G. Creuzet, A. Friederich, J. Chazelas, in *Phys. Rev. Lett.* **1988**, *61*, 2472.

[77] G. Binasch, P. Grünberg, F. Saurenbach, W. Zinn, in *Phys. Rev. B*, **1989**, *39*, 4828.

[78] V. A. Dediu, L. E. Hueso, I. Bergenti, C. Taliani, *Nat. Mater.* **2009**, *8*, 707.

[79] V. Dediu, L. E. Hueso, I. Bergenti, A. Riminucci, F. Borgatti, P. Graziosi, C. Newby, F. Casoli, M. P. De Jong, C. Taliani, Y. Zhan, *Phys. Rev. B* **2008**, *78*, 115203.

[80] J. Ribas-Arino, T. Baruah, M. R. Pederson, *J. Chem. Phys.* **2005**, *123*, 044303.

[81] M. Mannini, F. Pineider, P. Sainctavit, C. Danieli, E. Otero, C. Sciancalepore, A. M. Talarico, M. A. Arrio, A. Cornia, D. Gatteschi, R. Sessoli, *Nat. Mater.* **2009**, *8*, 194.

[82] A. L. Barra, F. Bianchi, A. Caneschi, A. Cornia, D. Gatteschi, L. Gorini, L. Gregoli, M. Mafflni, F. Parenti, R. Sessoli, L. Sorace, A. M. Talarico, *Europ. J. Inorg. Chem.* **2007**, 4145.

[83] L. Margheriti, M. Mannini, L. Sorace, L. Gorini, D. Gatteschi, A. Caneschi, D. Chiappe, R. Moroni, F. Buatier de Mongeot, A. Comia, F. M. Piras, A. Magnani, R. Sessoli, *Small* **2009**, *5*, 1460.

[84] *Scanning Probe Microscopy and Spectroscopy* (Ed.: R. Wiesendanger), Cambridge University Press, Cambridge (UK), **1994**.

[85] R. Nakajima, J. Stohr, Y. U. Idzerda, *Phys. Rev. B* **1999**, *59*, 6421.

[86] C. T. Chen, Y. U. Idzerda, H. J. Lin, N. V. Smith, G. Meigs, E. Chaban, G. H. Ho, E. Pelegrin, F. Sette, *Phys. Rev. Lett.* **1995**, *75*, 152.

[87] G. Schutz, W. Wagner, W. Wilhelm, P. Kienle, R. Zeller, R. Frahm, G.Materlik, G. *Phys. Rev. Lett.* **1987**, *58*, 737.

[88] B. T. Thole, G. Vanderlaan, J. C. Fuggle, G. A. Sawatzky, R. C. Karnatak, J. M. Esteva, *Phys. Rev. B* **1985**, *32*, 5107.

[89] B. T. Thole, P. Carra, F. Sette, G. Vanderlaan, *Phys. Rev. Lett.* **1992**, *68*, 1943.

[90] R. Moroni, C. C. D. Moulin, G. Champion, M. A. Arrio, P. Sainctavit, M. Verdaguer, D. Gatteschi, *Phys. Rev. B* **2003**, *68*, 064407.

[91] N. Regnault, T. Jolicoeur, R. Sessoli, D. Gatteschi, M. Verdaguer, *Phys. Rev. B* **2002**, *66*, 54409.

[92] M. Mannini, P. Sainctavit, R. Sessoli, C. C. D. Moulin, F. Pineider, M. A. Arrio, A. Cornia, D. Gatteschi, *Chem. Eur. J.* **2008**, *14*, 7530.

[93] I. Letard, P. Sainctavit, C. Cartier Dit Moulin, J. P. Kappler, P. Ghigna, D. Gatteschi, B. Doddi, *J. Appl. Phys.* **2007**, *101*.

[94] J. Stohr, *J. Magn. Magn. Mater.* **1999**, *200*, 470.

[95] M. P. de Jong, I. Bergenti, V. A. Dediu, M. Fahlman, M. Marsi, C. Taliani, *Phys Rev. B* **2005**, *71*, 014434

[96] W. Wernsdorfer, N. Allaga-Alcalde, D. N. Hendrickson, G. Christou, *Nature* **2002**, *416*, 406.

[97] S. Stepanow, J. Honolka, P. Gambardella, L. Vitali, N. Abdurakhmanova, T. C. Tseng, S. Rauschenbach, S. L. Tait, V. Sessi, S. Klyatskaya, M. Ruben, K. Kern, *J. Am. Chem. Soc.* **2010**, *132*, 11900.

[98] D. J. Miller, L. Sun, M. J. Walzak, N. S. Mc Intyre, D. Chvedov, H. Rosenfeld, *Surf. Interf. Anal.* **2003**, *35*, 463.

[99] A. Licciardello, S. Pignataro, A. Lente, A. Benninghoven, *Surf. Interf. Anal.* **1993**, *20*, 549.

[100] J. B. Goedkoop, B. T. Thole, G. van der Laan, G. A. Sawatzky, F. M. F. de Groot, J. C. Fuggle, *Phys. Rev. B.* **1988**, *37*, 2086.

[101] J. P. Schillé , J.-P. Kappler , Ph. Sainctavit , Ch. Cartier dit Moulin , C. Brouder , G. Krill, *Phys. Rev. B* **1993**, *48* , 9491.

[102] H. Peisert, T. Schwieger, J. M. Auerhammer, M. Knupfer, M. S. Golden, J. Fink, P. R. Bressler, M. Mast, *J. Appl. Phys.* **2001**, *90*, 466.

[103] H. Peisert, I. Biswas, L. Zhang, M. Knupfer, M. Hanack, D. Dini, D. Batchelor, T. Chasse, *Surf. Science* **2006**, *600*, 4024.

[104] I. Biswas, H. Peisert, M. Nagel, M. B. Casu, S. Schuppler, P. Nagel, E. Pellegrin, T. Chasse, *J. Chem. Phys.* **2007**, *126*.

[105] I. Biswas, H. Peisert, M. B. Casu, B. E. Schuster, P. Nagel, M. Merzz, S. Schuppler, T. Chasse, *Phys. Status Solidi A-Applications and Materials Science* **2009**, *206*, 2524.

[106] F. Pobell Matter and methods at low temperatures; Springer, New York, 1996.

[107] E. Beaurepaire, H. Bulou, F. Scheurer, J.-P. kappler, in *Springer Proceedings in Physics, Vol. 133*, Berlin heidelberg, **2010**.

[108] A. De Cian, M. Moussavi, J. Fischer, R. Weiss, *Inorg. Chem.* **1985**, *24*, 3162.

Acknowledgement

Vorrei ringraziare innanzitutto chi ha contribuito alla mia crescita professionale ed alla mia formazione, ad iniziare dal Prof Andrea Caneschi che mi ha dato l'opportunità di iniziare questo percorso e la Prof.ssa Roberta Sessoli per avermi guidato con disponibilità e pazienza durante lo svolgimento di questo lavoro.

Ringrazio quindi coloro che hanno collaborato a questo lavoro di tesi: il Dott. Francesco Buatier de Mongeot per aver dato la possibilità di depositare su superficie i Magneti a Singlola Molecola, la Dott.ssa M. Federica Piras per l'acquisizione degli spettri ToF-SIMS, il Prof. Andrea Cornia per i preziosi consigli relativi alla sintesi dei composti, il Prof. V. Alek Dediu e la Dott.ssa Ilaria Bergenti per aver fornito i substrati delle manganiti e per il contribuito dato nell'interpretazione delle relative misure magnetiche.

Vorrei infine ringraziare tutti i compagni di viaggio che hanno reso piacevole la permanenza a Genova, Bologna, Modena, Grenoble, Villigen e sopratutto i compagni del LAMM con i quali ho condiviso questi anni.